Designed Amphiphilic Fullerene Morphologies with Optical and Electronic Control for Bottom up Functional Photovoltaics

Dissertation

zur Erlangung des akademischen Grades

doctor rerum naturalium (Dr. rer. nat.)

vorgelegt dem Rat der Chemisch-Geowissenschatlichen Fakultät der

Friedrich-Schiller-Universität Jena

Masters of Science (MSc Chemistry) Saunak Das

geboren am 10. März 1990 in Kalkutta, India

Gutachter:

1. ………………………………..

2. ………………………………..

(3. ………………………………..)

Tag der Verteidigung: ……………………….

Table of Contents

Included Publications

Major parts of this thesis have been *published, submitted* or *to-be-submitted (P1-P4)* in peer-reviewed journals. Some results have been presented as *conference contributions or research talks*. Few results were acquired during a *visiting research stay* as indicated.

Peer-reviewed Contributions

P1. **Das, S.**; Herrmann-Westendorf, F.; Schacher, F. H.; Taüscher, E.; Ritter, U.; Dietzek, B.; Presselt, M., Controlling Electronic Transitions in Fullerene van der Waals Aggregates via Supramolecular Assembly. *ACS applied materials & interfaces* **2016,** *8* (33), 21512-21521. *(IF-8.097)*

P2. **Das, S**.; Fiedler, J.; Buhmann, S. Y.; Walter, M.; Dietzek, B.; Presselt, M., Macroscopic Quantum Electrodynamic and (Time-Dependent) Density Functional Theory Approaches to Electronic Ground and Excited State Dispersion Interactions between Fullerenes. (*to be submitted)* **2019**.

P3. **Das, S**.; Preiß, J.; Plentz, J.; Brückner, U.; von der Lühe, M.; Eckardt, O.; Dathe, A.; Schacher, F. H.; Täuscher, E.; Ritter, U.; Csáki, A.; Andrä, G.; Dietzek, B.; Presselt, M., Controlling Intermolecular Interactions at Interfaces: Case of Supramolecular Tuning of Fullerene's Electronic Structure. *Advanced Energy Materials* **2018,** *0* (0), 1801737. (*IF-21.875)*

P4. **Das, S**.; Presselt, M., New horizons in supramolecular non-bonded fullerene aggregates with tunable optoelectronic properties. *(Submitted) Journal of Materials Chemistry A)* **2019**.

P5. **Das, S**.; Täuscher, E.; Biehl, P.; Ritter, U.; Schaefer, H. F.; Dietzek, B.; Presselt, M., Synthetic, Interfacial and Optoelectronic chemistry of PEG-functionalized Fullerenes. *(in preparation)* **2019**.

Conference and other contributions

1. *Poster:* **Das, S**.; Herrmann-Westendorf, F.; Dietzek, B.; Presselt Optical characterization of highly ordered donor-acceptorfilms made by Langmuir Blodgett technique, **2015** *DPG Spring Meeting, (Berlin, Germany)*

2. *Poster:* **Das, S**.; Herrmann-Westendorf, F.; Dietzek, B.; Presselt, M. Impact of Aggregation on Photonic Properties of Amphiphilic Fullerenes, **2015** *Bunsentagung, (Bochum, Germany)*

3. *Talk:* **Das, S**.; Dietzek, B.; Presselt, M. Morphological and Optical properties of Amphiphilic Fullerene Nanostructures, **2015** *European School on Molecular Nanoscience (ESMolNa), (Paris, France)*

4. *Poster:* **Das, S.** Herrmann-Westendorf, F.; Dietzek, B.; Presselt. M., Controlling Electronic Transitions in Fullerene Aggregates **2016** *MRS Fall Meeting Abstract (Pheonix, Arizona, USA).*

5. *Invited Talk:* **Das, S**.; Dietzek, B.; Presselt. M., Exploration of optoelectronic properties of fullerene nanostructures, **2017** *Department of Chemistry, University of Copenhagen, (Denmark)*

6. *Meeting Abstract:* **Das, S**.; Herrmann-Westendorf, F.; Hupfer, M.; Sivakov, V.; Dietzek, B.; Presselt, M. In Interface Doping in BHJ Solar Cells and Development of Well-Defined Model-Interfaces for Fundamental Studies and Understanding of Interface Processes and Involving Doping. **2017** *MRS Fall Meeting Abstract* (Boston, USA).

7. Presselt, M.; Herrmann-Westendorf, F.; Kaufmann, M.; **Das, S**.; Hupfer, M.; Dietzek, B. Colored soaps for photonics, **2017**; *American Chemical Society Meeting Abstracts*).

International Internship

Vice-Chancellor’s visiting research fellowship at Perovskite Lab, Soft Matter Physics Group of Adolphe Merkle Institute in University of Fribourg, Switzerland under the supervision of Dr. Michael Saliba *(March -June 2018).*

List of Abbreviations and Symbols

Chemical and Spectroscopy/Structure Terms

PEG	polyethylene glycol
AZO	aluminium zinc oxide
ACN	acetonitrile
$CHCl_3$	chloroform
OD	optical density
UV	ultraviolet
vis	visible
FMO	frontier molecular orbital
HOMO	highest occupied molecular orbital
MM	molecular mechanics
MO	molecular orbital
$MAPbI_3$	methyl ammonium lead iodide
TiO_2	titanium dioxide
TD-DFT	time-dependent density functional theory
LUMO	lowest occupied molecular orbital

Methods and Sample Names

AFM	atomic force microscopy
COSMO	COnductor-like Screening MOdel
CV	cyclic voltammetry
DLS	dynamic light scattering
LB	Langmuir Blodgett
LLIP	liquid liquid interfacial precipitation
SC	spin coating
DC	drop coating
IV	current voltage

PECVD	plasma enhanced chemical vapour deposition
PDS	photothermal deflection spectroscopy
TEM	transmission electron microscopy
TZV	triple zeta valence
SWV	square wave voltammetry
a-Si:H	amorphous silicon hydrogenated
HSC	hybrid solar cell
vdW	van der Waals
ETL	electron transport layer

Symbols

ϵ	molar absorption coefficient
λ	wavelength
$E_{1/2}$	half wave potential
Π	surface pressure
k_b	Boltzmann's constant
V_{OC}	open circuit voltage
FF	fill factor
J_{SC}	short circuit current
P.C.E.	power conversion efficiency
N_{nn}	number of nearest neighbours
N_{surf}	number of surface molecules
N_{bulk}	number of bulk molecules
ξ	N_{bulk}/N_{surf}
ψ	wave-function
E	energy

List of Figures

List of Tables

In all chaos there is a cosmos, in all disorder a secret order

-Carl Gustav Jung

1 Introduction

Parts of this chapter are taken from: **P4** – Progress and Development in Structural and Optoelectronic Tunability of Supramolecular Non-bonded Fullerene Assemblies Saunak Das, Benjamin Dietzek, Martin Presselt, *(submitted)* **2019**

1.1 Prelude

The ubiquity of fullerenes span from ''chaos to cosmos'', in the grand design of the universe and human's conscious reality! This remark might seem all too philosophical at a glance, but fullerene nanotubes are actually sought to store human consciousness artificially (vide Hameroff[1]) and they do inhabit interstellar space[2]. If Carl Jung is right (*cf.* quote above),[3] then these highly symmetrical (ordered) molecules must evolve into assemblies, relatively less ordered and vice-versa. Here philosophy unites with science, and this thesis aims to show that this very interplay of order/disorder in fullerene assembly can control properties to harvest energy in organic/carbon based electronics. But what makes fullerene based carbon electronics enticing in the first place?

The last two decades have witnessed dramatic progress in the field of carbon based electronics in the broad realms of semiconductor technology.[4] A constant demand for new materials with tunable physicochemical and optoelectronic properties to improve performance limits with progressive device miniaturization for eco-friendly disposable electronics have been launched. The pivotal focus is on carbon allotropes as they germinate from naturally occurring precursors and therefore, can be recycled for large-scale use.[4-6] Long ranged charge movement with negligible resistivity is their paramount property, rendering them ideal candidates in organic,[7] hybrid, perovskite solar cells,[8-9] field-effect transistors,[10] electroluminescent light emitters,[11] and photodetectors.[12] Among the different carbon allotropes, varying charge acceptance and subsequent migration properties occur depending on the nature of chemical bonding and molecular structure for *e.g.* bulk diamond cannot host mobile electrons, but graphene has exceptionally large electron mobility with reported values of 200,000 $cm^2\ V^{-1}\ s^{-1}$ from a single layer.[13-14] Interestingly, with the exception of graphite, all carbon allotropes used in electronics were directly/indirectly synthesized from fullerenes. For *e.g.*, carbon nanotubes are cylindrical fullerenes, and cutting nanotube laterally yields graphene sheets, which when stacked upside down produces graphite. The inception of fullerenes in 1985 by Kroto and co-workers,[15] bulk synthetic capabilities[16] and the recent discovery of finding stable fullerenes in the interstellar space,[2] have opened doors to a plethora of questions regarding their structure and properties. In this thesis, a broad scientific question pertaining to the usability of fullerene self-assemblies in optoelectronics is researched upon. In the following section, the scientific problem is described and subsequently tackled in the succeeding chapters.

1.2 Scientific Problem

Fullerenes, particularly C_{60} and C_{70} are ubiquitous electron acceptors in semiconductor technology.[17] Out of all known carbon allotropes only fullerene C_{60} can participate in isotropic electron transfer due to its unique icosahedral (I_h)-symmetry. Endowed with 12 alicyclic pentagonal rings and 20 hexagonal rings bearing conjugated delocalised π-bonds with sp^2-hybridization, fullerenes feature high electron mobility.[18] In addition, they reversibly accept up to six-electrons[19] making them supreme n-type organic semiconductors[20]. Fullerenes are often used in conjunction with a potential electron donor in binary mixed films (*e.g.* in bulk-heterojunction solar cells), where their shape allows fine phase separation. These three factors, namely, isotropic electron transfer, charge mobility and phase separation make them exceptional candidates in all branches of organic electronics *viz.* organic/hybrid/perovskite solar cells and organic field-effect transistors (oFETs).[20-25]

In spite of the aforementioned positive attributes, severe limitations restrict the practical usability of fullerene acceptors (FAs) in semiconductor industry. They are:

a) The first is its poor photon absorption in the vis-NIR region of the spectra. The same icosahedral shape which renders it beneficial for isotropic electron transfer, limits vis-absorption due to symmetry effect.[26-27]

b) Secondly, FAs comprise high electron affinities with limited energy level tunability, limiting their use with several potential electron donors.[28]

c) Lastly, synthesis of pure FA materials is a costly, time-consuming process limiting large scale industrial fabrication, *cf.* price of $PC_{61}BM$, a commonly used fullerene derivative is ~2 €/mg.[28]

Hence, an important scientific challenge is to find turnabouts to tackle the issues with FAs. To do so, a high level of control in optoelectronic properties is needed in FA structures; *i.e.* i) tunable vis-absorption, ii) tunable electron affinities in, iii) thin-films (usually <30 nm) to reduce the quantity of fullerene required for pocket-friendly functional photovoltaic devices. In this thesis, the above challenge is addressed by 'directed self-assembly' of a fullerene made amphiphilic, at different interfaces and on solid supports, characterizing their thin-film structure and finally, testing them in inorganic/organic hybrid photovoltaic devices. The next section strives to explain the legitimacy of "directed self-assembly" as the scientific approach to eradicate the above-mentioned limitations in the overall context of fullerene photovoltaics.

1.3 Scientific Approach and Methods

Molecular properties are primarily studied.in solutions,[29] to obtain an overview of the basic molecular properties (*e.g.* electron-donating/accepting efficacies, absorption coefficients, solvent dependencies or intra/intermolecular interactions). For single molecules of fullerenes dispersed in solution, obviously the limitation of poor vis-absorption and limited tunability of energy levels persist, producing ineffective devices as represented in Figure 1—1. However, it is well-known that optoelectronic properties may vary substantially, based on processing conditions of optoelectronic molecules for device applications.[30-33] This depends on structure-defining variables, namely, molecular orientation,[34] shape,[35] size,[36] packing[37] and order[38] of the supramolecular structures that constitutes the thin-films/devices. Literature reports suggest, that each of these parameters have substantial impact on optoelectronic properties, for *e.g.*: the ionization energy of pentacenes can be varied up to 550 meV when processed on Au(111) or SiO_x substrates based on their *orientation*, i.e. flat-lying or upstanding relative to the substrate.[39]

Thus, a reasonable approach to eradicate the drawbacks of fullerenes is to find ways to design supramolecular fullerene structures by self-assembly, which might lead to tailored optoelectronic properties, and can be successively programmed in photovoltaic devices. Therefore, understanding how fullerenes self-interact and respond to external processing methods shall enable production of structurally tuned supramolecular assemblies.[40] First, *self-assembly* is introduced and the role of *interfaces* for directed self-assembly is discussed in this work. Next, the steps followed to alleviate the drawbacks of fullerenes by achieving *optoelectronic control on surfaces and functional devices* is enunciated. Thus, the overall scientific framework can be summarized as '*fullerene self-assembly at interfaces and surfaces for optoelectronic control on substrates and in functional devices*'.

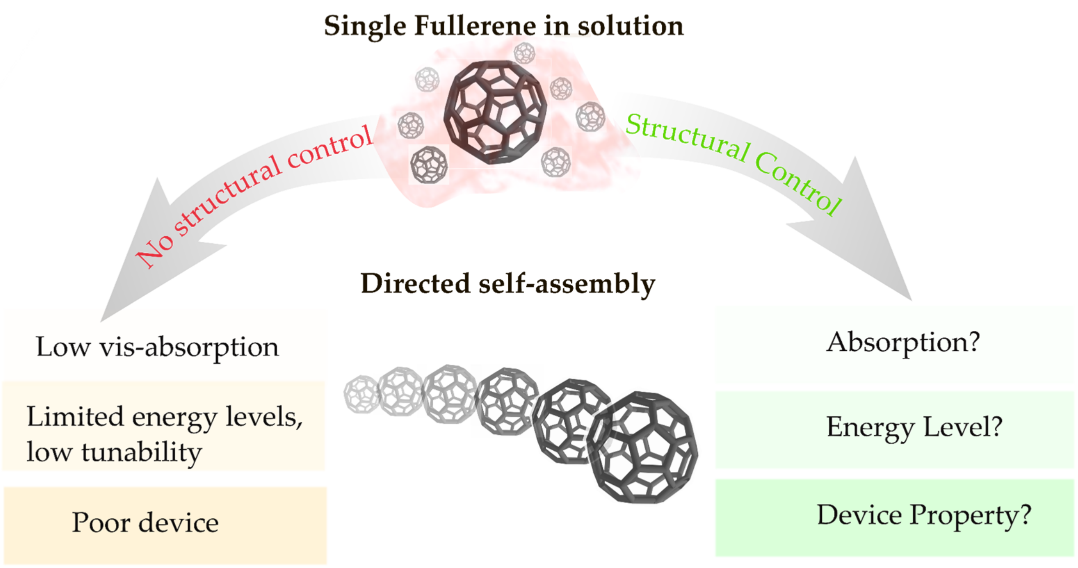

Figure 1—1: Scientific problem targeted and directed self-assembly approach adopted in this thesis to resolve drawbacks of fullerenes.

1.3.1 *Self-assembly at Interfaces and on Surfaces*

Self-assembly refers to the evolution of periodic arrangements of a molecule spanning from sub-nano, meso-, micro- to macro-scales into defined functional materials.[40] Depending on the nature and propensity of intermolecular interactions, shape, size, packing, geometry, mechanical/thermodynamic stability, the final functional response of the self-organized material is determined.[17] The major noncovalent forces which dictate self-assembly are π-π, van der Waals (vdW), hydrogen bonding, dipolar, electrostatic or hydrophobic(philic) interactions with differing degrees of stabilizing energies.[17] Utilizing these interactions, organic molecules can form zero-dimensional (nanoparticles),[41] one-dimensional (polymeric wires,[42] rod-coil molecules,[43] hair-pin,[44] nanowire, nanotube or filament like),[45] two-dimensional (liquid-liquid interfacial sheets,[46] Langmuir-Blodgett films[34]) and hierarchical three-dimensional structures (single crystal growth).[47]

For fullerenes, self-assembly is strongly controlled by molecular structure and preparation strategies.[48] Thanks to the pioneering works conducted by the research teams of Guldi,[20, 49-50] Nakamura,[51-52] Martin,[51-54] Nierengarten,[55-56] Wudl[56-57], Hirsch[58-59], Troshin[60-61], Bonifaci and Diederich[62], a large chemical bank of fullerene derivatives and supramolecular structures with outstanding physicochemical and electron-transport capabilities have been introduced with application in photovoltaics,[20] photocatalysis,[63] artificial photosynthesis[64] and sensors.[65] Diverse supramolecular architectures with truncated/controlled dimensionalities with non-covalent oligomeric-C_{60} can be formed using aggregation chemistry from the monomeric-fullerene units.[48, 66-70] To have a better control of these aggregate morphologies, suitable side-chain substituents are introduced that complement C_{60}-intermolecular interaction and introduce molecular order and stability.[71-72] Research at the few-molecule scale, particularly focused on the above-mentioned aggregate morphologies is necessary to bridge the gap between single molecule and optoelectronic device levels. However, only few reports describe the influence of size, crystal packing and intermolecular distances on optoelectronic properties of fullerene nanostructures.[73-75]

Thus, the purpose of using self-assembly in this thesis in context of fullerene electronics is manifold. a) Depending on the orientation, shape, size, packing and supramolecular order, absorption, charge transfer and subsequent transport efficacy of fullerenes can be controlled, and b) thermodynamic and mechanical stability of self-assemblies are higher than disordered/random aggregates which strongly control device flexibility and operation times.

It is chemically obvious, that in order to prepare structurally different assemblies *(point a)* from the same fullerene building block, different fabrication and synthesis protocols are necessary. Next, to address point b, specific fabrication protocols for producing fullerene structures with structural and spatial control on surfaces are crucial. This gives the perfect platform to produce fullerene structures at *interfaces*, where, tuning the area and nature of the interface can tune the spatial extent of the assembly, and can be successively deposited on surfaces.[1]

1.3.2 *Supramolecular & Optoelectronic Control on Substrates and Devices*

Controlling a typical physicochemical material property can be defined as, the ability to adjust that property by a desired quantity at will, through defined variation in experimental parameters. Albeit, achieving control in fullerenes which participate in random isotropic π-π and vdW interaction to inhibit structural control is not merely straight forward and requires a sequential suite of structure/property characterizations. The theorem in this regard is, that optoelectronic properties heavily depend on supramolecular structure of fullerene-assemblies. Thus, the interfacially synthesized

---

[1] A comprehensive description of these interfacial preparation methods can be found in Methods chapter

fullerene assemblies elucidated in the last section are characterized at varying assembly-scales, as follows:

a) ***Single and few molecular scales (<10nm)*****:** Tracking fullerene aggregates at single (fullerene diameter ~1 nm) and few molecular scales experimentally, is challenging. UV-vis studies on highly diluted thin-films (corresponding solution phase dynamic light scattering (DLS) data gives particle size <10 nm) may provide absorption signatures of monomers, dimers and smaller aggregates. At molecular scales, quantum chemical calculations enabled by density functional theory for determining energetically favourable geometries, binding energies and frontier orbital energies (FMOs) are suitable. Excited state calculations using time-dependent DFT or TD-DFT[76] are performed to complement experimental absorption data.

b) ***Few Molecule to thin-film morphology scales (10 nm- few µm):*** Fullerene morphologies produced by interfacial self-assembly are characterized in solution (dynamic-light scattering (DLS)) and on surfaces, namely, hydrophilic quartz (atomic force microscopy (AFM)) and on Cu-grids (transmission electron microscopy (TEM)). UV-vis spectroscopy on fullerene thin-films constituting interfacial assemblies provide spectroscopic fingerprints for detecting the effect of size, symmetry, packing and geometry. Electrochemical characterizations using cyclic and square-wave voltammetry on these structures immobilized on glassy carbon substrates enumerate redox properties and particularly LUMO-energies.

c) ***Device Scales (10-30 nm film with fullerene morphologies)*****:** After establishing a connection between supramolecular structure and optoelectronic properties, the same fullerene morphologies are tested as n-type layers in Si/fullerene hybrid solar cells.[24] The current-voltage characteristics of the device, is strongly dependent on fullerene's supramolecular structure.

1.4 Outline of this thesis

The earlier sections, laid forward the scientific problem, literature reports and discussed interfacial fullerene self-assembly. The open questions addressed in this regard, arose out of the above considerations and are listed as follows (see Figure 1—2):

a) How does self-assembly control optical and electronic properties?

b) How far can self-assembly scale spatially, if prepared from the same derivative?

c) How does optoelectronic properties change with b), *i.e.* at different size scales of the assembly, and with other structural parameters, like intermolecular distances and supramolecular order?

d) Can the morphology dependent optoelectronic properties be witnessed in a pure self-assembly based solar cell, in the form of certain photovoltaic parameter variation?

Finally, how far addressing the above questions (a-d), can alleviate the drawbacks of FAs as outlined in section 1.2, is examined. The outlines of this work are schematically depicted in Figure 1—2, distributed into three chapters (3, 4 and 5) as follows:

Chapter 3 focusses on controlling the optical properties of fullerenes in solution and thin-films with quantum chemical calculations. It stresses on a typical fullerene made amphiphilic by polar –PEG tail substitution, compare its LB (ordered) and SC (random) thin-film structures, and elucidates the role of supramolecular structure (random/ordered) on optical absorption features. Particularly, supramolecular size is varied by embedding MPEGC_{60} in stearic acid matrices by means of a dilution series, from large supramolecular clusters down to monomers and dimers. Furthermore, theoretical modelling by extensive TD-DFT calculations on different structures and geometries, explore optical features of fullerene non-covalent assemblies. Finally, spectroscopic fingerprints of non-covalent dimers are derived and optical features are controlled based on preparation methods.

Chapter 4 is focused on bottom-up synthesis of a wide range of fullerene morphologies *via* self-assembly. Here, interfacial assembly and film deposition methods, LB and LLIP are used to fabricate finger-print like packed assemblies, spatially ordered 2D nanosheets or folded sheets, *i.e.* nanowires, and exfoliated flakes. These unique interfacial assemblies are compared with DC vesicular and SC ellipsoidal structures which grow into crystalline grains and subsequently aggregate into spheroids upon annealing. UV-vis studies of these above-synthesized structures is presented, to correlate morphology with optical properties. The paramount outcome of this chapter is presentation of a length scale of self-assembly of the above synthesized fullerene morphologies, extending from a few nanometers up to μm sized nanosheets. Finally, these structures endowed with supramolecular shape, size, packing and order and optical properties, enables a morphological control on fullerene supramolecular assemblies.

Chapter 5 investigates the electrochemical properties of the fullerene assemblies as established in Chapter 4, to unravel their LUMO energies. In order to understand the influence of morphology on LUMO and binding energies, quantum chemical calculations are performed to corroborate experimental data. Next, a correlation function between LUMO-energy and morphology was derived leading to a novel equation, enabling control on fullerene's electronic property

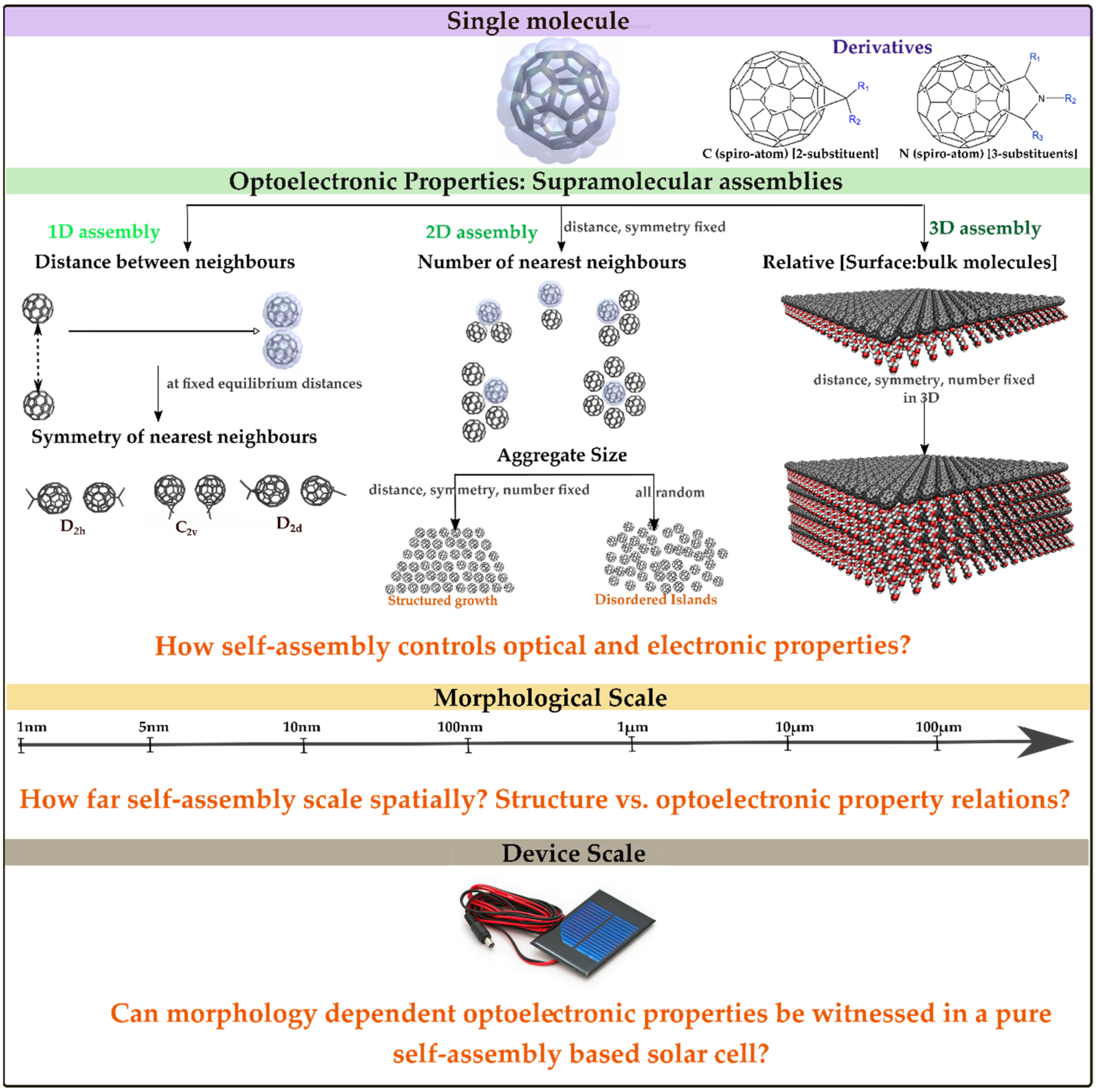

Figure 1—2: Scientific questions addressed in this thesis: For a single fullerene molecule which can be either derivatized by using a C-bridge for two substituents or a N-bridge for three- how fullerene structure changes in an assembly taking into account intermolecular distances, symmetry, order and height at each dimension, with corresponding changes in optoelectronic properties at different self-assembly scales, and solar cells made by incorporating these morphologies.

Finally, these established fullerene assemblies are transferred to p-i-n Si/fullerene hybrid-solar cells. Amorphous-Si as p^+-absorber with amphiphilic fullerene assemblies serving as n^+-doped acceptor, and pure p-i-n a-Si reference solar cells are fabricated and characterized. The LUMO energy variation in $MPEGC_{60}$ morphologies, is shown to linearly vary the open-circuit voltage of the hybrid solar cells, and shown to yield record performances.

In Summary *(**Chapter 6**)*, the essential results from Chapter 3, 4 and 5 are summarized to demonstrate how far the pertinent drawbacks of fullerene in electronics (Figure 1—1), could be alleviated.

Thus, in a nutshell the following chapters strives to provide a holistic exploration by - "*designed amphiphilic fullerene morphologies with optical and electronic control for bottom up photovoltaics*", manifesting the title of this thesis.

2 Methods- Theory and Experiment

This chapter is divided broadly into theoretical and experimental methods used in this thesis. The theoretical methods comprise of quantum chemical modelling using Density and (Time-Dependent) Density Functional Theory. The experimental part is classified into Preparation methods (interfacial self-assembly and standard thin-film techniques), Characterization Methods (Optical (Absorption Spectroscopy), Morphological (Microscopy) and Electronic (Electrochemistry)) and finally, Applications (Theory and Characterization of solar cells).

2.1 Theoretical Methods

Quantum chemistry is indispensable to study physical properties of matter in subatomic to molecular scales.[77] At such length scales, quantization of energy, momentum etc., wave-particle duality, and limited deterministic probability of conjugate variables (energy/time or position/momentum) are witnessed. These phenomena, which are largely deviant from the macroscopic view of nature emerge from quantum mechanical considerations and form the basis of electronic structure theory. In this theory, the behaviour of electrons in the electrostatic field created by stationary nuclei is considered.[78] This forms the basis of Born-Oppenheimer's approximation stating that the nuclear and electronic motion can be separated.[79] In the Schrödinger treatment of quantum physics the property of an isolated system is considered to be best described by wave-function ψ which is an eigen function of space and time.[80] This fundamental function forms the basis of Schrödinger equation, $\hat{H}\psi = E\psi$. This, mathematically is an eigen equation which states that the Hamiltonian operator $\hat{H}$ (given by summation of kinetic and potential energy operators), when operated on ψ, will give the eigen value or total energy E corresponding to that system. Solving this equation through computational modelling have made the evaluation of energetically favourable molecular structure determination, their ground and excited state properties, potential energy surfaces, dynamics, reactivity, and dissociation pathway analysis possible.[81]

Exact solution of Schrödinger equation can be obtained for one electronic system only (*e.g.* homonuclear dihydrogen cation H_2^+), that too, for the time-independent part and considering Born-Oppenheimer's approximation. Thus, different theories like valence bond theory,[82] Hartree-Fock (HF),[83] Multi-Configuration Self Consistent Field (MCSCF),[84] Multi-Reference Configuration Interaction (MRCI),[85] Many Body Perturbation Theory (MBPT)[86] including Coupled cluster methods,[87] Dynamical Mean field theory,[88] Quantum Monte Carlo (MC) methods,[89] and Density Functional Theory (DFT)[90] have been developed to solve the Schrödinger equation through some approximations. Each of these methods operate at different computational expense and have different degrees of accuracy to convincingly describe the electronic structure. In this thesis, DFT and it's time-dependent analogue (TD-DFT) has been used to describe ground or excited states, and electronic structure of fullerenes and their aggregates.

2.1.1 Density and Time-Dependent Density Functional Theory ((TD)-DFT)

In DFT, electron densities of molecules composed of many electrons (non-interacting fermions) are considered.[90] This helps in conceiving the idea of an effective internal potential v_{eff}, which experience an external field v_{ext} given by the chemical composition of the molecule. This is elementary in understanding the two Hohenberg-Kohn (H-K) theorems, fundamental to DFT.[91] The first theorem states that v_{ext} and hence the total energy is an unique functional[2] of electron density $\rho(\mathrm{r})$. Mathematically, this leads to $E_{g.s.} = f(\rho(\mathrm{r}))$. The second H-K theorem states that a functional minimises the total energy or v_{ext} to ground state energy only when the input electron density $\rho(\mathrm{r})$ is true. These considerations became instrumental in the development of Kohn-Sham (KS) equations.[92] Using these Schrödinger-like eigen equations a simplified picture of DFT[93] can be conceived:

$$\left(\hat{H} = -\frac{\hbar^2}{2m}\nabla^2 + v_{eff}(r)\right)\varphi_n(r_n) = \varepsilon_n\varphi_n(r_n)$$

In the above equation, ε_n or the eigen value represents the individual orbital φ energies and the total electron density, $\rho(\mathrm{r}) = \sum_n^N |\varphi_n(r)|^2$. Subtracting exchange correlation (electronic interaction energy, E_{xc}), Coulomb energies ($E_H\rho(\mathrm{r})$ and exchange correlation over total electron density from total orbital energies ($\int f^{'}(E_{xc})\rho(\mathrm{r})$), the total ground state energy ($E_{g.s.}$) of the molecule can be obtained:

$$E_{g.s.} = \sum_n \varepsilon_n - (E_H\rho(\mathrm{r}) + E_{xc}\rho(\mathrm{r})) - \int f^{'}(E_{xc})\rho(\mathrm{r})$$

These mathematical treatments in DFT is helpful to develop a convincing picture of energetically favourable structures (optimized geometries), total energies, and spatial distribution of electrons (orbital diagrams) which collectively describes the ground state of the system.

---

[2] A functional simply means the function of a function.

The time-dependent analogue of DFT (TD-DFT) is used to describe dynamic properties of the many electron system.[94] Thus, the external potential v_{ext} act upon a many-body system with time-dependent wave-function ψ(t) or ϱ(t). In contrast to ground state (DFT), such a case is rather complicated because the effective potential changes with time, which necessitates information of many-body electron densities from initial times. Thus, the time-dependent Schrödinger equation needs to be solved and a simplified picture can be formed from the celebrated Runge-Gross (R-G) theorem.[95] In the R-G framework, for a given initial ψ, it can be shown that the potential can be mapped in a one-to-one relationship with ϱ(r,t).

Using the DFT approach ground state properties and by the TD-DFT approach, the absorption spectra of fullerene derivatives and their aggregates are evaluated and discussed in the thesis (Chapter 3 onwards). Computational modelling are usually performed using quantum chemistry program packages like Turbomole,[96] GAMESS,[97] Gaussian[98] etc. where the theoretical frameworks (*e.g.* DFT or TD-DFT) are pre-loaded. Most calculations are performed on a starting geometry of the to-be-studied molecular structure, described by a 3D *xyz* matrix where each atom takes a point in space.

In this thesis, Turbomole was used and generalized gradient approximation (GGA) and BP86 exchange-correlation functional were used. Optimizations was carried out using splitvalence polarization (SVP) and triple-zeta valence (TZV) basis sets with gradually increasing convergence criteria. Furthermore, MARI-J approximation with D3 dispersion interaction correction was used as detailed.[99-100] Solvent interactions in mediums having different dielectric constants were treating through COnductor-like Screening Model (COSMO)[101] (for vacuum and infinite permittivity medium).

Excited state responses were typically obtained by Turbomole's singlet excitation module for escf. For these TD-DFT calculations, 300 electronic dipole transitions were calculated per irreducible representation, to cover the entire spectral window from near IR to UV. The obtained line spectrum was broadened by Gaussian broadening. Lastly, the obtained theoretical absorption spectra was hypsochromically shifted by 0.35 eV and matched with experimental absorption spectra recorded either using UV-vis spectroscopy in transmission mode or Photothermal Deflection Spectroscopy. The following section is dedicated to several characterization techniques, first starting with these above-mentioned optical characterization methods.

2.2 Experimental Methods

2.2.1 *Sample Preparation*

Seven different MPEGC$_{60}$ films are mediated on solid supports by Drop Coating (DC), Spin Coating (SC) with/without annealing, Langmuir-Blodgett (LB) and Liquid/Liquid Interfacial Precipitation (LLIP) methods. The supports include quartz (for AFM and UV/vis characterizations), Cu-grid (for TEM studies), Glassy Carbon Electrodes (for electrochemical measurements). Finally, these are processed on amorphous Silicon surfaces for hybrid solar cells. This section will outline the basics of these interfacial self-assembly techniques used. Figure 2—1 provides a pictorial summary of these sample preparation methods.

2.2.1.1 Interfacial deposition

An interface between two phases can be defined as the two-dimensional boundary surface sandwiched between them. Generally, assembly of molecules at interfaces (liquid/gas or liquid/liquid), is a result of reduction of surface tension, upon addition of a molecule, usually an *amphiphile*, typically consisting of polar and non-polar parts.

At an interface, there exists an imbalance of intermolecular forces which is responsible for the initial (i) surface tension ɣ, or $ɣ^{i}$ under static conditions. When a sufficiently diluted amphiphile is introduced at the interface, the surface tension of liquid phase reduces, evident by increased surface pressure (Π) because of re-distribution of intermolecular forces.

$$\Pi = ɣ^{i} - ɣ$$

The polar-part of the amphiphile orients itself towards the polar liquid phase, due to favourable van der Waals (vdW) forces, dipolar interaction and H-bonding in certain cases.[102] In contrast, the non-polar part tends to face the gaseous/non-polar liquid halves of the interface. Contextually, the liquid/liquid interface provides a second stabilizing vdW force to orient the non-polar moiety of the amphiphile. For liquid/gas interfacial assembly, the polar part is stabilized by the polar solvent phase, while the non-polar part of the amphiphile self-assembles because of intermolecular interactions, as the carrier solvent evaporates.[103] In this work, liquid/gas interfacial deposition employing the air/water interface is enabled by Langmuir Blodgett (LB) technique. Additionally, liquid/liquid interfacial precipitation method (LLIP) is used for inducing fullerene assembly (see Figure 2—1).

- *Langmuir Blodgett (LB) Technique*

LB technique developed by Irving Langmuir and Katharine Blodgett is a simple yet sophisticated nanostructured assembly and deposition tool usually operating at the air water interface.[102] The assembled one-molecule thick film (monolayer), or Langmuir film can be deposited on a chosen substrate moving either horizontally (Langmuir-Schaefer), or vertically (Langmuir Blodgett) relative to the interface. Repeating this process multiple times at defined barrier positions produce multi-layered functional films with defined thickness, for targeted applications.[104]

A typical LB setup comprises of a water filled bath at known temperatures bath kept horizontally on a flat surface (panel A, Figure 2—1). The molecule to be assembled is finely dissolved in an evasive carrier solvent (usually Chloroform) and is dispersed at the air-water interface. After allowing a waiting time for complete carrier solvent evaporation, the interfacial area is reduced (compressed) using two automated mobile barriers. At different barrier positions, the molecule transit between different intermolecular orientations, giving its corresponding gas/liquid/solid and transition phases. This is turn gives the characteristic mean molecular area (A), and thus, a qualitative hint about molecular orientation. Thereby, surface pressure Π (representing the degree of intermolecular interaction) is gradually increased and corresponding Π-A isotherms are detected *via* Wilhelmy plate method (Figure 2—1).[105] The shape and nature of these isotherms is given by concentration dependent phase change.[103]

At sufficient dilution (gas phase with amphiphile concentration << CMC) there is no self-interaction between the dispersed molecules and the reduction of surface tension *vs.* concentration is linear. If the interface is linearly compressed at constant temperatures, the amphiphile starts to self-interact. Based on this principle and Gibbs equation for interfacial thermodynamics, one observes a function for gaseous phase relating Π and A. This is given by $\Pi A = k_B T$, where A is the mean molecular area of the amphiphile, k_B is the Boltzmann's constant and T absolute temperatures.[3] From this equation surface pressure Π is found to rise hyperbolically, in the gas phase regime[106] (see G-part of the isotherm in panel A, Figure 2—1).[107]

---

[3] Alternatively, this equation can be understood by conventional kinetic theory of gases. The average translational kinetic energy for each degree of freedom, is $k_B T/2$. For an ideal 2D gaseous interface, the total kinetic energy is therefore, $k_B T$. Thus, $\Pi A = k_B T$.

Compressing the gaseous interface further leads to thermodynamic phase transitions (usually first order) and formation of liquid and solid states[103] with chemically distinct phases. Generally, these can be broadly classified into *liquid-expanded* (LE), *liquid-condensed* (LC) and solid phases.[103]

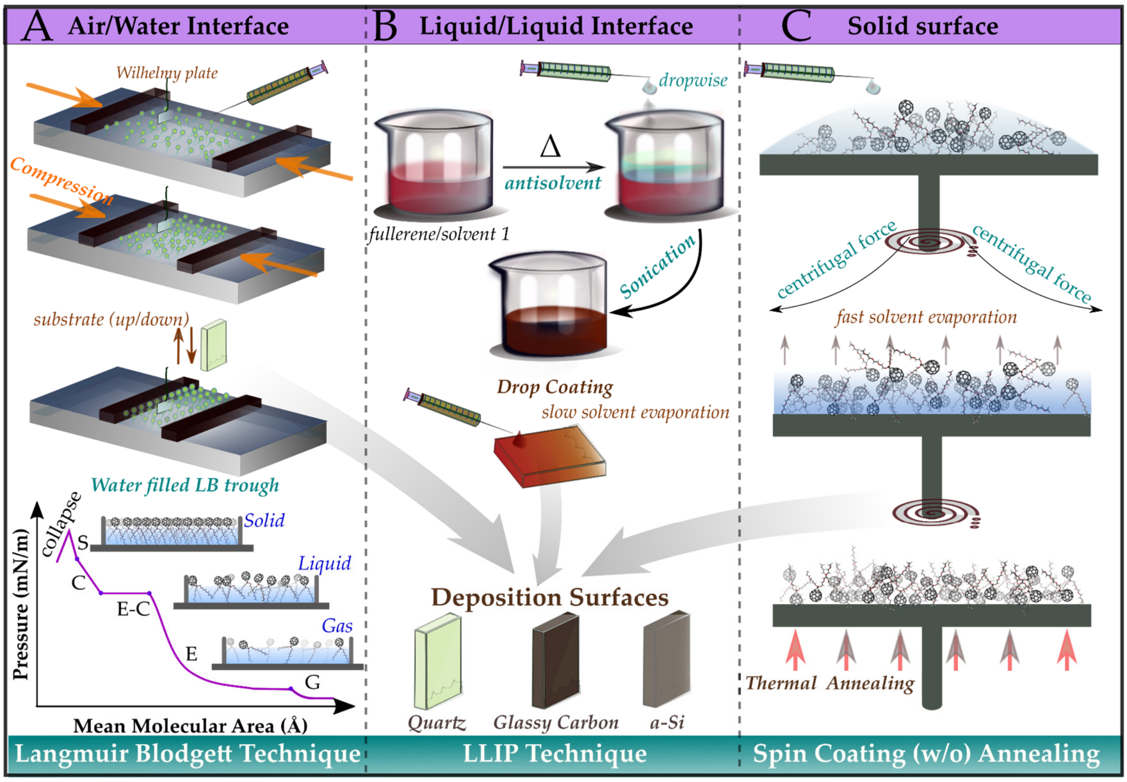

Figure 2—1: Preparation methods used in this thesis: (A) In LB technique, amphiphilic molecules are dispersed at the air-water interface and compressed *(orange arrows)* by two mechanical barriers. With compression Π-A isotherms are recorded *(purple graph, below)* via Wilhelmy plate method. (B) LLIP method where the antisolvent is added at elevated temperatures to a homogenous solution forming an interface, which is then disturbed by sonication. (C) Sequential events of self-assembly during spin coating, and thermal annealing. All assemblies are transferred to three surfaces (panel B), each intended for targeted characterization.

For expanded phases, there is no definite relationship between mean molecular areas and surface pressure. The Π-A isotherms are often characterized by rapidly changing mean molecular areas at virtually constant surface pressures, because the molecule is subjected to tremendous intermolecular forces phase as it undergoes first order thermodynamic transition. As the molecular chain length is increased or bath temperature is decreased these expanded phases disappear and a liquid-crystal like monolayer is achieved. On further compression, ideally, a close packed solid phase is witnessed.[108]

For condensed and solid phases, mean molecular areas can be derived by extrapolating the linear part of the isotherm to zero pressures. This gives rich information about the molecular crystal structure and their orientation at the interface.[103]

- *Liquid/liquid Interfacial Precipitation (LLIP)*

Liquid/liquid interfacial precipitation (LLIP) of an amphiphile is usually carried out at the interface of two liquids constituting two solvents of contrasting polarities, for *e.g.* methanol/chloroform or toluene/isopropanol (see Figure 2—1).[109] An amphiphile can orient itself between two liquids, into its thermodynamically favourable self-assembled structure, in absence of an external force. The size of the obtained supramolecular structures scales with the extended area of the interface, *i.e.* relative miscibility. In cases where the solvents are completely immiscible (*e.g.* hexane and methanol), there is one extended 2-D interface where self-assembly occurs, given by the cross-section of the reaction chamber. The resulting self-assembled structures are thus several micrometres long. In contrast, nm-scale self-assemblies are obtained upon tuning interfacial area by using: a) sparingly miscible solvent pairs b) changing proportions of the chosen solvent pair,[48] and, c) vigorous sonication for extended time for dynamic self-assembly.[110]

To complement and compare with the above described interfacial synthesis methods, standard fast and slow -solvent evaporation techniques, namely Spin- and Drop coating (SC and DC) respectively, with post-processing annealing, are treated in this work (Figure 2—1). In SC a solution containing the molecule of interest is spun on a substrate at chosen angular speed for a certain time. The centrifugal force acting outwards, helps in spreading the solution and form a flat film by fast solvent evaporation. In comparison to the 2D interfacial methods detailed earlier SC produces thin-films with lesser nanoscale morphology control. In contrast, DC method refers to drop-by-drop deposition of a solution on substrates, and subsequent formation of thin-film by natural evaporation. DC produces more amorphous films with lesser supramolecular control in comparison SC. Annealing, *i.e.* heating the formed films at chosen temperatures induce crystallinity and renders them suitable for applications.

2.2.2 *Optical Characterization*

In this thesis, optical characterization of the prepared samples was performed using Photothermal Deflection spectroscopy (PDS) and absorption spectroscopy in transmission mode (UV-vis). In this following section fundamentals of PDS is discussed and compared with UV-vis spectroscopy in transmission mode.

2.2.2.1 Photothermal Deflection Spectroscopy (PDS)

PDS technique is a highly sensitive spectroscopic technique for measuring absorption of thin solid films.[111-113][4] PDS operates through '*mirage cantilever effect*', and the measured absorption signals are due to three sequential events: a) *Photo*- the sample and its surroundings (usually a transparent solvent of high temperature dependency) is heated up by a monochromatic light-source; b) *thermal*- a thermal lens, *i.e.* a liquid dome consisting of a gradient of refractive indexes is generated around the focus point, and c) *Deflection*- the deflection of a laser beam grazing across the thermal lens is determined using a position detector. Within these sequential steps, the light absorbed by the thin-film sample resulting in the thermal lensing is a measure of the deflected recorded by a position detector (see Figure 2—2).[114]

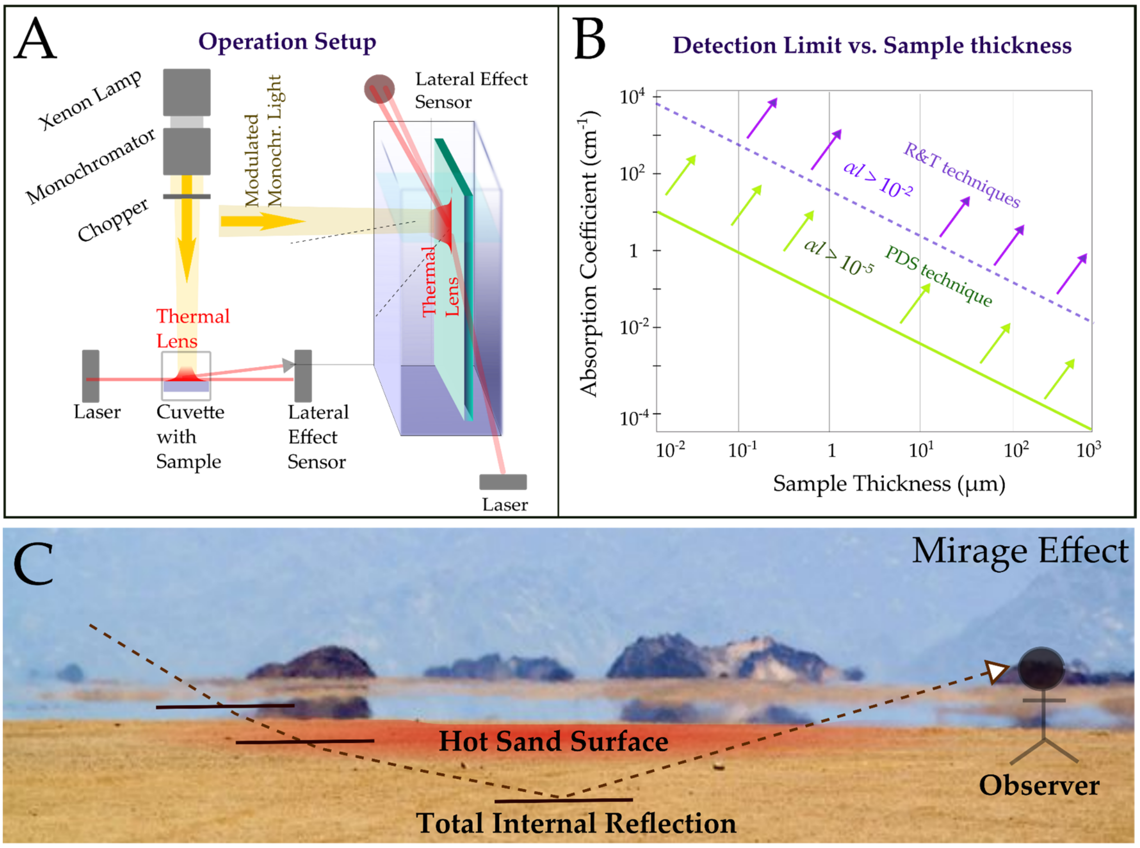

Figure 2—2: (A) Operation Setup of PDS; (B) Comparison of the detection limit of PDS *vs.* R&T absorption spectroscopy. (C) Portrayal of Mirage Effect on which PDS is based. Background image is by loskutnikov posted in Shutterstock.

---

[4] The section is influenced by a tutorial talk of Dr. Henner Kampwerth about PDS at the University of New South Wales (UNSW, Sydney) on 13/12/2017.

Due to modulated heating, the sample and surrounding liquid produces a gradient of varying temperature gradient and hence varying optical reflectivity. This thermal lensing effect cause the grazing laser beam to deflect, whereby, the detected deflection of the laser beam must be proportional to the rise in temperature. This temperature increment due to optical absorption and thermalization is actually well described by the heat equation. The deflection distance (S) is proportional to the solvent's temperature dependency, given by $\left\{\left(\frac{1}{n_0}\right)\left(\frac{dn}{dT}\right)\right\}$, heat gradient ($\nabla T$), interaction distance (L), and the modulation speed (e^{iwt}), *i.e.*

$$S \propto \left(\frac{1}{n_0}\right)\left(\frac{dn}{dT}\right) L \nabla T e^{iwt}$$

This equation is simplified by considering a low diameter of the probe beam and a substrate with a lower absorption coefficient than that of the thin-film. If the film is supposed to have small temperature gradient upon heating, then the equation can be further simplified, yielding the simplified PDS equation of absorption, giving a measure of the absorbance (A):

$$S/_{S_{ref}} = 1 - e^{\alpha l} = A$$

Here, S_{ref} denotes the reference laser deflection for a film with 100% absorption, α determines the absorption coefficient and l determines the thickness of the thin-film.

PDS is particularly necessary to bypass the drawbacks associated with standard R&T based absorption spectroscopy, namely:

i) At longer wavelengths specifically in the IR regime, photodetector noise heavily influences UV-vis signals measured in reflectance/transmission (R&T) mode.

ii) These measured absorption signals are directly dependent on the optical detector's wavelength of operation. All photodetectors show good sensitivity within a specified wavelength range, given by the bandgap of the photodetector. Usually the photodetector changes while moving from visible to IR. This is why, usually unavoidable noise crops in when moving from detector to detector due to their relative differences in sensitivity.

iii) Lastly, it is difficult to measure: a) *scattering samples* (*e.g.* colloidal dispersion immobilized films which are optically opaque), and b) *few-atom thick samples* (monolayer of quantum dots film) with R&T spectrophotometers. They are poorly sensitive and it is often difficult to separate sample-signal from scattering

PDS is an excellent technique to bypass the above issues. The minimum absorption which can be recorded by PDS is 10^{-2} which is 1000x higher than that of R&T spectrophotometers, making it ultrasensitive to optically thin samples. Secondly, the PDS can be performed on opaque or rough substrates unlike R&T. Thirdly, PDS can measure scattering samples. Lastly, PDS data is not limited by detector variation because in contrast to reflectance/transmission absorption spectroscopy, the thin-film itself act as the detector in PDS. A schematic figure describes the working principle of PDS.

The home-built PDS setup consists of the parts sketched in Figure 2—2. The light source component is a 1000 W Xe-high pressure lamp from LOT-QD and a 260 mm monochromator is used to deliver maximum light intensity from 200 nm up to 2500 nm.

a) A chopper (Thorlabs) modulates this incoming light which then focused on the thin-film sample immersed in a perfluorohexane solvent filled cuvette.

b) The intensity of the incident light is monitored using a quartz glass plate functioning as the beam splitter, placed between focusing lens (f=75 mm) and the sample, and a UV-optimized trans-impedance amplified silicon detector obtained from Thorlabs.

c) The deflection of a 0.5 mW HeNe-laser is measured using a lateral effect sensor PDA90 from Thorlabs.

d) The whole system is controlled using a Labview program, collecting all the data and corrects the PDS signal in accordance to the incident intensity.

2.2.3 *Morphological Characterization*

The morphology of produced supramolecular fullerene assemblies are characterized in solution and films. Three characterization techniques were used, namely: a) Dynamic light scattering (DLS) for solutions b) Atomic force microscopy (AFM) on films and c) Transmission electron microscopy (TEM) on air-dried fullerene films on Cu-grids.[5] Of this the principles of DLS and TEM are discussed briefly and AFM is discussed with more details, in the upcoming section.

---

[5] Dynamic light scattering, and Transmission electron microscopy experiments were performed by JENANO- Professor Dr. Felix H. Schacher group in FSU Jena. Specifically, Oliver Eckardt, Dr. Felix Schacher measured light scattering samples and Dr. Moritz von der Lühe measured transmission electron microscopy samples.

In DLS, Rayleigh scattering of molecular aggregates in solutions is measured by recording a typical speckle pattern.[115] This pattern is produced when a polarized monochromatic laser passes through a scattering sample, *i.e.* fullerene assemblies in solution. The intensity of the measured signals changes dynamically (particle's Brownian motion) and an autocorrelation function is used to estimate the size of the mobile aggregates. In this thesis CONTIN analysis was performed to estimate the hydrodynamic diameters of very dilute (<100 μM) solutions and LLIP fullerene solutions. The detection limit is usually >2 nm. The setup comprises of an ALV Laser CGS3 Goniometer with ALV Avalanche correlator and a He–Ne laser (λ = 633 nm).

TEM was used to measure supramolecular size and packing of 2D fullerene assemblies (LB and LLIP) at the single molecule level. In contrast to the laser source in DLS, TEM uses an electron source beam which is shone on air-dried films on Cu-grids[116]. The resulting scattered light contains specific information about molecular arrangements. The typical resolution of TEM is around 0.2 nm. For TEM measurements from air-water interface, hydrophilic Cu-grids were prepared by Ar plasma cleaning (~30 s) (Diener Electronics). A typical TE-microscope (Zeiss-CEM 902A, Oberkochen, Germany) having a 1k TVIPS FastScan CCD camera was used for measurement.

2.2.3.1 Atomic Force Microscopy

AFM is a high resolution scanning probe microscopic technique for morphological measurements of samples with lateral dimensions >30 nm and vertical dimension >0.1 nm.[117-118] The general advantage of AFM over TEM is that the former provides height information of the surface. However, the lateral resolution of TEM is in the atomic scale, which is superior to that in AFM. In AFM, the interaction between a probe (a sharp tip <10 nm supported on a flexible cantilever) and a sample in solid/liquid environment is measured. The probe is usually made of Si, SiN or polymers depending on the mode of AFM operation. The tip is usually made conical in shape and has an apex diameter of 4-5 μm. The cantilever, usually up to 200 μm in length keeps oscillating obeying the Hooke's law (Force = -Spring Constant x distance), with a spring constant between (0.5-50 N/m). The probe is connected to a piezoelectric scanner and is moved laterally (X, Y) and in Z directions across the sample surfaces. Using a raster scanning method, detailed information about the 3D surface structure is obtained.

Several forces of interactions (vdW, dipole-dipole and electrostatic) operate between the sample surface atoms and the tip, essentially determined by their chemical properties. The force between the surface atoms and probe is essentially described by a Lennard-

Jones potential like curve governed by their separation distance Δz (see panel B, Figure 2—3). Generally, AFM operates in three modes of operation given by the separation distance Δz (Figure 2—3). At distances far from the sample surface the nature of interaction is purely attractive and this is utilized for measurements in the *non-contact* mode. As the tip approaches equilibrium distances, the mode of operation is called *tapping* mode. At even shorter distances, only repulsive interaction occur as the tip makes real contact with the surface and is utilized for *contact mode* AFM.

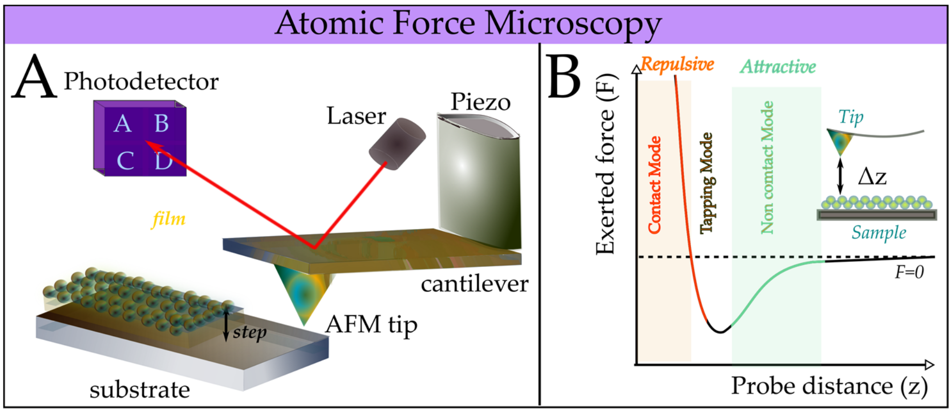

Figure 2—3: (A) Setup and (B) Operation principle of AFM.

In this thesis, AFM (Veeco Digital Instruments Dimension 3100 AFM) in: a) tapping mode where the probe consisted of a silicon tip (radius: 8 nm) at 300 kHz (Budget Sensors Tap 300-G) and, b) contact mode ("ContE-G" with Cr/Pt-casting) were utilized. Tapping method was used for the analysis of grains with lateral dimensions spanning from ~30 nm to ~0.6 µm and heights <100 nm. Contact mode method was utilized to estimate film thickness was determined by square scratching method. In this method the tip in contact is first moved with a high velocity across smaller areas (3 µm × 3 µm) of the film surface effectively scratching large parts of the sample. This created a step height (see panel A, Figure 2—3) which was subsequently scanned at larger areas (10 µm × 10 µm) and measured by line profiles to determine film thickness.

2.2.4 *Electronic Characterization*

Electronic characterization in context of this thesis refers to evaluation of the frontier-orbital energies and binding energy profiles of the molecule of interest in solutions and thin-films. Conventionally electrochemical techniques (cyclic voltammetry,[19, 119-120] square-wave,[121] or Osteryoung square-wave voltammetry), gas-phase low temperature photoelectron spectroscopy,[122] scanning tunnelling spectroscopy,[123] ultraviolet (HOMO) and solid state inverse photoelectron[124] or laser two-photon photoemission spectroscopy

(LUMO)[125] are used for electronic characterizations. The obtained results using these above-mentioned methods are then usually compared/validated with additional DFT-based simulation.[126]

2.2.4.1 Cyclic and Square Wave Voltammetry (CV and SWV)

In this thesis, electrochemical sweep techniques are utilized, namely cyclic and square voltammetry (CV and SWV) to evaluate FMO energies of fullerenes and is compared with that obtained *via* DFT-modelling.[127] The fundamentals of these electrochemical methods rely on the classical Nernst equation for redox-couples in solution phase, originally derived from the second law of thermodynamics.[128] Based on the solvent environment an electrochemical double layer is formed at the vicinity of the electrode. In presence of a supporting electrolyte usually at high concentrations, forward and backward potential scans are applied to a working electrode. If a redox process can be activated in the molecule where the reduced/oxidized species is stabilized within the potential sweep time-scale, cathodic and anodic current/voltage peaks are witnessed. The Nernst equation for such a process is given by:

$$E_{pc/pa} = E_o - \frac{RT}{nF} \ln \frac{[Red]}{[Ox]} \quad \text{or,}$$

$$\frac{RT}{nF} \ln \frac{[Red]}{[Ox]} = (E_o - E_{pc/pa})$$

The shape of the voltammogram is largely determined by two factors: a) increased currents as $E_{pc/pa}$ becomes too large or too small facilitating thermodynamically favourable Nernstian behaviour up to the redox maxima, and b) tailing down of the voltammogram due to transport limited current which can be understood from Fick's law (see panel B, Figure 2—4). Fick's law indicates that the diffusion rate of a species depends on the concentration gradient, *i.e.* $J = D\frac{\Delta C}{\Delta X}$. Here J is the Fickian diffusion rate, D the diffusion coefficient, ΔC and ΔX represents change in concentration and distance from electrode surface respectively, while their division represent the concentration gradient. At the electrode surface all the analyte species can be assumed to be reduced or oxidized at the peak potentials. Moving further away from the electrode surface, the concentration difference ΔC (between electrode surface and bulk solution) remains fixed, but the distance ΔX keeps growing which effectively slows down J with time. Thus the voltammogram tails off generating lesser current at potentials away from peak potentials. Thus this unique shape characteristic of CV is both Nernstian and Fickian, solely controlled by the scanning potential.

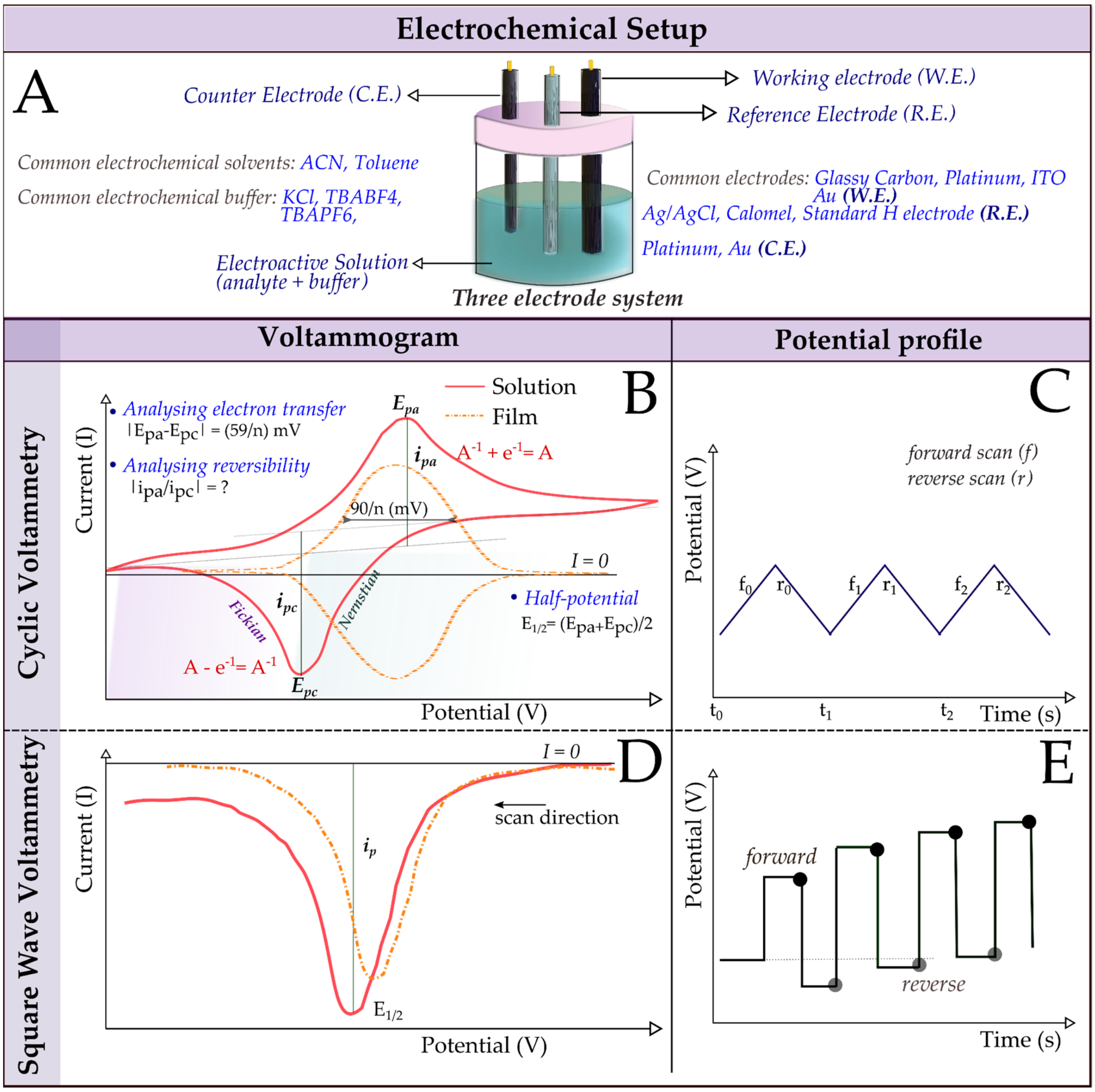

Figure 2—4: Description of electrochemical methods: (A) Commonly used three electrode electrochemical setup with chemicals and components; (B) and (D) Features of a typical CV and SWV (reduction) performed in solution or on chemically modified W.E. The CV peak-shift of 59/n mV for a redox process with n transferred electrons does not occur for thin-film voltammograms; (C) and (E) demonstrates potential *vs.* time profiles of the corresponding methods.

In CV, half wave potential ($E_{1/2}$) is measured which is given by the numerical average of the cathodic and anodic peak potentials, E_{pc} and E_{pa} respectively (see panel B, Figure 2—4). For reversible/quasi-reversible redox reaction, difference between the anodic/cathodic peak potentials is given by $\frac{59}{n}$ mV where n designates the number of electrons transferred in the redox process.[127] It is important to recognize that these individual processes, *i.e.* potentials and currents from cathodic/anodic waves, and the peak potential difference to identify number of transferred electrons are pertinent to redox processes in solution. In contrast, for a redox-active molecule immobilized on working electrode, the potential difference between the anodic/cathodic waves is zero. Electrochemistry on thin-films (<100 nm) require higher sensitivity and elimination of non-Faradaic currents, which is done by SWV. In SWV, the reduction/oxidation $E_{1/2}$ potential is directly obtained from single redox peaks.

From the cathodic (reduction) and anodic (oxidation) peaks of CV (in solution) and SWV (thin-films), the HOMO/LUMO energies are determined. This requires evaluation of an onset potential (E_{onset}), which can be defined as the electrochemical potential for reducing/oxidizing just the FMOs.[129] In principle, HOMO/LUMO is only relevant for molecules in vacuum, but is approximated by ionization energy/electron affinities, which is primarily defined for single electron ejection or injection to atoms in gas phase. Furthermore, electrochemistry is performed in solution phase with several thermodynamic processes surrounding the solvent shell. This makes HOMO/LUMO estimation from electrochemical data challenging but specific standards are utilized to legitimately correlate the measured electrochemical data to vacuum scales (correlation offset between 4.8 to 5.3 eV has been reported). The huge variation of the reported LUMO-energies for the popular PCBM molecule, spanning over ~250 meV,[122] justifies that correct correlation scales and reference electrode standard are needed for absolute determination of FMO energies. *vs.* vacuum The HOMO/LUMO is finally computed from the onset potential and correcting for the ferrocene half-potential and the vacuum scale correction as[129].

$$E_{HOMO/LUMO} = -(E_{onset,ox/red} - E_{1/2}^{Fc/Fc^{+}}) + 5.1\ \mathrm{eV}$$

2.3 Application: Theory and Characterization of Solar Cells

Photovoltaic cells, convert light energy (solar photons) into electrical energy *i.e.* usable work, and is one of the current solution to meet global energy crisis. Silicon solar cells have been in the forefront of photovoltaic technology because of their high efficiencies, low-environmental toxicity and offering variety of structures for targeted demands. Though most solar panels are based on crystalline-Si, low temperature fabrication (<250 °C), possibility of different substrates and low cost make amorphous-Si (a-Si) a prospective energy harnessing material.[24] In Chapter 5 of this thesis, hybrid (organic/inorganic) solar cells were fabricated. In the amorphous hydrogenated Silicon (a-Si:H), acting as the p-type and the fullerene as the n-type semiconductor.[130] In the following section, a short theoretical treatment is provided to understand the basics of inorganic, organic or hybrid solar cells and subsequently the fabrication method of the device adopted in this thesis is described.

In practice solar cells can be based on a single *pin*-junction or on multiple junctions, usually called tandem cells. The intrinsic or pure semiconductor material (i-layer) primarily absorbs solar photons and gets photoexcited. The p^+- and n^+-doped semiconductors act as the hole and electron majority carrier layers respectively. The device can either take a sandwich architecture or can the p^+-doped and n^+-doped materials can be intermixed, adopting a bulk-heterojunction structure as in solution processed organic photovoltaic cells (see panel B, Figure 2—5).[131]

The vacuum levels at infinite distances for two semiconductor materials far from one another is considered to be the same, and is equal to the potential energy of an isolated electron at rest in vacuum. The potential wells within these materials can be imagined to be merged at the interface which falls off at larger distances.[132] Their individual fermi energies (E_F) merges in contact and individual surface dipoles of the materials get aligned.[133] If one of this material is p-type and the other n-type, then electrons tend to migrate from the n-type rich semiconductor surface to p-type, and the holes from the p-rich surface to the n-type (see panel A, Figure 2—5. These charges instantaneously balance out by recombination with the majority carriers on the opposite sides resulting in a *depletion zone* or *space-charge region*, which stays in dynamic equilibrium.[134] This continuous diffusion of majority carriers creates an electric field which becomes particularly strong as the space-charge region attains dynamic equilibrium *i.e.* the majority carriers can no longer diffuse across the depletion zone. Under such conditions electricity is produced as the residual holes in the p-type and electrons and n-type flows through an external circuit upon photo-activation.[135]

In organic photovoltaics the events associated with current generation in the active layer is closely related to the above situation. Usually, a solution processed blend of electron donor and acceptor molecules (active layer), similar to intrinsic or i-layer in *pin*-configuration is sandwiched between two electrodes having suitable work functions. The substrate (usually quartz glass) and electrode (transparent conducting oxides) in the direction of incoming photons are made transparent for maximum absorption. Organic materials are primarily intrinsic semiconductors, where charge generation is preceded by formation of a bound electron/hole (e^-/h^+) pair called an exciton.[136-138] This occurs when incoming photons absorbed by the active layer excites an electron from the HOMO of the electron donor to its LUMO. This e^-/h^+ pair is bound together by Columbic forces with total binding energies smaller than that of unbound charges The acceptor can get photoexcited too, but the due to a larger absorption coefficient excitons are primarily generated in the donor phase.[139-140]

Exciton binding energies depend on the material's dielectric constant, but are typically larger than thermal energy at room temperature (25 meV). Thus, they tend to recombine until and unless, the charge separated state reaches energetically stable state through charge delocalization in the e^- and h^+ orbital wavefunctions. Thus, after these excitons diffuse randomly within the photoexcited active layer, either recombination occurs or they dissociate at the donor:acceptor interface. The acceptor LUMO being typically lower than the donor LUMO, provides the necessary driving force in dissociating the exciton. Thereby, the acceptor gets reduced while the donor is oxidised. These separated charges move freely under the influence of an external electric field generating photocurrent.

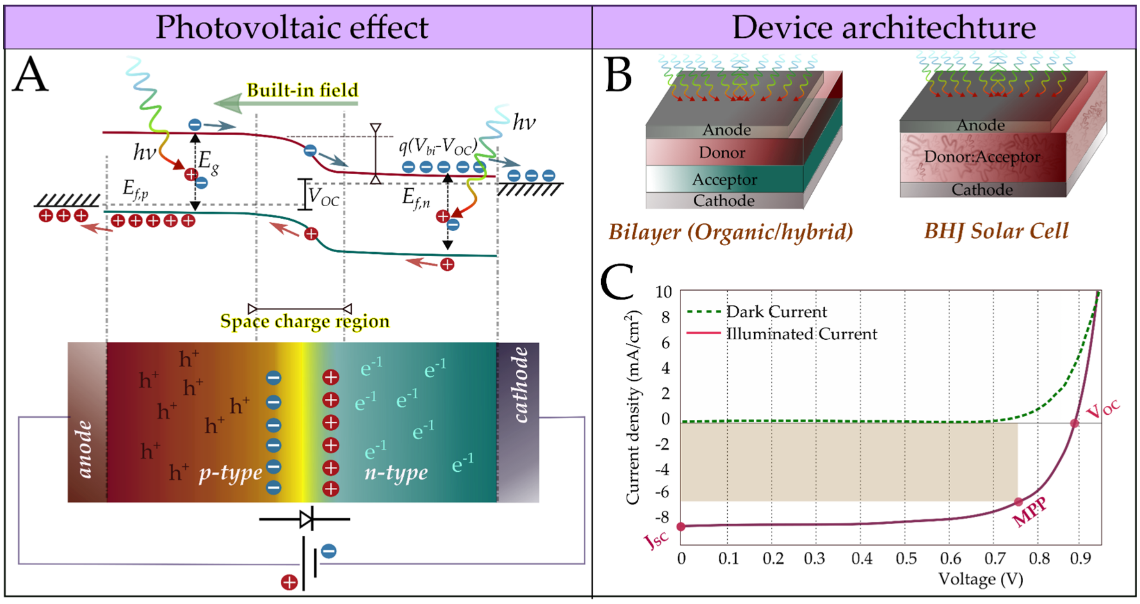

Figure 2—5: (A) A typical p-n junction type solar cell and events of charge carrier generation upon illumination. The Fermi energies (E_f) of the p- and n-type components merges in contact near the space charge region. The corresponding majority carrier migrate to the electrodes. (B) Typical architecture of bilayer or BHJ solar cells, and (C) Typical IV profile of a functional solar cell. The biscuit brown rectangle gives the total obtained power (P_{max}) at maximum power point (MPP), whereas the ideal power is given by the product (V_{OC} × J_{SC}). Their ratio determines the fill factor of the solar cell.

In this thesis (Chapter 5) hydrogenated amorphous Si (a-Si:H)/fullerene hybrid solar cells were constructed.[24] These were fabricated at low temperatures using plasma enhanced chemical vapor deposition (PECVD).[141] Amorphous Si offers flatter surface than crystalline-Si (c-Si) *cf.* surface roughness of a-Si:H is <1 nm,[142] almost 5 times less than c-Si. The deposition of the fullerene layer necessitated interruption of HSC-fabrication in vacuum after the intrinsic a-Si:H layer deposition leading to the spontaneous formation of a thin oxide layer on the a-Si:H surface.[143] This lead to the formation of virtually hydrophilic surfaces, chemical similar to quartz. Thus the conventional a-Si:H p+-i-n+-doped stack model was used with highly p-doped a-Si:H (10 nm), intrinsic a-Si:H (300 nm), fullerenes as the n-type layer. Being an indirect semiconductor the Si-layer thickness is large by a factor of 20-30, *w.r.t.* fullerenes. Therefore, photon absorption primarily occurs in the Si-layer. All layers apart from interfacially deposited fullerenes were deposited using PECVD upon 200 nm Al-doped ZnO (AZO) serving as the transparent front contact. The reflective back contact was a 300 nm silver deposited and designed by a shadow mask producing 16 solar cells per batch.[6]

2.3.1 *Active layer morphology and device parameters*

The active layer morphology plays pivotal role in controlling the overall performance of the photovoltaic cell. A measure for solar cell performance is given by its external quantum efficiency (EQE) which is a measure of the fraction of photons which gets converted into charges. This in turn depends on the material's extinction coefficient and the device's internal quantum efficiency (IQE). IQE simply is a measure of the fraction of absorbed photons which leads to collectable charges. Clearly, this depends on a number of factors: a) exciton dissociation and recombination, b) free charge migration, c) charge collection at the electrodes. Of these, a) and b) are strongly dependent on the morphology of the active layer, *i.e.* the supramolecular structure of pure donor or acceptor phase, nature of the interface, and the structure of their co-assemblies. Point c) is mainly defined by the external electric field which is controlled by the work functions of the respective cathode and anode materials.[131]

The overall efficiency of a solar cell is governed by several factors, but the heart of the problem lies in the molecular structure of the photoactive components which control their optical excitations and electronic energy levels. The difference in fermi energies of the 'n' and 'p' components of the p-n junction solar device, gives a hint of the maximum cell voltage. Therefore, $eV_{OC} = \varepsilon_F(n) - \varepsilon_F(p)$.[131, 135] For organic semiconductors, usually this

---

[6] Further details about device architecture, band diagrams and characterization are in Chapter 5.

is given by the difference in donor HOMO and acceptor LUMO energies, which is the energy needed to separate electron/holes. The fabricated cell is usually characterized by measuring Current (I)-Voltage (V) curves using illumination produced by a solar stimulator. A typical I-V curve is presented in panel C of Figure 2—5.

A number of characteristics, namely open circuit voltage (V_{OC}), short circuit current (J_{SC}), fill-factor (*FF*) and power conversion efficiency (*P.C.E.*) gives an estimate of the quality of the solar cell. Upon forward biasing, two types of currents flows through the external circuit: a) illuminated current, and b) dark current. The illuminated current is the usual photocurrent generated upon illumination and dark current is produced due to leakage of carriers across the space-charge region in the dark. The voltage, at which the dark and illuminated currents balance out, zero photocurrent produced in the circuit and is defined as V_{OC} (see panel C, Figure 2—5). At zero voltage. The current density measured at zero voltage is called short-circuit current which is actually a measure of the light-generated carriers in the circuit. The maximum cell power (maximum power point) is the area of the biggest rectangle inscribed within the I-V profile. For a good solar cell the product of J_{SC} and V_{OC} (ideal solar power) must very close to the maximum power point (P_{max}). The ratio between the *MPP* and ideal power versus is indicative of the quality of the solar cell and is defined as fill factor (*FF*).[131]

$$FF = \frac{P_{mpp}}{P_{ideal}} = \frac{J_{mpp} \times V_{mpp}}{J_{SC} \times V_{OC}}$$

For all practical purposes the stability of the solar cell is estimated by measuring the cell efficiency at the maximum power point. Lastly, the P.C.E. of the solar cell is the most commonly used parameter which is indicative of the incident spectral power which the device can convert photocurrent. Thus, it is given by:

$$PCE = \frac{J_{SC} \times V_{OC} \times FF}{P_0}$$

The electronic and optical properties of materials used in the photovoltaic device play important role in controlling these solar cell parameter, and is detailed in Chapter 5 of this thesis.

3 Fullerenes–Optically Controlled Supramolecular Assemblies

Parts of this chapter follows from these articles: **P1** – Saunak Das, Felix Herrmann-Westendorf, Felix H. Schacher, Eric Täuscher, Uwe Ritter, Benjamin Dietzek, and Martin Presselt *ACS Applied Materials & Interfaces* 2016, *8, 33, 21512-21521*. **P2** – Saunak Das, Johannes Fiedler, Oliver Staufert, Michael Walter, StefanYoshi Buhmann, and Martin Presselt *Physical Chemistry Chemical Physics* 2019, *(to be submitted)*

Like most fullerene derivatives spanning from the smallest C_{20} to the mega-fullerene (C_{3996}),[144-145,20] pristine C_{60} features strong UV-absorption (λ_{max} = 256 nm) with an absorption coefficient similar to that of amorphous Si (~10^4-10^5 cm^{-1}), but *centrosymmetry* limits it's vis-absorption significantly.[27] Additionally, fine-tuning of fullerene's band structure to promote efficient charge-injection into its vacant electronic states is essential for their application in functional devices.[146] Furthermore, the assembly of pristine fullerenes into functional and ordered monolayer(s) requires them to be soluble in a wide-range of solvents, minimal to no self-aggregated clusters and high structural stability of fullerene thin-films. Thus, for most practical applications, C_{60} is substituted with suitable side-groups (see Figure 3—1) in order to: (i) enhance its vis-absorption coefficient and tailor optical transitions, (ii) fine-tune its Frontier Molecular Orbital (FMO) energies, and (iii) improve directed self-assembly into stable, ordered monolayers.

Before we delve into points (ii) and (iii) which are discussed in the next chapters, this chapter entails a conceptual overlook about fullerene's molecular structure and optical properties.

3.1 Structural Considerations

The van der Waals (vdW)-diameter of a single C_{60}-molecule is nearly 1.1 nm, whereas the furthest atomic nuclei distance is 0.7 nm (see Figure 3—1).[147] Due to a curved molecular surface the constituent σ and π-bonds cannot be fully decoupled and individual bond-lengths deviate from standard linear C=C length (1.33 Å) to fit into the perfectly spherical architecture of the buckyballs. In effect, the double bonds between adjacent [6,6] hexagonal rings (both, π-systems) are shorter than the ones between [5, 6] penta- and hexagonal (one σ- one π-system). Out of the sixty molecular orbitals (m.o.), typically, the frontier orbitals participate in charge transfer processes and are studied with special focus.[147]

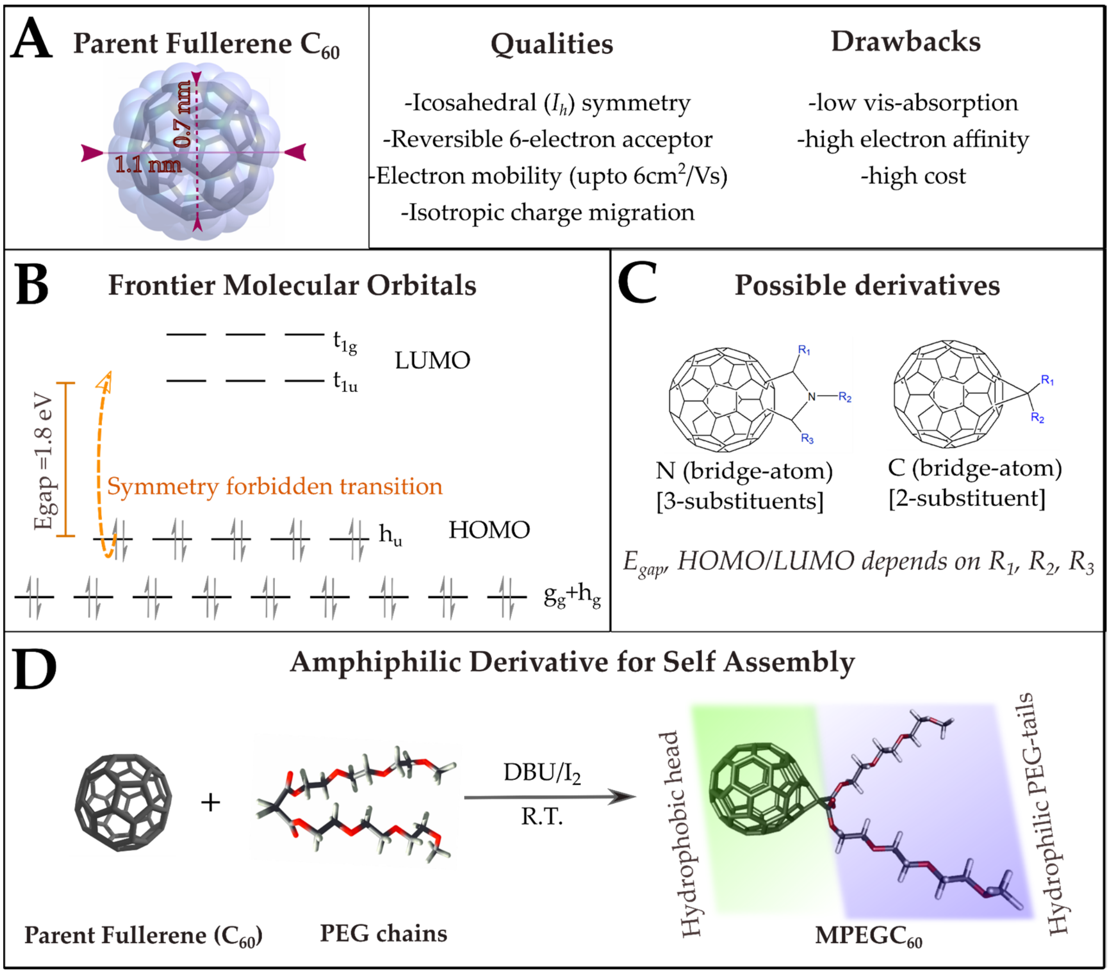

Figure 3—1: (A) Parent C_{60} structure, its qualities and drawbacks; (B) FMO orbitals of C_{60} and their symmetries with tunable energies usually done by derivatization as shown in C; (D) Synthesis route for MPEGC_{60} employed in this work.[7]

Typical substitution occurs at the [6,6]-position through a single C-atom bridge position, allowing maximum two ligands, or through a –C-N-C– moiety (with N-bridge), facilitating three substituents.[7] Electron-donating or accepting ligands withdraw or push electron density into the buckyballs altering molecular orbital energies and optical properties (see Figure 3—1). The polarity of the solvents in which the fullerene derivative solubilizes is strongly dependent on the polarity of these ligands. Pure C_{60} is virtually immiscible in most organic polar solvents (water, methanol, isopropanol *etc.*) but demonstrate excellent solubility in highly non-polar solvents, *e.g.* toluene/hexane. The most widely used Phenyl-C_{61}-butyric acid methyl ester (PCBM), for *e.g.* have similar solvent affinities like C_{60}, because both substituents are sufficiently hydrophobic. Forced dissolution (sonication, heat, extended mixing) of these hydrophobic fullerenes in polar

---

[7] MPEGC_{60} was synthesized by Dr. Eric Täuscher, Prof. Uwe Ritter and team from TU Ilmenau.

solvents yields several micrometres long disordered aggregate structures, with uncontrolled optoelectronic properties, due to random fullerene-fullerene noncovalent interactions.[48]

Aggregation effects in solution cause changes in the absorption spectra,[148] which correlate to particle size, but these aggregates: (i) disintegrate rapidly upon thin-film formation and (ii) trap charges if a systematic and hierarchical control of the supramolecular order is not established.[149] Therefore, for fullerene thin-film electronics, morphological control of the fullerene assembly[48] is preferable to provide well-defined interfaces, charge percolation pathways and thermodynamic stability. Thus the major target for functional fullerene films is to attain a targeted design for hierarchical morphology control and simultaneously expand the limits of light absorption.

In contrast to pure fullerene aggregates, substituting parent C_{60} by hydrophilic pendant side groups yield derivatives with diverse solubility, *i.e.* in both polar and non-polar solvents.[150] These amphiphilic fullerenes self-interact and form distinct superstructures at defined concentrations. Due to contrasting polarities, the hydrophilic side chains act as shield in limiting random fullerene-fullerene interactions. Furthermore, depending on the side group, mechanical and thermodynamic stability of a fabricated fullerene thin-film can be improved. Here, two short bis-polyethylene glycol malonate chains are substituted to parent C_{60} yielding MPEGC_{60} (see Figure 3—1).

The amphiphilicity of MPEGC_{60} facilitates directed self-assembly with the aid of programmable interfacial film fabrication, here the Langmuir-Blodgett (LB) technique.[151-153]. When MPEGC_{60} in $CHCl_3$ solvent (MPEGC_{60}/ $CHCl_3$) is dispersed onto water, the hydrophilic MPEG-tails selectively penetrates the water, while the hydrophobic C_{60}-moeities keep floating on the water surface. Upon evaporation of the carrier solvent $CHCl_3$, the air/water interface is linearly compressed, yielding a flat monolayer commensurate with a prototype tetragonal/hexagonal packing arrangement.[8] In contrast to LB-technique a faster solvent evaporation method of producing relatively amorphous thin-films with rather lesser supramolecular control, is the commonly used Spin Coating (SC) technique[9].[154] It will be shown in this chapter that the optical properties of fullerene thin-films heavily depends on the actual supramolecular structure, packing and aggregate symmetry, mediated by the above LB and SC-methods of film production.

---

[8] Morphology and structure of these L and LB type films are discussed in Chapter 4.

[9] Fundamental details about these sample preparation techniques are included in Chapter 2.

3.2 Optical Properties

3.2.1 *Solutions*

A comparison of the absorption spectra of $MPEGC_{60}$ with the commonly used PCBM sheds light on important optical states within characteristic electronic transitions (see Figure 3—2). Spectral features of PCBM and $MPEGC_{60}/CHCl_3$ are compared to quantum chemically (TD-DFT) derived absorption spectra. Within the experimentally accessible spectral window in $CHCl_3$ ($\lambda > 240$ nm), the $MPEGC_{60}$ spectrum is similar but slightly hypsochromically shifted if compared to the spectrum of PCBM[155] and features two prominent peaks at 256 and 326 nm.

According to TD-DFT calculations, the $MPEGC_{60}$ peak at 256 nm is constituted by two pronounced electronic transitions, similar to the two prominent transitions to nT_{1u}-excited states (n = 6, 7) in I_h-symmetric C_{60}.[72, 156] The peak at 326 nm is a superposition of several medium-intensity and weak transitions which might be compared to the transition to the $3T_{1u}$ state in I_h-C_{60} (335 nm). Additionally, an extremely sharp Soret-like peak appears at 425 nm, which is typical for fullerene derivatives with [6,6]-bridged carbons.[157] Absorption at longer wavelengths than 400 nm is very weak.[158] However, the weak vis-absorption originates from several transitions that are symmetry-forbidden in I_h-C_{60} but gain intensity because of Herzberg–Teller intensity borrowing.[159-160] Furthermore, combination bands contribute to these transitions.[161] These combination bands comprise Jahn–Teller active modes, which partially favours these otherwise forbidden transitions.[27]

The spectral difference between $MPEGC_{60}$ and PCBM arises because: (i) PCBM comprises of an electron withdrawing aryl group (-C_6H_5), which withdraws electron density *via* the C-bridge atom. In contrast, $MPEGC_{60}$ is functionalized with two weakly electron withdrawing –MPEG chains. These substituents with differences in electron pulling strength (inductive effects) influence the C_{60}'s electronic structure differently, modulating the optical transitions. (ii) Due to the presence of two identical side chains, $MPEGC_{60}$ is arguably more symmetric (belongs to C_{2v} point group) than PCBM causing differences in optical transitions.

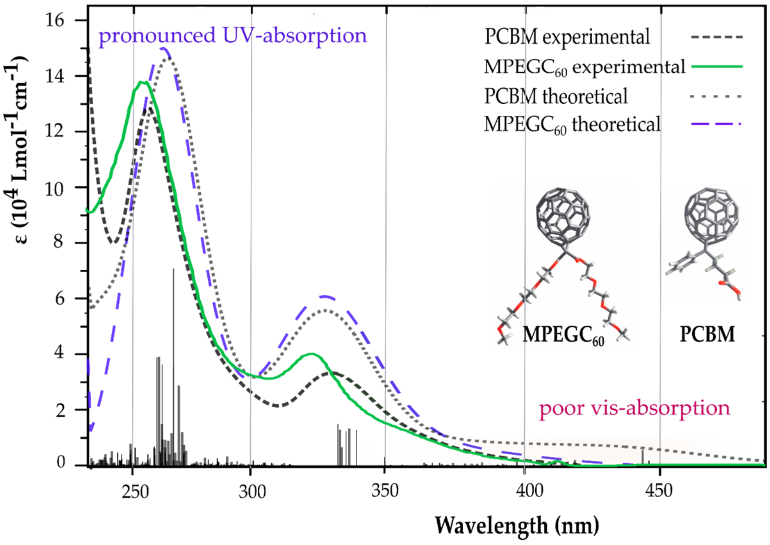

Figure 3—2: Experimental and TDDFT-derived absorption spectra of MPEGC$_{60}$ and PCBM. TDDFT results are shown as stick spectra as well as dashed line spectra obtained by Gaussian broadening. The region below 240 nm is not discussed because of strong CHCl$_3$ absorption in this spectral range.

3.2.2 *Thin-films*

Having characterized the absorption features of dissolved MPEGC$_{60}$ in solution described in the preceding section, spectroscopic properties of aggregates in thin solid films are presented below. The focus will be on spectral changes due to formation of aggregates observed in SC and LB films and then on analysis of model aggregates using TD-DFT calculations. The supramolecular structure of these SC, LB thin-films was altered by systematic fullerene loading in a stearic acid matrix. This molar blending ratio is varied from pristine MPEGC$_{60}$ (100%) to high dilutions of 0.9%. Due to higher sensitivity than conventional absorption methods, photothermal deflection spectroscopy (PDS)[10] is employed for spectral characterizations of these highly diluted thin-films.[111, 113]

At first, possible aggregates at low concentrations (0.9% and 1.3%) are tracked, to deduce reasons of thin-film spectral variation. At a low concentration of 0.9% (equals 36 μM), the SC films are largely dominated by monomers. At 1.3%, dimers and smaller clusters start dominating the fabricated films. This was confirmed by dynamic light scattering (DLS) experiments. The particle size distributions shown in Figure 3—3 is governed by scattering effects from both solvation shells and the core C$_{60}$-fullerenes with entangled

---

[10] Fundamental details on PDS is provided in Chapter 2.

MPEG chains. The mean particle distribution at the lowest concentration (0.9% $MPEGC_{60}$) is centred around 3.1 nm which slightly shifts to lower radii of around 2 nm upon increasing the concentration to 1.3%. The solvation shell of $MPEGC_{60}$ in $CHCl_3$ at such low concentration varies with the orientation of the flexible MPEG chains enveloping the C_{60} core. This variation in solvent shells can explain the difference between the mean radii of the two differently concentrated $MPEGC_{60}$-solutions. Both radii approximately fit to the length to a single $MPEGC_{60}$ molecule (~2.5 nm) associated with a solvation shell. Therefore, both solutions are presumably dominated by $MPEGC_{60}$ monomers. In addition, at 1.3% we the appearance of the first onset of aggregation was observed which was absent at 36 μM concentration. The radial size distribution of these aggregates ranges from 4 nm over to 9 nm and is expected to be a signature from small vdW dimers (~5 nm) or trimers (~7.5 nm) enveloped by the solvent shell.

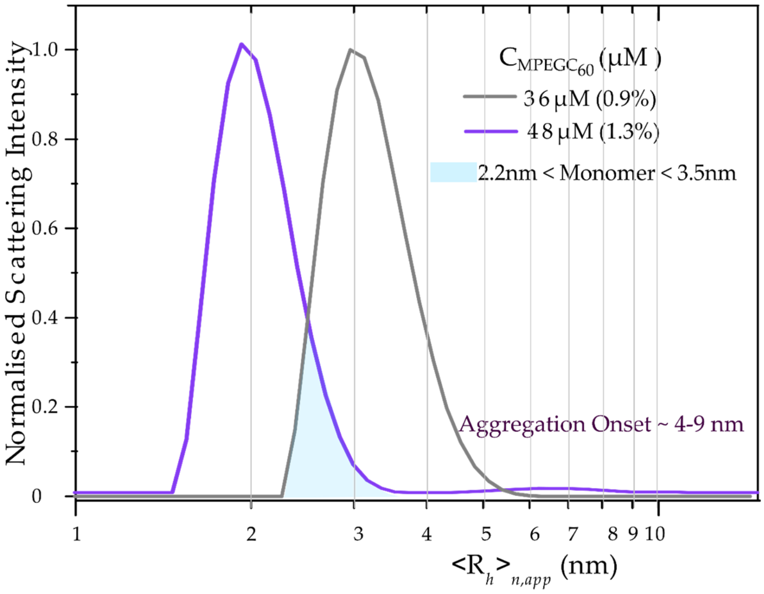

Figure 3—3: Particle Size Distribution at aggregation onset of $MEGC_{60}/CHCl_3$ using Dynamic Light Scattering (DLS).

3.2.2.1 Spin Coated (SC) Films

The ratio of absorbance $A^{256\ nm}/A^{326\ nm}$ between the prominent peak at 256 nm and the peak at 326 nm at 0.9% $MPEGC_{60}$ content in the SC films is, ≈3, virtually identical to the ratio found for the diluted chloroform solutions. However, upon slightly increasing the $MPEGC_{60}$ content to 1.3%, the sharp UV-absorption peak gets weaker and extends to higher energies as shown in Figure 3—4. These spectral changes are assigned to $MPEGC_{60}$-dimers. If the absorption spectra is normalized to the peak at 326 nm (3.6 eV) the prominent peak at 256 nm progressively diminishes upon $MPEGC_{60}$ loading in the spin-cast films, while the broad absorption between 350 and 750 nm systematically increases. Finally, the pristine 100% MPEGC$_{60}$ SC film shows a broad and featureless absorption where the 326 nm absorption actually became the maximum of the absorption spectra as shown in Figure 3—4. Additionally, the peak at 256 nm gets significantly broader due to aggregation of the MPEGC$_{60}$ molecules.

3.2.2.2 Langmuir-Blodgett (LB) films

As discussed above, the dramatic spectral changes upon fullerene loading in MPEGC$_{60}$ SC films are due to sequential formation of dimers, trimers and higher superstructures. In Langmuir-Blodgett films, the hydrophilic MPEG tails adhere to the water surface and the monomeric units tend to orient themselves parallel to one another, at particular surface pressures leading to the formation of small aggregates with identical symmetry. With fullerene loading, a *concentration effect* is witnessed evident by the spectral characteristics. Since, molecular symmetry is constant, the normalized UV-vis absorption of those LB-thin-films shows only small changes with concentration of MPEGC$_{60}$ (see Figure 3—4). Therefore, we assume that the spectral shapes presented in Figure 3—4 are representative for particular dimers and but also higher aggregates of similar symmetries as detailed in the subsequent theoretical section.

3.2.3 Evaluation of spectral differences

It is important to recognize, that supramolecular structures which contribute to spectral differences in SC and LB films can have: a) different size with varying symmetry (present in SC films); b) different size but identical symmetry (present in LB films), and c) different inter-fullerene distances in a particular assembly (present in SC films). Therefore, the overall focus of the next section, is to spectrally disentangle points a), b) and c) based on the available experimental data in Figure 3—4, with adequate theoretical evidence.

Instead of considering superstructures with several possibilities, the starting point to disentangle a), b) and c) is to consider smaller aggregates, particularly dimer structures, which can be treated using TDDFT calculations at fair computational costs. Since LB dimers feature parallelly oriented fullerenes and SC dimers constitute random symmetries, treating dimers with ranging symmetry give evidence of spectral differences at the dimer level.

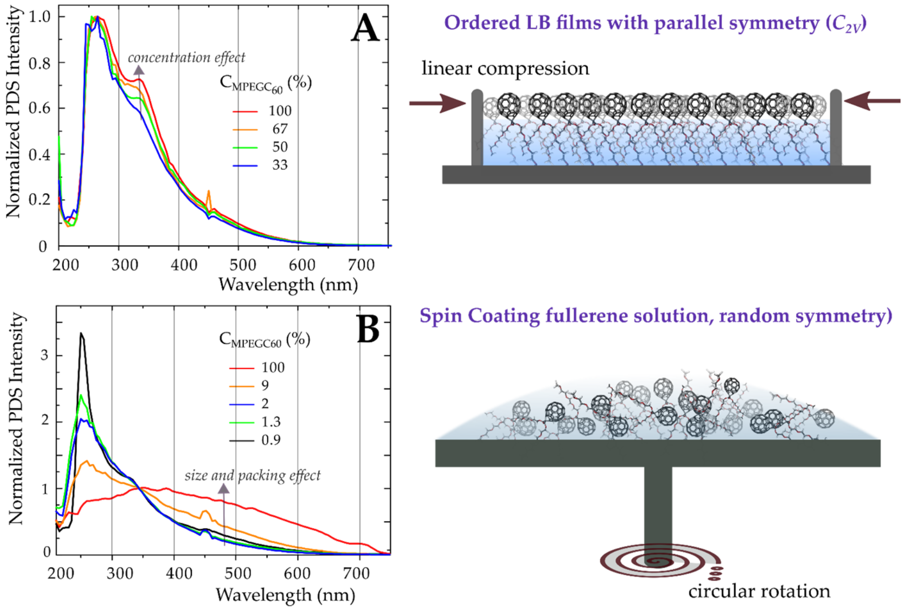

Figure 3—4: (A) PDS spectra on Langmuir–Blodgett films for different MPEGC60/stearic acid concentrations. Concept images on the right explains how LB and SC self-assembly are symmetrically different. (B) PDS spectra for spin-casted films of MPEGC$_{60}$ from CHCl$_3$ solvent for different MPEGC60/stearic acid concentrations, normalized at 344 nm.

Next, at specific symmetries, treating dimers with systematically varied inter-fullerene distances, or packing gives hint about spectral changes, particularly relevant to SC-films at large concentrations. Thus, dimer geometries are assigned to experimental absorption features, followed by theoretical discussions about: 1) Influence of symmetry and 2) Influence of packing. From a quantum chemical perspective, Point 1 considers dimers with specific molecular point group. Therefore a third variable, namely 3) Effect of geometry, or the rotation of one buckyball against another at fixed symmetries and packing is discussed, subsequently.

3.2.3.1 Reduction of Experimental Absorption Features to Dimer Level

The DLS data presented in Figure 3—3 showed the presence of monomers at 0.9% and the SC-film spectrum at the same concentration is identical to single fullerene molecule spectra. Therefore, the 0.9% fullerene films consist of isolated monomers. In contrast, at the onset aggregation concentration of 1.3%, the MPEGC$_{60}$ SC-film, comprises of monomers and dimers of varying symmetries. Counterintuitively, such a hypothesis must hold since, the 1.3% MPEGC$_{60}$ spectra appears broadened *w.r.t.* monomer spectrum, and spectral broadening indicates aggregate formation.

Hence, spectral features of dimers are identified by taking the spectrum of the most diluted spin-cast film (0.9% MPEGC$_{60}$) representative for the monomer spectrum and subtracting this monomer reference from the spectrum of the next higher concentrated spin-cast film (1.3% MPEGC$_{60}$). Figure 3—4 shows that the 256 nm band for the 1.3% MPEGC$_{60}$ film is spectrally broad, especially towards the deep UV-region. Upon subtraction of the monomer spectrum, the UV-absorption at wavelengths shorter than 256 nm is pronounced but the difference spectrum (ΔSC) shows an *unphysical* minimum when approaching balanced weights of the 1.3% and the 0.9% monomer spectra. For a 50% relative weight of the monomer reference spectrum, the UV-absorption at 232 nm (5.3 eV) is marked (*mauve*) (ΔSC spectrum in Figure 3—5). Besides this *unphysical* feature, the spectral signatures above 256 nm absorption basically mimics the LB-absorption spectrum. Because the 232 nm peak is absent in LB-films it can be used as a spectroscopic fingerprint for the identification of various dimer geometries that are absent in LB-films but those which are present only in SC films. Thereby those dimers can be unravelled which exclusively contributes to UV-absorption (LB-type) and those causing intense vis-absorption (SC-type) as shown in Figure 3—5.

3.3 Theory

Fullerene-dimer models are constructed and their absorption spectra are computed by means of TDDFT. To facilitate computations of large sample space at low computational costs, the long MPEG-side chains of the fullerene were trimmed and replaced with shorter substituents (in this case -CN) which mimic the absorption spectra of fullerene single molecules *i.e.* does not alter the electronic structure of the derivative. All calculations are performed using TZV basis set, BP-86 functional with added D3-dispersion interaction correction. At such conditions, about 2700 electronic states are calculated, and about a hundred relevant electronic states are analysed.

3.3.1 Influence of Symmetry

The essential difference between formation of LB and SC-films is their structural symmetry at dimer scales (4-10 nm, *cf.* DLS data Figure 3—3), which contribute to spectral differences at thin-film scales. Absorption spectra of dimers of possible symmetries namely C_s, D_{2d}, D_{2h}, C_{2h}, C_{2v} are computed in Figure 3—5 to assign the essential spectral differences in ΔSC or LB dimer spectrum.

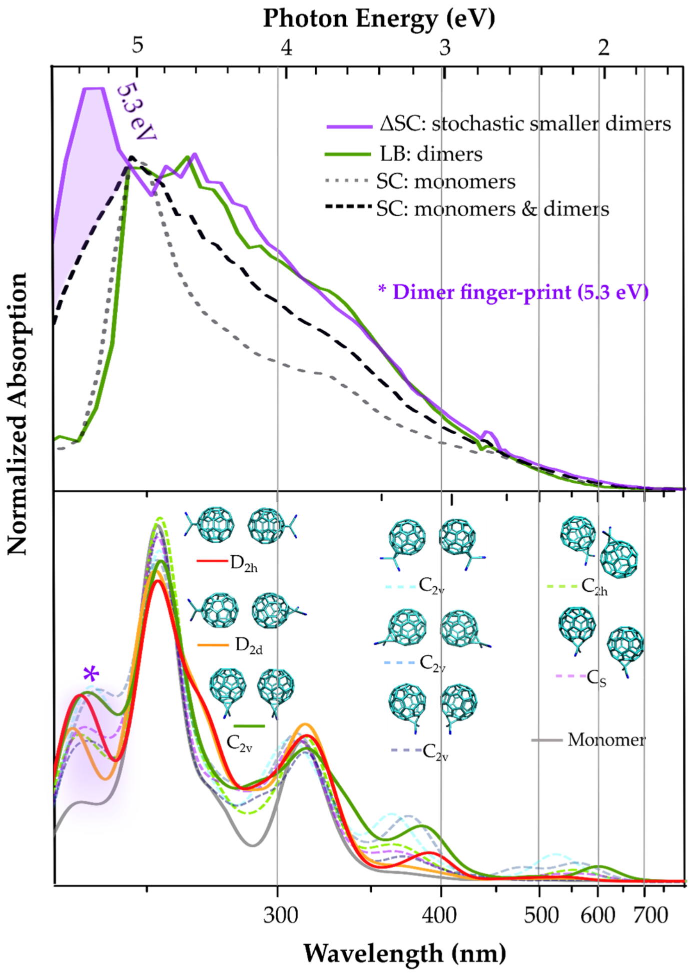

Figure 3—5: Comparing experimental dimer spectra *(top)* to TD-DFT derived spectra of dimers belonging to different symmetry groups *(bottom)*. LB film and spin cast films (SC) with 0.9% and 1.3% MPEGC$_{60}$ content represents monomers and a mixture of monomers and dimers, respectively. Difference spectrum ΔSC is SC-monomer spectrum subtracted from 1.3%-MPEGC$_{60}$ SC film with weights $A(\lambda, c = 1.3\%)/A(\lambda, c = 0.9\%) = 2:1$ to identify fingerprint dimer peak at 5.3 eV. Comparison indicates that the fingerprint peak at 5.3 eV is particularly well resolved for dimers with D_{2d} and D_{2h} symmetries.

All dimers with C_s, D_{2d}, D_{2h}, C_{2h}, C_{2v} symmetry populate SC-dimer film, contributing to the ΔSC-spectrum. In contrast, all C_{2v}-dimer candidates are exclusive representatives of LB type aggregates because their dimer geometries have non-vanishing dipole moments and amphiphilicity which is essential for LB film production. Dimers which are not expected to populate LB films can be filtered in the following way:

a) Dimers belonging to point groups D_{1h}, C_{2h}, D_{2d} least populate the LB films as their anchor PEG tails are projected away from the air-water interface.

b) Dimer C_s too, has minimal chance of formation in a well-assembled monolayer because an imaginary plane cutting the broad bases of the individual fullerenes horizontally, is not parallel to the water surface.

Naturally, the spectroscopic signatures of all dimers with various symmetries contribute to the ΔSC-spectrum, whereas the C_{2v}-dimer to the LB dimer spectrum. Being centrosymmetric (consists of '*i*' symmetry element) in nature, dimers belonging to D_{2h} and the C_{2h} point group shows the weakest vis-absorption (forbidden transition region) of all considered dimers which otherwise would be violation of Laporte's selection rule of symmetry.[162] The spectral features at 3.9 and 4.9 eV are attributed to monomeric fullerene transitions[27] and depend negligibly on the molecular point-group. All remaining spectral signatures are strongly dependent on the dimer symmetry and are classified into four regions of interest: 1.8 to 2.8 eV *(first)*, 2.8 to 3.6 eV *(second)*, 4.4 to 5.2 eV *(third)*, and 5.2 to 5.6 eV *(fourth)*.

The weak absorption feature in the *first* region is a result of HOMO→LUMO transition which largely depends on the dimer symmetry. This feature is particularly prominent for C_{2v}-type dimers, but is clearly Laporte-forbidden for centrosymmetric D_{2h} and C_{2h} dimers as the involved MOs have same parity. These signals are however quite weak and broad in the wavelength scale, which might explain why just negligible absorption differences are present between LB- and highly diluted SC-films below 2.8 eV *cf.* Figure 3—5.

The *second* absorption region are populated by singlet excited states where the nearest adjacent *p*-orbitals between fullerenes interact to varying extents defined the considered geometry and molecular symmetry. Minimum dipole-dipole repulsion occurs in most C_{2v} dimers because of parallel orientation mostly. However, maximum orbital overlap occurs here, resulting in bathochromically shifted low energy transitions with oscillator strengths higher than all other symmetries. With concentration in concentration, the supramolecular size of LB-type structures grow, but with fixed symmetry thereby influencing the vis-spectral region negligibly. Therefore, the remaining dimers in Figure 3—5 and those with similar geometries having a large distribution of intermolecular distances contribute to the vis-absorption of the SC-films at higher concentrations (see Figure 3—4).

The *third* absorption range is characterized by an intramolecular fullerene transition or monomeric transition at 4.9 eV, which is basically isoenergetic with change in molecular symmetry. Lastly, *fourth* region is featured by some monomeric and excitations to overlapped states. This absorption signal lies deep into the UV region for C_{2h}, D_{2h}, and D_{2d} dimers, and appears spectrally well-resolved, particularly for D_{2h} and D_{2d} dimers. This spectroscopic hallmark non-C_{2v} dimers can be thus counted as the likely origin of the experimental peak at 5.3 eV in the ΔSC-spectrum and absent for LB-films. Because pristine SC-films are comprised of dimers with all possible structure *i.e.* both C_{2v} and non-C_{2v} this *peak* is not spectrally resolved but virtually appears like a shoulder.

3.3.2 *Influence of Intermolecular Packing*

From the above discussions, it can be inferred that spectral differences at the dimer-level primarily occurs due to *symmetry effect* resulting in varying inter-fullerene interactions. As mentioned earlier, differently packed dimers exist in SC-films, but not in LB films because they are fabricated at the same surface pressure of 10mN/m. Thus, spectral changes at systematically varying intermolecular distances serves as a metric to explain origins of strong vis-absorption in concentrated SC-films. The SC dimers with varying symmetry are now classified into three categories:

a) Dimers with maximum inter-fullerene interactions and –PEG chains projected away from each other (D_{2d}, D_{2h}).

b) Dimers identical to LB-type structures where the individual monomers in a dimer are oriented parallelly (C_{2v}-dimers).

c) Centrosymmetric dimers, which present Laporte forbidden transitions and do not contribute to enhanced vis-absorption (D_{2h}, C_{2h}).

Upon vdW-dimerization, breakdown of symmetry and π-orbital delocalization effects the weak forbidden visible part of the spectra while the allowed UV-region broadening occurs due to origin to new transitions as discussed above. The forbidden part contains intermolecular delocalized states, which in particular show distance dependence. Therefore, the vis-absorption of D_{2d} and C_{2v} dimers gain intensity progressively as intermolecular distance is systematically reduced up to 2 Å (Figure 3—6). In case of the centrosymmetric D_{2h} dimer, these symmetry forbidden transitions do not escalate upon distance reduction, which otherwise would violate Laporte's selection rule.[162]

To explain the reason of progressively higher vis-absorption upon distance reduction we take the case of dimer D_{2d}. Upon intermolecular distance shrinking at constant point, *i.e.* all rotational degrees of freedom are frozen, interaction between the molecular π-orbitals lead to formation of new bonding and anti-bonding orbitals that are delocalized over the whole dimer. Naturally, electronic excitations that are dominated by transitions involving unoccupied delocalized orbitals with decreased energies as compared to the constituting molecular orbitals, will have lower transition energies than ones of the individual molecules; in case the corresponding HOMO energies change lesser upon dimerization. Thus, electronic transitions associated with these stabilized MOs gets bathochromically/hypsochromically shifted relative to those transitions, which occurs *via* energetically degenerate MOs.

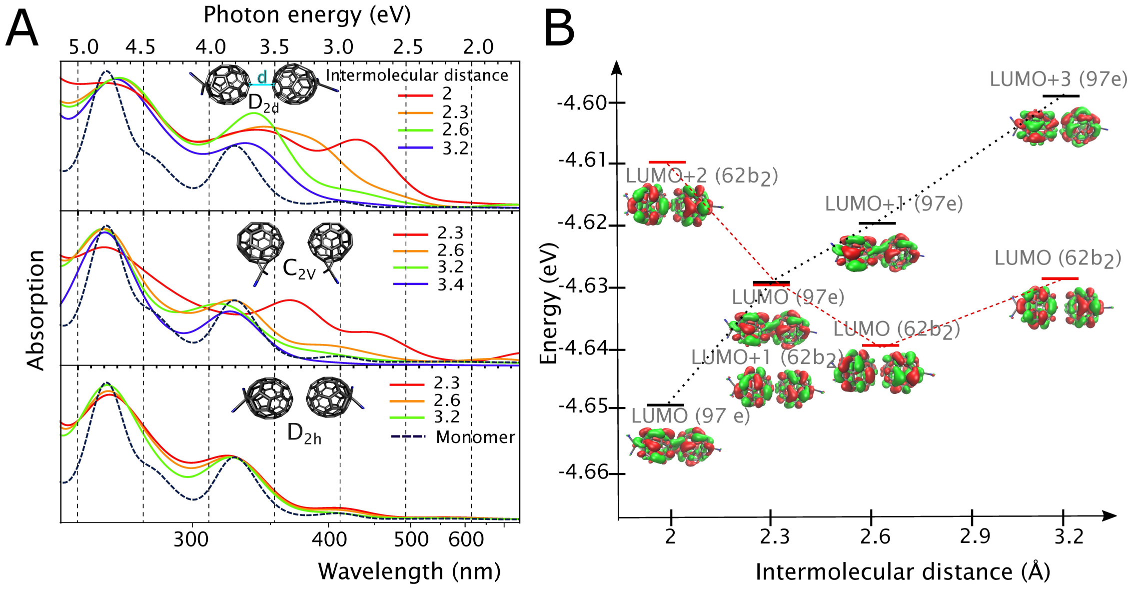

Figure 3—6: *(Left)* TD-DFT-derived UV-vis absorption spectra depending on the intermolecular distance. *(Right)* Exemplary change in orbital energies upon distance reduction as described in preceding text.

Let's take the example of the LUMO (*62b*$_2$) (-4.63 eV) and the LUMO + 3 (*97e*) orbitals (-4.6 eV) for the intermolecular distance 3.2 Å. LUMO+3 (*97e*)[11] involves π-π delocalization as distance shrinks and gets energetically stabilized upon intermolecular distance reduction by 20 meV at 2.6 Å. On further distance reduction, *97e* is systematically stabilized to become the LUMO for the fullerenes separated by 2 Å, in total 50 meV more stabilized than that for 3.2 Å. Electronic transitions to LUMO shifts bathochromically as intermolecular distance diminishes. In contrast, LUMO (*62b*$_2$) (-4.3 eV) at 3.2 Å shifts, first away and then towards vacuum contributing to an overall destabilization of 20 meV at 2 Å. Such delocalized states are frequent in the visible part of D_{2d}'s absorption

---

[11] For a MO representation, for *e.g. 97e*, the suffix *i.e. 'e'* represents the irreducible representation in accordance to character tables. The prefix *i.e.* 97 does not have any physical significance, but is simply the item number in the long DFT molecular orbital output chart (*eiger* file). The number is provided for interested theoreticians to easily identify these specific orbitals from the exhaustive *eiger* list.

spectrum explaining why the low energy transitions shift in energy upon distance reduction. Orbital overlap between the interacting fullerenes does not occur in cases where the nearest hexagonal rings between the fullerenes interact *via* face-to-face interaction. Such interactions are unfavourable due to electrostatically repulsive vdW-surfaces for face-to-face π-stacking, which explains for *e.g.* why benzene dimers are A-B stacked.[163]

3.3.3 *Influence of Geometry*

To simulate a realistic condition depicting dimer orientation in thin-films, all intermediate geometries, between different point groups need to be considered. The *influence of geometry* on optical properties can be understood by rotating one buckyball against another while keeping intermolecular distance and symmetry constant. Because staying in the same point group during rotation is possible only for C_{2V} dimer, this variation is exclusive to the C_{2v}-point group. The starting geometry with dihedral angle (θ) of 84° shows that the nearest pentagonal rings of the individual $C_{61}(CN)_2$ fragments (are slanted towards each other whereas in the optimized geometry with θ =65°, they are oriented face-to-face. This indicates that upon optimization the hexagonal rings adjacent to these pentagonal rings move away from each other (Figure 3—7). This is possibly because π-stacking interaction is destabilized by repulsive quadrupole moments of aromatic rings, but is marginally stabilized by London dispersion interaction. Eight different structures were chosen along the dimer angle optimization trajectory within the C_{2v}-point group (dimer angles θ: 84° (starting geometry), 81°, 77°, 74°, 73°, 70°, 67°, 64° (optimized geometry)) and absorption spectra was computed for each structure (see Figure 3—7).

A gradual blue-shift in the absorption spectra is observed as the dihedral angle decreases upon optimization. The prime electronic transitions in the presented absorption spectra are given by four different regions of interest (first between 1.8 and 2.3 eV, second between 2.9 and 3.3 eV, third between 3.7 and 4.2 eV and the fourth between 4.6 and 5 eV). To investigate and assign specific spectral features the most intense electronic transitions for the four above-mentioned spectral regions are identified.

From these assignments, it is clear that delocalized states diminish as dihedral angle decreases for all four spectral region as mentioned above. For *e.g.*, the first, second and fourth spectral region comprises of delocalized MOs for the initial geometry, but is dominated by monomeric π-MOs for the final geometry. As dihedral angle decreases upon optimization, delocalized orbitals become unstable due to breakdown of linearity of the π-backbone, prohibiting intermolecular charge transfer making delocalized transitions increasingly less probable. Contrarily, because optimization leads the nearest hexagonal rings to move apart in order to reduce quadrupole moment repulsion the monomeric π-transitions governed by b_1-character gain oscillator strength and appear blue-shifted.

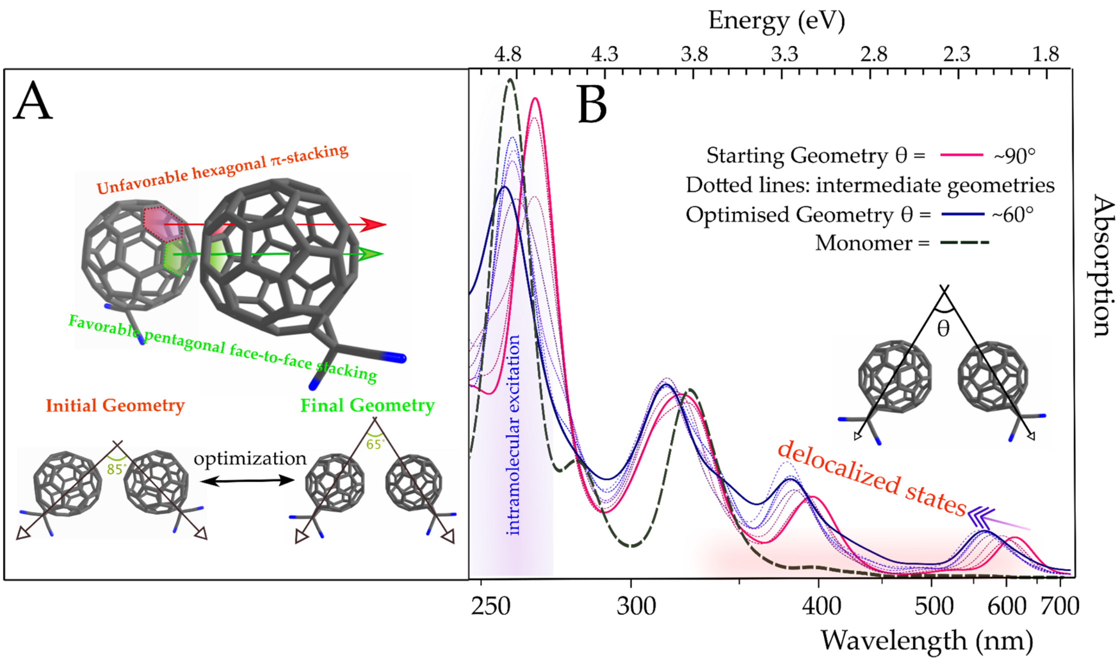

Figure 3—7: (A) Sketch depicting interacting rings between the fullerene interstitial spaces. Pentagonal face-to-face interaction is favored, while hexagonal π-stacking is unfavorable as discussed in text. Geometry optimization keeping symmetry constraint aims to decrease hexagonal stack, *i.e.* tilting of the two fullerenes towards each other or reduction of dihedral angle; (B) TD-DFT electronic absorption spectra for angular C_{2v} dimers as a function of dihedral angle (θ). The blue arrow demonstrates a hypsochromic spectral shift upon optimization for all the four absorption peaks.

3.4 Summary- Optical properties

In this chapter, optical transitions of solutions, LB and SC thin-films and of different vdW dimer structures made using amphiphilic fullerene $MPEGC_{60}$ were studied. The main focus of chapter was to control electronic transitions featured by the change of absorption properties which arise due to supramolecular structure modification. First, the absorption spectra of non-aggregated fullerene solution is compared to the standard PCBM reference molecule and characterized with support from TD-DFT simulated spectra. Then, $MPEGC_{60}$'s aggregate size was systematically enlarged by concentrating/dilution MPEGC$_{60}$ within stearic acid matrix. It was demonstrated that the molecular orientation and order of these fullerene assemblies can be switched between *random disordered-* and *parallel ordered-* orientations in SC and LB films, respectively. The resulting absorption spectra differed vastly. Size increment of LB-type aggregates (C_{2v}-symmetry) caused marginal variations in the UV spectral region which is attributed to concentration effect. In contrast, evolution of stochastic large aggregates in highly concentrated spin-cast films causes vis-absorption to boil up at the cost of UV region until the absorption spectrum covers the whole vis-spectral range homogeneously.

Deeper insights about how aggregate structure evolves, from poorly absorbing monomers to relatively strongly absorbing dimers was derived, by experimentally deconstructing the dimer spectra and comparing it to TD-DFT derived dimer absorption spectra. At 5.3 eV (~234 nm) an absorption peak exclusive to dimers was captured, which either virtually appears like a shoulder, or is strongly resolved depending on the orientation of one fullerene *w.r.t.* another. Because the relative orientation of one buckyball against another matters in determining the thin-film structure and properties made out of them, the effect of intermolecular distance, symmetry and angle was studied subsequently.

Particularly C_{2v} type parallel dimers which dominate LB films feature weakly resolved shoulder while strongly resolved peaks in the UV-fingerprint region are pertinent to D_{2d} and centrosymmetric D_{2h} dimers which are expected to populate fullerene spin-cast films. Next, dimers falling into C_{2v}, D_{2h} and D_{2d} symmetry groups, with sequentially decreasing intermolecular distances and specific intermediate geometries with various intermolecular angles were considered. TD-DFT derived absorption spectra reveals that molecular orientation modifies the nature of intermolecular π-π orbital overlap. This stabilizes/destabilizes specific orbitals and in effect, shifts electronic transitions bathochromically/hypsochromically.

The presented results in this chapter therefore, conclusively justifies that:

- *The common notion of low vis-absorption in fullerene is a misnomer, since it does not hold true if larger aggregates are considered.*
- *Fullerene's electronic transitions can be tailored at will by programming the aggregate symmetry, supramolecular size, intermolecular distance and geometry by designed thin-film fabrication with supramolecular control.*

4 Fullerenes- Morphologically Controlled Supramolecular Assemblies

Parts of this chapter follows from these articles: **P3**– Controlling Intermolecular Interactions at Interfaces: Case of Supramolecular Tuning of Fullerene's Electronic Structure Saunak Das, Julia Preiß, Jonathan Plentz, Uwe Brückner, Moritz von der Lühe, Oliver Eckardt, Andre Dathe, Felix H. Schacher, Eric Täuscher, Uwe Ritter, Andrea Csáki, Gudrun Andrä, Benjamin Dietzek, Martin Presselt. *Advanced. Energy Materials.* 2018, 1801737. **P4**– Progress and Development in Structural and Optoelectronic Tunability of Supramolecular Non-bonded Fullerene Assemblies Saunak Das, Martin Presselt, *(submitted)* 2019

The term 'morphology' in pure one-component systems refers to their symmetry, packing, size and geometry at molecular scales. Self-assembly of these morphologies taking into account intermolecular interactions replicate molecular scale arrangements into defined functional thin-films.[40, 164] The last chapter demonstrates that optical properties of fullerenes are heavily dependent on their morphologies, more precisely, symmetry, packing, geometry and size. There absorption spectroscopy and quantum chemical calculations were used as tools to determine structure/property relationships. Thus, the exact supramolecular structure at the molecular scales was determined implicitly. For an explicit determination of these supramolecular structures, their nanoscopic visualization would be excellent. Furthermore, an additional suite of film fabrication methods can be used to generate ranging structures with diverse morphologies.

The usual approach to produce electroactive active thin-films is spin or drop coating (SC and DC).[154] As described before, the produced structures in such films are uncontrollably large with random molecular symmetries. Additionally, both of these methods yield amorphous films and therefore are coupled with post-processing steps like annealing to induce film crystallinity, control thickness, and eliminate residual solvents.[165] Thus for high-functional solution-processed SC films a number of control parameters require optimization *viz.* spinning frequency, time, casting solvent, ramp and annealing time, steps temperature, inert/ambient atmosphere. In contrast, interfacial self-assembly is an excellent one-step platform for controlled growth of molecular morphologies.

In this thesis, liquid (water)-gas (air) interface is utilized in Langmuir-Blodgett technique, while self-assembly at liquid interfaces is enabled by Liquid-Liquid

Interfacial Precipitation (LLIP).[12] Therefore, in comparison to pure solution processing on solid supports, the supramolecular framework can be pre-defined prior to thin-film deposition. Using a vertically (Langmuir-Blodgett)[166] or horizontally (Langmuir-Schäfer)[167] moving substrate along the interface or by drop/spin-coating these pre-defined morphological frameworks (LLIP) are deposited on solid supports. In addition, drop or spin coating, with or without post-processing annealing at chosen temperatures, are used to compare all thin-film morphologies.

The current chapter has the following goals:

- Preparation and detailed morphological analysis of fullerene assemblies at the nanoscale.
- To control intermolecular distance, shape and spatial extent of these fullerene assemblies by tuning the chemical nature and size of the interface.
- Absorption measurements on thin-films to understand how supramolecular structure controls optical properties.

4.1 Morphology Investigation

Seven different MPEGC$_{60}$ morphologies are mediated on three solid supports by Drop Coating (DC), Spin Coating (SC) with/without annealing, Langmuir-Blodgett (LB) and Liquid/Liquid Interfacial Precipitation (LLIP). The supports include quartz (for AFM and UV/vis characterizations), Cu-grid (for TEM studies), Glassy Carbon Electrodes (for electrochemical measurements). Finally, these are processed on amorphous Silicon surfaces for hybrid solar cells as detailed in the subsequent chapter.

4.1.1 Drop Coating

Upon evaporation of the mediator CHCl$_3$ solvent, unique vesicular structures are observable in MPEGC$_{60}$ films (Figure 4—1). Thermodynamically favourable bi-layered vesicular assembly are expected to form for fullerenes with two hydrophilic tail groups in accordance to Israelachvili's packing theory.[168] These vesicles have a uniform diameter of 655±60 nm, a 5 nm ridge, and feature the same phase as the surrounding smooth film. The slow DC thin-film formation, likely facilitates formation of thermodynamically favourable morphologies.

---

[12] Further details on these methods can be found in Methods (Chapter 2)

4.1.2 *Spin Coating*

SC generates films with amorphous morphology. Here, the supramolecular structures likely reorganize, first locally to energetically more favourable morphologies. Thus, the MPEGC$_{60}$ thin-films obtained by SC show a heterogeneous morphology as revealed by AFM (Figure 4—1). Specifically, two morphologies of interest are noted, namely, dome-shaped large clusters, and amorphous portions of the constituting thin-film. Statistical grain analysis discloses aggregates with diameter d_{SC} = 619±52 nm, which feature different supramolecular orientations as revealed by the AFM phase images in Figure 4—1. These surfaces must comprise one of the two constituting MPEGC$_{60}$-moieties, *i.e.* either the bucky balls or the PEG-chains of the MPEGC$_{60}$ amphiphiles.

4.1.3 *Thermal Annealing*

To relieve interfacial tensions and induce crystallinity within amorphous SC films, a post-processing step for 15 min at three different temperatures (85°C, 165°C and 220°C) is introduced. Both temperature and time duration are kept within what is used in traditional fullerene semiconductor processing.[169-170] Figure 4—2 provides a schematic structure evolution upon annealing.

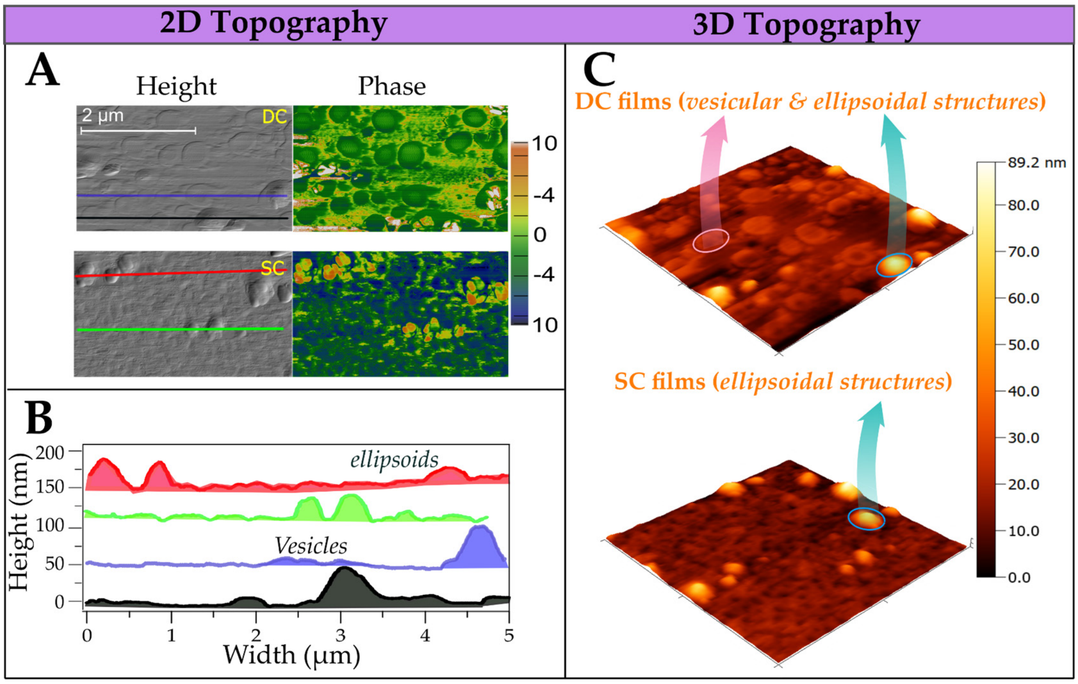

Figure 4—1:(A) Comparison between AFM derived height and phase images of Drop Coated (DC) and Spin Coated (SC) films; (B) line profiles, *cf.* topographies in (A), depicting heights of morphologies; (C) 3D views of vesicular and ellipsoidal dome like structures.

The SC morphology discussed in the preceding section is first homogenized upon annealing at 85°C. This proceeds *via* disruption of large and unstable SC aggregates, and simultaneous release of trapped solvents (*cf.* boiling point of $CHCl_3$ - 61.2°C), leading to crystalline domains. Grain analysis indicates presence of aggregates with $d_{SC}^{85°C}$=67±26 nm, which at higher annealing temperatures aggregates grow in size up to $d_{SC}^{220°C}$=282±31 nm. A similar evolution of aggregate sizes with annealing of spin-casted indene-C_{60} bisadduct (ICBA) films has been reported before.[171] In addition to aggregate growth, annealing inherently drives supramolecular structures to their thermodynamically most favourable geometry. Those structures likely involve as many intermolecular interactions per molecule as possible, such as realized in closed shell packing of $MPEGC_{60}$ with the PEG-chains possibly filling the interstitial volumes.

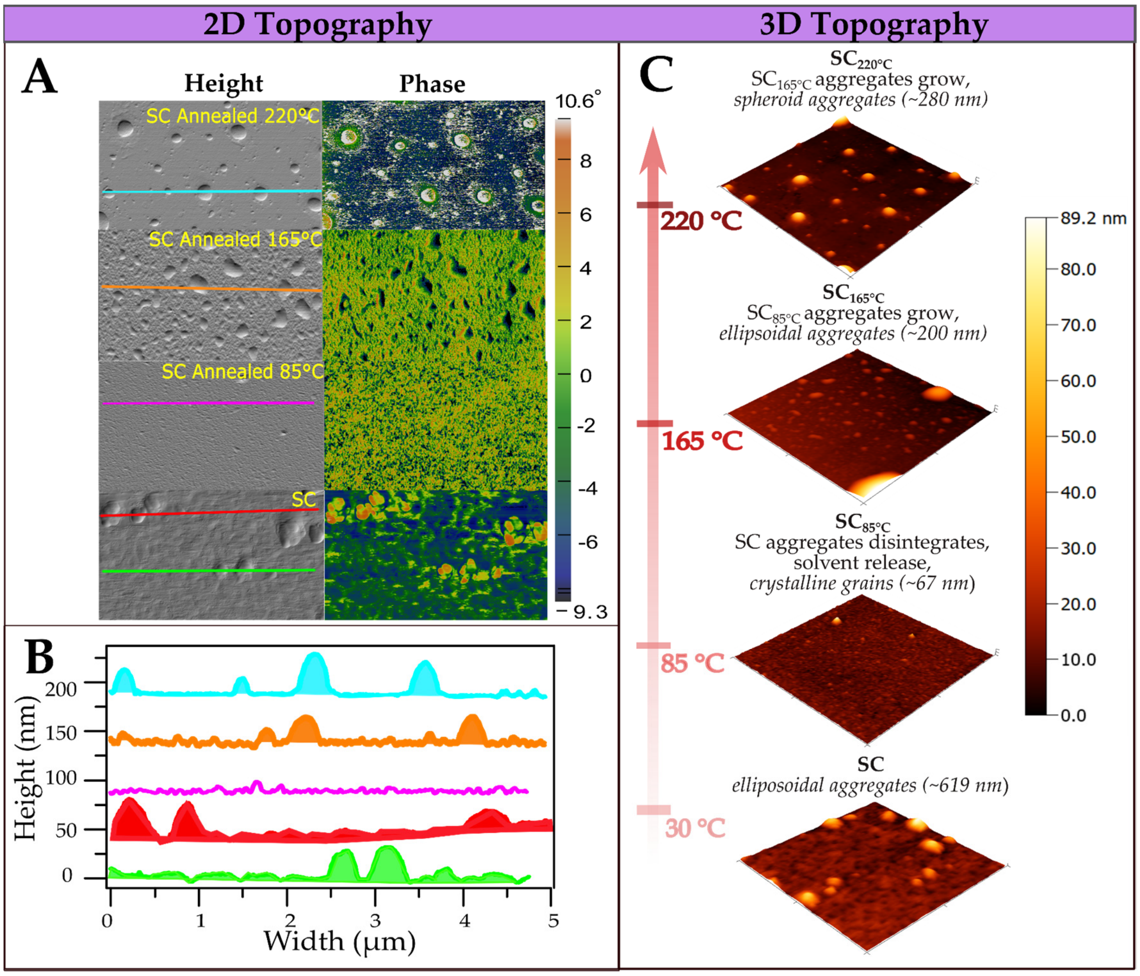

Figure 4—2: Structure evolution of SC films upon annealing; (A) height and phase images and (B) line profiles on specific portions of A, elucidating morphological heights, and (C) 3D topography demonstrating structure evolution upon annealing.

4.1.4 *Langmuir Blodgett Technique*

Due to its characteristic amphiphilicity, *cf.* the electrostatic potentials at the vdW surface of MPEGC$_{60}$ in Figure 4—3, its molecular structure has sites with preferential affinity to polar/non-polar media, a prerequisite for the formation of a LB layer. This section shall deal with a prototype LB monolayer as determined by the theoretical unit cell arrangement.[13]

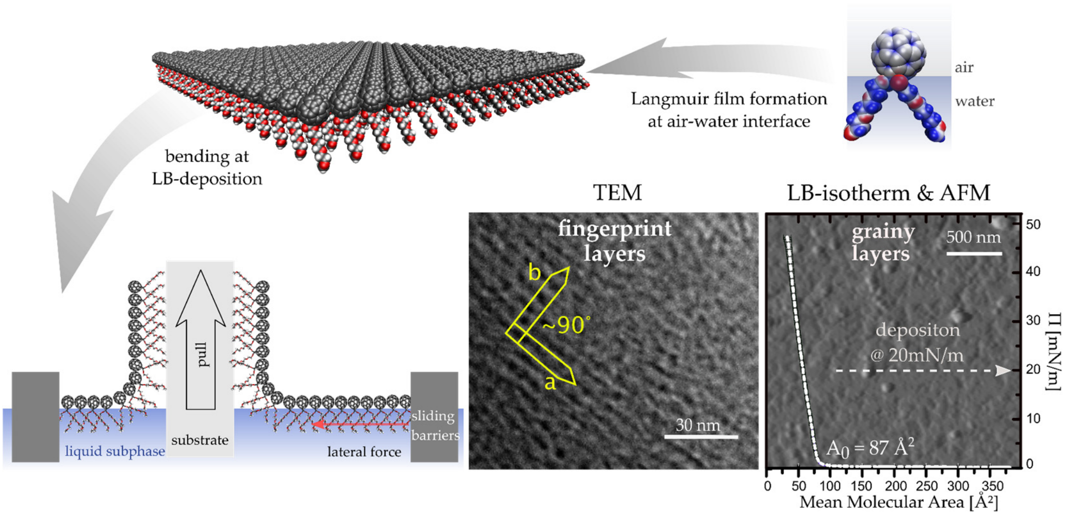

Figure 4—3: Molecular structure and distribution of the electrostatic potential Φ (-0.04 - 0.04 a.u.) at the vdW surface of MPEGC$_{60}$; the supramolecular structure exemplifies that MPEGC60 amphiphiles can assemble at air-water interfaces to extended 2D-layers which are deposited on suitable substrates *via* Langmuir-Blodgett (LB) technique demonstrated pictorially. TEM images on these deposited films demonstrates fingerprint like structure. Langmuir isotherm is overlaid on the AFM image of the deposited film.

Lateral compression leads to distinctive molecular assembly upon shrinking of the molecular area available for each MPEGC$_{60}$-molecule and is characterized by increasing surface pressures Π, as shown in Figure 4—3 (left part, bottom: Π(A)-isotherm overlaid with AFM topography image). The Langmuir monolayers were deposited at a moderate surface pressure of Π_{LB}=20 mN/m, *cf.* Π at Langmuir monolayer collapse $\Pi^{collapse}$=45 mN/m. Thus, the resulting AFM topography is generally smooth and homogeneous. Occasionally, certain grainy structures with mean diameters of 101±20 nm are observed. Deeper insights into the actual supramolecular geometry are gained by determining the mean molecular area A_0 of individual MPEGC$_{60}$-molecules in a relaxed Langmuir layer *via* extrapolating the linear part of the isotherm. From the derived A_0=87 Å² area unit cell

---

[13] Fundamental descriptions about Langmuir Blodgett (LB) technique is provided in Chapter 2.

lengths between a_{tetra}=9.3 and a_{hexa}=10.0 Å are obtained for prototypical tetra- and hexagonal closed shell packing pattern (according $A_0=a_{tetra}^2 \sin 90°$, $A_0=a_{hexa}^2 \sin 60°$, respectively) in Langmuir monolayers (see Figure 4—3).

Explicit confirmation of the exact packing pattern was obtained *via* TEM performed on LB layer modified Cu-grids (Figure 4—3). TEM reveals that the deposited films feature fingerprint-like morphologies comprised of quasi-linear MPEGC_{60} assemblies with rather non-specific phase relation. These aligned fullerenes feature high local but less global ordering. The distance within and between the MPEGC60-rows were obtained statistically by drawing line profiles. The obtained values are, a=9.6±0.6 Å (within rows) and b=10.2±0.5 Å (between rows) respectively. Multiplying and taking sine (a*b*sin60°~85 Å^2), yields unit cell areas, practically very close to the intermolecular distances in the two prototype closed shell packing(s) (87 Å^2) (see Figure 4—3) deduced from the LB isotherm.

4.1.5 *Liquid-Liquid Interfacial Precipitation*

LLIP assembly is a 2-D self-assembly process similar to LB technique where instead of utilizing the liquid/gas interface like LB, occurs across the interface of two liquids with contrasting polarities, here between $CHCl_3$ and CH_3OH.[14]

MPEGC_{60} was dissolved in the good solvent $CHCl_3$ and a large volume of CH_3OH was added dropwise at temperatures closer to the $CHCl_3$ boiling point (~55°C). This induces a tendency for $CHCl_3$ to evade the solution phase while CH_3OH start to dissolve the polar –PEG tails. Using extended sonication for ~30 min, larger supramolecular fragments disintegrates leading to formation of ordered nanostructures. Dynamic light-scattering (DLS) in solution phase provides evidence of structures with two sets of hydrodynamic radii ($<R_h>$): 4-10 nm and between 100 nm - 1 μm (Figure 4—4). AFM together with TEM experiments compliments DLS data on thin-films revealing that formation of fullerene nanowires (AFM: d_{LLIP} = 75 - 100 nm), nanosheets (AFM, TEM: length=200 nm – 2 μm) and flaky structures, as shown in Figure 4—4. Interfacial precipitation leads to formation of 2D-domains, which furl upon sonication to yield MPEGC_{60} nanowires.

A comparison between the packing and supramolecular ordering between the LB and LLIP 2D-sheets suggests differences in unit-cell packing, and supramolecular order.

---

[14] Further details about the basics of LLIP method are provided in Chapter 2.

Information on the lattice constants are obtained by drawing line profiles, similar to that of the LB morphology. For the LLIP case, MPEGC$_{60}$ rows (direction 'a' in Figure 4—4), have larger lattice constants within (a=17.8±1.6 Å) and between (b=23.2±2 Å). Since, the proportion of CH$_3$OH is 10x larger by volume than fullerene dissolving CHCl$_3$ the PEG tails are better solubilized and space out leading to the large inter-fullerene distances (a=17.8±1.6 Å) as illustrated in Figure 4—5. This fullerene separation is not observed in LB films where fullerene- fullerene contacts are enforced by the external lateral pressure, at a given concentration.

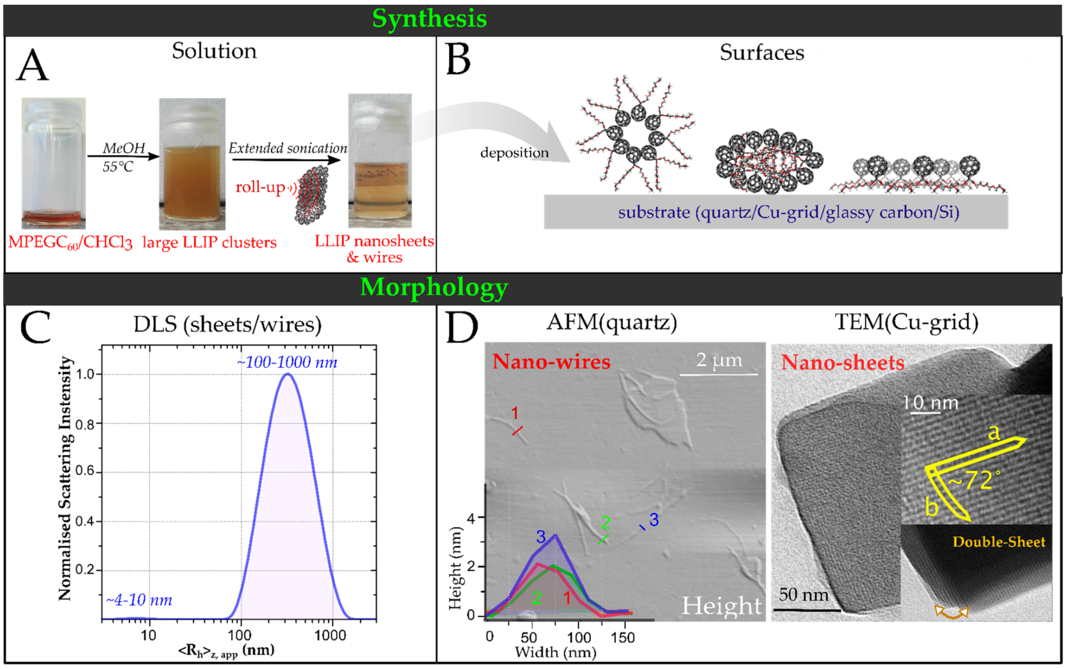

Figure 4—4: (A) Synthesis of ordered LLIP structures, evinced by the change in colour of MPEGC$_{60}$/CHCl$_3$ solution from wine red to murky brown which upon extended high power sonication leads to the formation of light brown solution comprising nanosheets and wires; (B) LLIP structures are transferred to surfaces by drop coating article; (C) and (D) Morphology of synthesized LLIP structures: (C) shows the particle size distribution in solution studied by DLS, and (D) shows morphology of LLIP structures on quartz glass showing wires and flake-like structures (AFM) and on Cu-grid showing ordered 2D single and double nanosheets (TEM)

Though both LB and LLIP layers feature linearly organized fullerenes, supramolecular order is considerably different (see Figure 4—5). While the buckyballs are organized linearly over hundreds of nanometres along each LLIP nanosheet (direction 'a'), in LB layers the linearity is broken within a row for distances larger than 20-30 nm(s). Thus, while methods demonstrate excelled molecular organization at the nanoscale, LLIP nanosheets exhibit more uniform spatial order in comparison to LB layers.

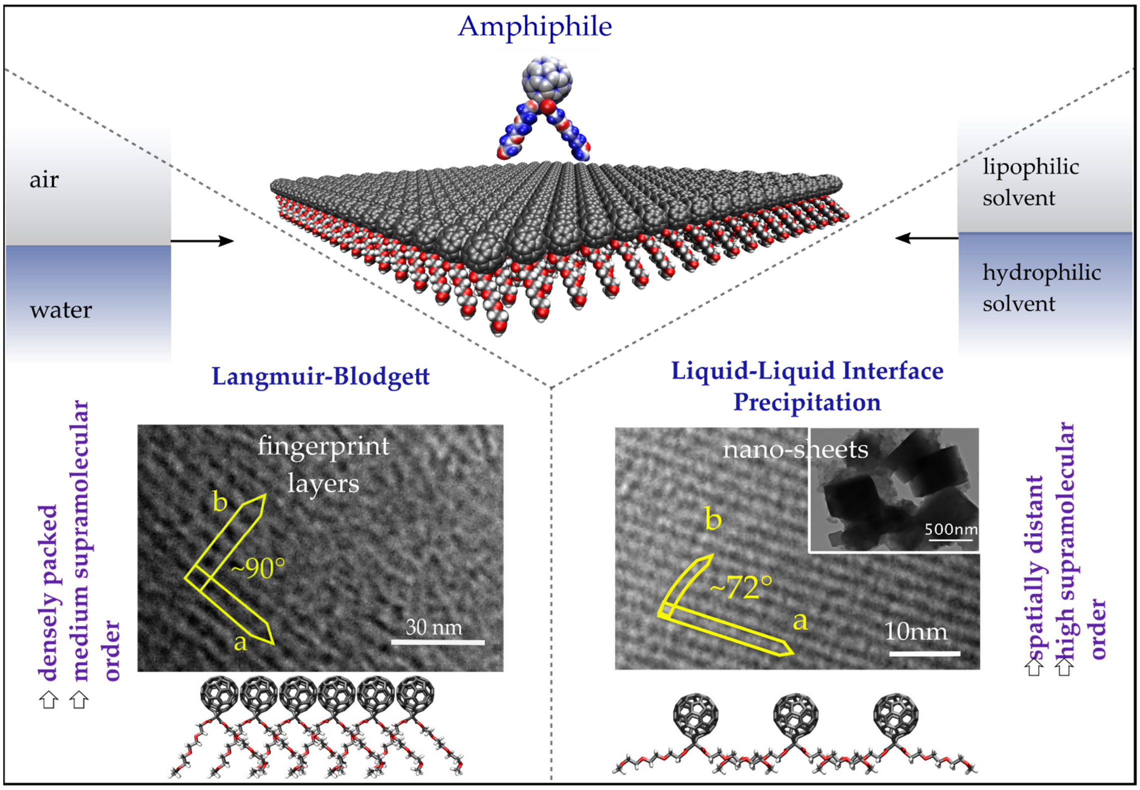

Figure 4—5: Comparing interfacial formation and supramolecular structures of LB and LLIP films using TEM. LB produces densely packed finger-print like layers which have locally organizes into close packed motifs with medium supramolecular order, while LLIP produces 2D nanosheets with 1-2 µm size, spatially distant but featuring high supramolecular order.

4.2 Structure Property Relationships

The morphologies discussed above vary substantially in terms of molecular arrangement and dimension based on preparation methods. These method dependent fullerene morphologies are classified based on their structural features through the following acronyms: grainy morphology (gr), sheets (sh), wires (wi), vesicles (ves), distant and ordered (dis/or), closed shell packing (csp). Thereby, the structures are given by: $LLIP_{sh,wi\,|\,dist}$, $LB_{sh\,|\,csp}$, $DC_{gr,ves\,|\,csp}$, $SC_{gr\,|\,csp}$, $SC^{85\,℃}_{gr\,|\,csp}$, $SC^{165\,℃}_{gr\,|\,csp}$, $SC^{220\,℃}_{gr\,|\,csp}$. Correlating UV-vis absorption spectra to these morphologies (on quartz substrates) provides information about supramolecular geometries[172], symmetry[119, 173], and aggregate size.

4.2.1 *Correlating Optical Property to Morphology*

Correlating UV-vis absorption spectra to these morphologies (on quartz substrates) provides information about supramolecular geometries,[172] symmetry,[119, 173] and aggregate size. The spectral changes (Figure 4—6) induced by the morphology, *cf.* symmetry, geometry and packing as introduced in Chapter 3 is governed by particle in a box model.[174-175] The following effects are apparent:

a) Reduction of the supramolecular symmetry causes increased vis- and decreased UV-absorption according to the Herzberg-Teller intensity borrowing (HTIB) mechanism.[72, 159, 173]

b) Aggregate growth and reduction of intermolecular distances causes an apparent red-shift due to increased π-π states, giving rise to low-energy electronic transitions, *cf.* Figure 3—6.[123]

These effects mentioned in points a) and b) were previously observed while systematically varying MPEGC$_{60}$ supramolecular size through fullerene loading in non-chromophoric matrices, *cf.* Chapter 3. Point a) was particularly encountered while comparing the spectral features of symmetry independent SC and parallelly oriented MPEGC$_{60}$ in LB films. Effect b) was witnessed while comparing the spectral features of MPEGC$_{60}$/stearic acid SC films as a function of fullerene loading. Instead of diluting/concentrating the thin-film sample, in the current chapter, different interfaces were utilized to vary the supramolecular structure within MPEGC$_{60}$ thin-films. To understand the spectral and electronic properties (next chapter) of these morphologies, it is essential to recollect how their explicit supramolecular properties varied based on preparation methods. Therefore, these morphologies are represented based on their structural features by using simple acronyms[99] (also see footnote[15]).

The spectra have been normalized to the absorption peak at 345 nm, which corresponds to an allowed electronic transition of C$_{60}$ that is rather insensitive to differences between morphologies[27], to facilitate comparison between the spectra of the films with different

---

[15] Shape and packing is separated by | symbol and multiple structures in the same film by comma. Representations are grainy (gr), sheets (sh), wires (wi), vesicles (ves), distant (dist), closed shell packing (csp). Final acronyms are given by: $LLIP_{sh,wi|dist}$, $LB_{sh,gr|csp}$, $DC_{ves,gr|csp}$, $SC_{gr|csp}$, $SC^{85°C}_{gr|csp}$, $SC^{165°C}_{sp,gr|csp}$, $SC^{220°C}_{sp,gr|csp}$. Note, that these acronyms are used only when specific structure/property relations are drawn. For all other cases the original short forms, *e.g.* LLIP, LB etc. are used.

thicknesses. While the $LB_{sh,gr|csp}$, $SC_{gr|csp}$, and the first annealed $SC^{85°C}_{gr|csp}$ films show the weakest vis-absorption, the latter gets systematically enhanced upon annealing the $SC_{gr|csp}$ films and reaches the maximum vis-absorption of all films after annealing at 220°C. As shown above in Figure 4—7, supramolecular size of SC assemblies increases by 3-4 times upon annealing. The UV-peaks of these annealed samples do not red-shift significantly upon annealing. Thus, aggregate growth cannot be the only possible explanation to account for observed rise in the vis-absorption. Secondly, the HTIB mechanism can operate via reduction of supramolecular symmetry leading to the increase of vis-absorption at the expense of UV-absorption. However, if supramolecular symmetry at molecular scales within the aggregate core remains unchanged upon annealing, then HTIB mechanism will not be able to explain annealing induced absorption changes. A plausible reasoning for the increased vis-absorption upon annealing can be thus explained by denser molecular packing, *i.e.* reduction of mean intermolecular distances in non-centrosymmetric supramolecular structures, which enhances vis-absorption but influences the UV-absorption marginally.[125]

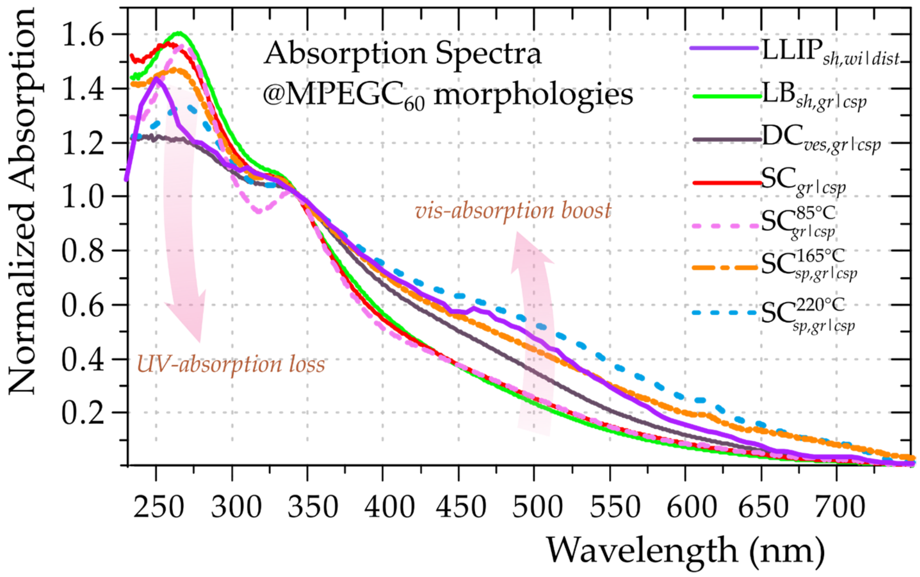

Figure 4—6: Thin-film absorption spectra of MPEGC_{60} supramolecular assemblies *cf.* Figure 4—7 on quartz glass.

The comparison of $LLIP_{sh,wi|dist}$ and $LB_{sh,gr|csp}$ spectra provides further information about their distinct supramolecular structural features, despite both being 2D assembly processes. The red-shift of the UV-peak ($LLIP_{sh,wi|dist}$: 250 nm, $LB_{sh,gr|csp}$: 270 nm) is in accordance with extended 2-D assembly across the substrate surface in $LB_{sh,csp}$ as compared to 0.1-1 µm long sheets in $LLIP_{sh,wi|dist}$ films. Because $LB_{sh,gr|csp}$ feature denser molecular packing (unit cell area of LLIP LB ~ 4 times LB) and lesser 2D order, these factors cannot account for the differences in relative vis-absorption. Consequently, a reduced supramolecular centrosymmetry in case of $LLIP_{sh,wi|dist}$ as compared to $LB_{sh,gr|csp}$ films, because of $LLIP_{sh,wi|dist}$ layer buckling and formation of nanowires, (Figure 4—4) is the likely origin of larger vis-absorption of $LLIP_{sh,wi|dist}$ as compared to $LB_{sh,gr|csp}$ films.

4.3 Summary- Morphological Properties

The goals set at the beginning of the current chapter are now reviewed in retrospect. Specifically, using a suite of four interfacial engineering methods, controlled fullerene growth was achieved in terms of buckyball orientation, molecular packing, supramolecular order and size. The films fabricated at 2D interfaces were found to assemble into globally ($LLIP_{sh,wi|dist}$) or locally ($LB_{sh,csp}$) ordered nanosheets containing fullerenes at *large* ($LLIP_{sh,wi|dist}$) or *closely packed* ($LB_{sh,csp}$) intermolecular distances. Thermally annealed films evidently demonstrated crystalline and densely packed domains than amorphous DC or SC films. Statistical grain analysis revealed the varying supramolecular size and shape of these assemblies, *viz.* ellipsoidal domes (SC films), vesicles (DC), spherical aggregates ($SC^{165^\circ C}$, $SC^{220^\circ C}$), crystalline grains ($SC^{85^\circ C}$, LB), nanowires (LLIP) and 2D-sheets (LLIP and LB).

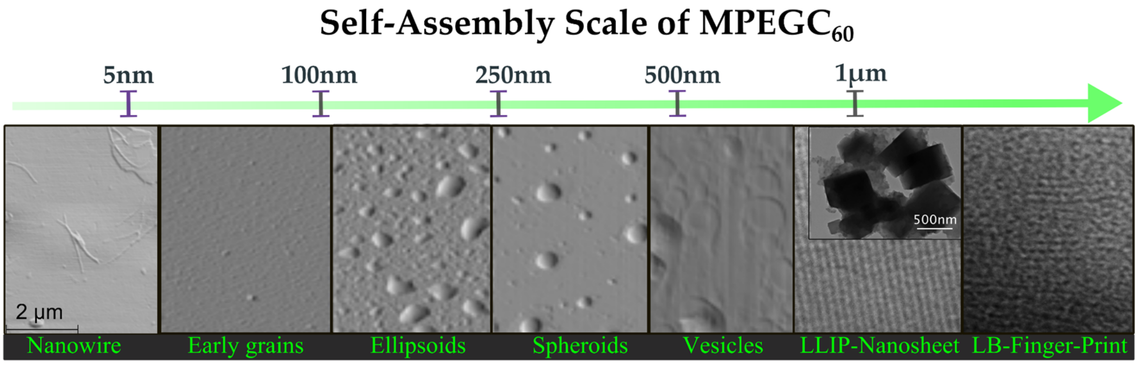

Figure 4—7: Length scale to demonstrate that the size of synthesized supramolecular MPEGC$_{60}$ structures range from the nano, meso to microscales.

UV-vis studies of these morphologies on thin-films indicate that both aggregate size and molecular packing influences vis-absorption, in particular. In comparison, the allowed UV part of the spectra shows minute changes, except for $LLIP_{sh,wi|dist}$ morphology featuring blue-shifted well-resolved UV- and enhanced vis-absorption. These diverse self-assemblies occur at length scales ranging from a few nm (height of nanowires ~ 4 nm) to a few hundred nanometres (width of vesicles = 619 nm). Finally, the goals set for this chapter are met and a length scale assigned to these supramolecular fullerene structures can be introduced (Figure 4—7). Conclusively, *morphological control of MPECG*$_{60}$ *supramolecular assemblies is achieved by interfacial self-assembly*.

5 Fullerenes- Electronically Controlled Supramolecular Assemblies

Parts of this chapter are taken from these articles: **P3** – Controlling Intermolecular Interactions at Interfaces: Case of Supramolecular Tuning of Fullerene's Electronic Structure Saunak Das, Julia Preiß, Jonathan Plentz, Uwe Brückner, Moritz von der Lühe, Oliver Eckardt, Andre Dathe, Felix H. Schacher, Eric Täuscher, Uwe Ritter, Andrea Csáki, Gudrun Andrä, Benjamin Dietzek, Martin Presselt. *Advanced. Energy Materials.* 2018, 1801737. **P4** – Progress and Development in Structural and Optoelectronic Tunability of Supramolecular Non-bonded Fullerene Assemblies Saunak Das, Martin Presselt, *(submitted)* 2019

Fullerene's strong electron accepting property is primarily attributed to its low-lying LUMO energies.[19, 126, 176] The five-fold degenerate HOMO and three-fold degenerate LUMO with small energy-gap offer the possibility to accept up to six electrons by a single buckyball.[19] Fullerenes usually accept electrons from photoexcited electron donors like polymers and convert into fullerene anions.[20] These anionic species comprise of low lying excited states (~0.2-0.4 eV), which promotes further exciton separation without affecting the charge recombination rate.[146] Also, the electron mobility in fullerene thin-films is impressive (up to 6 cm^2/V-s) if compared to other organic molecules.[177] Furthermore, both charge transfer and migration occurs isotropically, and thus FA thin-films are not limited by structural rigidity like NFAs.[28] In spite of these beneficial qualities, few serious drawbacks limit the full potential of fullerenes, which is why FAs can be used only in conjunction to certain electron donors. These limitations, detailed below serve as an impetus behind the focus of this chapter.

In 2014, Shubina and coworkers, demonstrated that fullerene vdW dimers act as electron traps in their anionic forms.[149] A general consensus about binding energies in the light of bonding theory is, that covalent bonds are strong and hence feature appreciably larger binding energies than that of vdW stabilization energies which is usually between 0.4-4 kJ/mole. However, DFT calculations demonstrated that singly reduced vdW fullerene dimer anions present a binding energy of ~16-28 kal/mole, which is significantly larger than the binding energy of covalently bonded Diels-Alder's cycloadduct fullerene dimer.[149] It was observed that the redox process of the singly reduced dimeric species is irreversible, particularly that re-oxidation of the first reduction is non-feasible. This indicated the formation of $(C_{60})_2^-$ charge traps. Presence of vdW fullerene dimers, which usually populate thin-films (see section 3.2.3.1) are thus detrimental for functional devices.

Reducing fullerene/fullerene interaction is carried out by substituting functional groups, minimizing disordered aggregation. This disrupts the degeneracy of the electronic states in C_{60} without affecting the nature of the orbitals, but influences LUMO energy. For *e.g.* the phenyl butyric acid derivatized C_{60} (PCBM) is 80-90 mV more difficult to reduce, featuring more stable LUMO *w.r.t.* pristine C_{60}, whereas both their HOMO-energies remain constant at 6.2 eV[122,174, 178] Thus with side chain modification in fullerene, aggregation reduces but their electronic properties are heavily compromised. Furthermore, higher electron affinities with limited energy levels in fullerenes reduce the choices of potential electron donor candidates due to energy level mismatch.

These limitations, in summary: a) formation of electron traps, b) uncontrolled FMO-energies in derivatives, and c) higher electron affinities, have initiated the demand for fullerene derivatives with tailored electronic properties for photovoltaic applications.[176] An ideal precondition to achieve high cell voltage in such a solar cell is to have the fullerene LUMO far in energy from the donor HOMO, *i.e.* closer to the donor LUMO.[179] Next, spatially separated fullerenes, but with high supramolecular order would be essential to prevent dimeric traps and boost mobility.[180] Finally, if the above goals can be achieved from the same fullerene derivative by supramolecular structure variation, efforts in the design and quest of newer derivatives can reduce. Therefore, the primary goals of this chapter are listed as follows:

a) To track FMO energy variation for the morphologically controlled fullerenes nanostructures presented in Chapter 4.
b) To derive a fundamental model for understanding how morphology is connected to electronic property.
c) To test the applicability of the model in real devices, *i.e.* to validate the above structure/property relationship in photovoltaic devices.

5.1 Electrochemical Properties

Hence, the evaluation of fullerene morphologies discussed in the thesis is done based on the following steps. First, CV of $MPEGC_{60}$ in solution is discussed and then SWV is performed on fullerene thin-film morphologies grown on glassy-carbon working electrode. Ferrocene is used as standard in each case and the correction offset factor is chosen to be 5.1 eV (about the mean of 4.8 and 5.3 eV scales proposed by Cardona[129]) for determination of HOMO/LUMO energies. These experimental data is discussed and analysed with support from DFT calculations.

5.1.1 Solution

Electrochemically MPEGC$_{60}$ in solution (see Figure 5—1) can be triply reduced up to (MPEGC$_{60}$)$^{-3}$ associated with two well-resolved CV peaks at -0.7 and -1.1 V, and a third indistinct reversible reduction wave is noticeable at -1.6 V qualitatively similar to that of PCBM and a mono PEG, mono-benzyl substituted C$_{60}$.[122, 181]. From the onset of the first reduction feature (-0.51 eV) the ELUMO was noticed at 4.3 eV when corrected to vacuum scale with a scaling factor of 5.1 eV.[129] The Fc/Fc$^+$ one-electron reduction couple's half-reduction potential ($E_{1/2}$) was 0.3 eV against Ag/AgCl reference electrode.

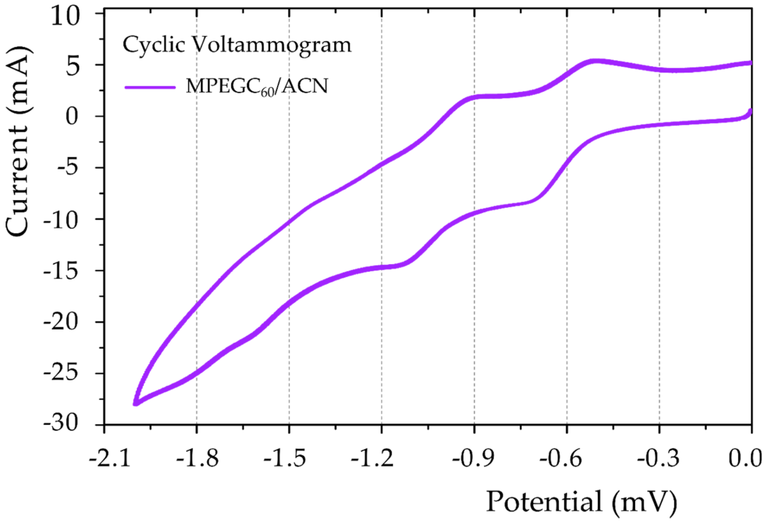

Figure 5—1: CV of MPEGC$_{60}$ in dry ACN *vs.* Ag/AgCl featuring three reversible reduction peaks.

5.1.2 Thin-films

For SWV-measurements, a standard three-electrode-cell system, comprising of a solid glassy carbon electrode substrate as the working electrode (30 × 5 × 1 mm^3), Pt-wire as counter, and Ag/AgCl wire as quasi-reference electrode, were used. The electrode surface was surface immobilized with thin-film fullerene morphologies, established in Chapter 4, namely, $LLIP_{sh,wi\,|\,dist}$, $LB_{sh\,|\,csp}$, $DC_{gr,ves\,|\,csp}$, $SC_{gr\,|\,csp}$, $SC_{gr\,|\,csp}^{85°C}$, $SC_{gr\,|\,csp}^{165°C}$, $SC_{gr\,|\,csp}^{220°C}$. These freshly prepared chemically modified electrodes were fitted to a self-designed electrode cell, along with the reference and auxiliary electrodes immersed in electrolyte for SWV measurements.

The voltammograms in vacuum scale are depicted in Figure 5—2 and the corresponding redox- ($E_{red/ox}$), half-wave- ($E_{1/2}$), onset- (E_{onset}), against Ag/AgCl and Fc/Fc$^+$ reference, with corresponding HOMO and LUMO energies are presented in Table 1. The onset potentials are deduced by line-fits from multiple data points from repeat measurements and herein, the standard deviation for a particular sample is due to variation in FMO energies because of a distribution of morphologies on working-electrode surface.

The analysis suggests that the redox properties of MPEGC$_{60}$ supramolecular structures varies strongly with thin-film preparation methods. The first reduction and oxidation signals are observed at ~-0.6 V and ~1.7 V (deviation ~150 mV) respectively against Ag/AgCl whereas the standard Fc/Fc$^+$ potential at ~0.4 V. Considering Koopman's theorem is applicable,[182] negative of the determined electron affinities/ionization energies determines LUMO and HOMO energies respectively. $LLIP_{sh,wi\,|\,dist}$ has the highest LUMO energy at -4.28 eV, whereas, LUMO of DC films are most stabilized at -4.4 eV. Similarly, the HOMO of $LLIP_{sh,wi\,|\,dist}$ is observed at -5.92 eV, whereas, as the DC HOMO is more stabilized (-6.29 eV). The FMO energies for rest of the morphologies lie between these two extremes. Thus, supramolecular structure and morphology tuning enable shifting FMO energies by tens, up to hundreds of meV.

Table 1: Squarewave voltammetry data of MPEGC$_{60}$ morphologies *versus* Ag/AgCl reference; Sorted for decreasing LUMO energies. For values *versus* the Fc/Fc$^+$-reference and the evaluation of mean HOMO/LUMO energies done statistically from multiple measurements see section 3 of SI. Note that the half-wave oxidation potential of $LB_{sh\,|\,csp}$ morphology is left undetermined due to physically broad oxidation wave signal.

Morphology	$E^{Ag/AgCl}_{onset,red}$ (V)	$E^{Ag/AgCl}_{onset,ox}$ (V)	$E^{Ag/AgCl}_{1/2,red}$ (V)	$E^{Ag/AgCl}_{1/2,ox}$ (V)	$E^{Fc/Fc^+}_{1/2}$ (V)	**HOMO (eV)**	**LUMO (eV)**	$\lvert\Delta HOMO - LUMO\rvert$
$LLIP_{sh,wi\,|\,dist}$	-0.40	1.23	-0.55	1.63	0.40	-5.92	-4.28	1.64
$SC^{165°C}_{gr\,|\,csp}$	-0.44	1.20	-0.63	1.66	0.30	-5.95	-4.29	1.66
$SC^{220°C}_{gr\,|\,csp}$	-0.29	1.37	-0.50	1.97	0.50	-5.90	-4.32	1.58
$SC^{85°C}_{gr\,|\,csp}$	-0.43	1.29	-0.59	1.89	0.35	-6.04	-4.33	1.71
$LB_{sh\,|\,csp}$	-0.34	1.24	-0.49	-	0.45	-5.93	-4.33	1.6
$SC_{gr\,|\,csp}$	-0.44	1.24	-0.53	1.81	0.30	-6.07	-4.37	1.7
$DC_{gr,ves\,|\,csp}$	-0.43	1.45	-0.62	1.62	0.30	-6.29	-4.40	1.89

The electrochemical data of the non-annealed samples reveal that, LUMO energies shift away from vacuum as grain size increases in order: $LLIP_{wi\,|\,dist} > LB_{gr\,|\,csp} > SC_{gr\,|\,csp} > DC_{gr,ves\,|\,csp}$. However, the relationship between aggregate size and FMO energies for annealed samples does not seem to be size-dependent. For *e.g.*, $SC^{220°C}_{gr\,|\,csp}$ features spheroid aggregates with diameters of ~300 nm which is about a hundred nm larger than

$SC_{gr\,|\,csp}^{165°C}$ grains, but the former's LUMO is 30 meV destabilized. Since with annealing, the intermolecular packing increases, along with grain-size increment, *cf.* Figure 4—2 it can be hypothesized that both aggregate and packing sizes can play a role, in determining FMO energies. Therefore, to support the size-dependency rule, and understand the influence of intermolecular packing DFT based quantum chemical calculations, are performed, as detailed in the following section.

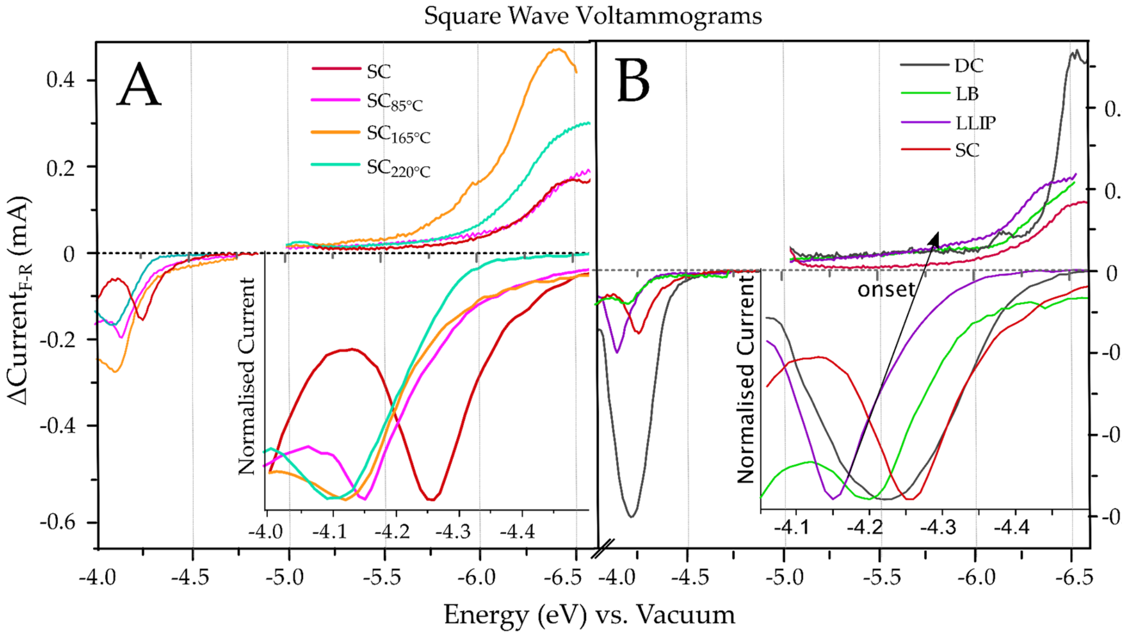

Figure 5—2: Squarewave voltammograms of MPEGC$_{60}$-modified glassy carbon electrodes showing the first reduction and oxidation processes for (top) DC, SC, LB and LLIP films, and (bottom) thermally annealed SC films, in 0.1 M TBABF$_4$/CH$_3$CN solvent. The representative plots are given relative to vacuum using the Ferrocene (Fc)/Ferrocenium (Fc$^+$) reference system for each measurement.

5.2 Theory

DFT based computations are performed to understand: a) the influence of aggregate size, and b) the influence of intermolecular packing. Here, the fullerene C$_{61}$(CN)$_2$, with truncated PEG-tails established in Chapter 3 is recalled as a suitable model for MPEGC$_{60}$. To address point a), monomer, dimer, trimer, a tetramer, *i.e.* $(C_{61}(CN)_2)^N$, with *N=1-4* is considered, constructed in a way to ensure maximum nearest neighbour interaction, through the buckyballs. For point b), dimers with D$_{2h}$, D$_{2d}$, and C$_{2v}$ are considered, and their intermolecular distances are varied to obtain binding energy profiles. Considering electron affinities are more important for acceptor materials,[176] like fullerene the main focus is to formulate a correlation between supramolecular structure and shift in LUMO energies.

5.2.1 *Influence of aggregate size*

The LUMO energy stabilization upon increasing the number of nearest neighbours reported by Fernándes Torrente *et al.*[123] (ΔE_{LUMO}=65 meV) was reproduced qualitatively through our quantum chemical calculations as shown in. Figure 5—3. The DFT calculations shows that the average lowering of LUMO energies per fullerene unit is given by $\Delta E_{LUMO} \approx$ 109±40 meV for vacuum conditions. To represent the solvent environment during SWV experiments, screening of surface charges by a polarizable continuum model for medium with infinite permittivity was considered using the commonly used COSMO.[101] This yielded smaller LUMO energy differences of $\Delta E_{LUMO} \approx$ 43±20 meV.

5.2.2 *Influence of intermolecular packing*

The dissociation tail of vdW-potentials is determined by relaxing distant molecules to the energetically most favourable structure, while the molecular fusion branch of the vdW-potential is determined by relaxing the dimer starting from very short distances.[149] These optimizations are restricted by keeping the point groups fixed, ensuring maximum fullerene interactions namely, D_{2h} and D_{2d}. From the resulting vdW-profiles as shown in Figure 5—3 the observed binding energy minima is found to be typically shallow (between 2.9-3.2 Å) with energies of 27.4 and 26.9 kJ/mole for dimers with point groups D_{2d} and D_{2h}, respectively. Considering the $C_{61}(CN)_2$ molecular dipoles, the intermolecular parallel dipole-dipole interaction is expected to be more repulsive in C_{2v} than D_{2h} or D_{2d} dimers.. These dimers thus demonstrate similar binding energies derived using two variation methods; a) by constrained distance variation and, b) natural relaxation. However, corresponding ΔE_{LUMO} variation (average of ΔE_{LUMO} variation in D_{2d} and D_{2h} dimers) upon intermolecular distance changes accessible in room temperature (as shown in Figure 5—3) is negligibly small (±3 meV) (see Figure 5—3).

Therefore, intermolecular distance variation in a small dimer system, alone cannot explain the 120 meV shift in LUMO energies, for the different morphologies. It is chemically intuitive that one cannot disentangle packing from size, because the former occurs at the expense of later. Secondly, the chemical environment experienced by the bulk of a molecular aggregate is substantially different than the surface. This implies, that simple intermolecular distance/size variation through DFT is inefficient in quantifying the electrochemically derived LUMO data. Thus, a mathematical model is needed to identify and satisfactorily quantify the experimental changes in LUMO energies, *cf.* Table 1. In the next sections, first the mathematical model is conceptualized, and then an equation is derived to correlate supramolecular structure with LUMO energies.

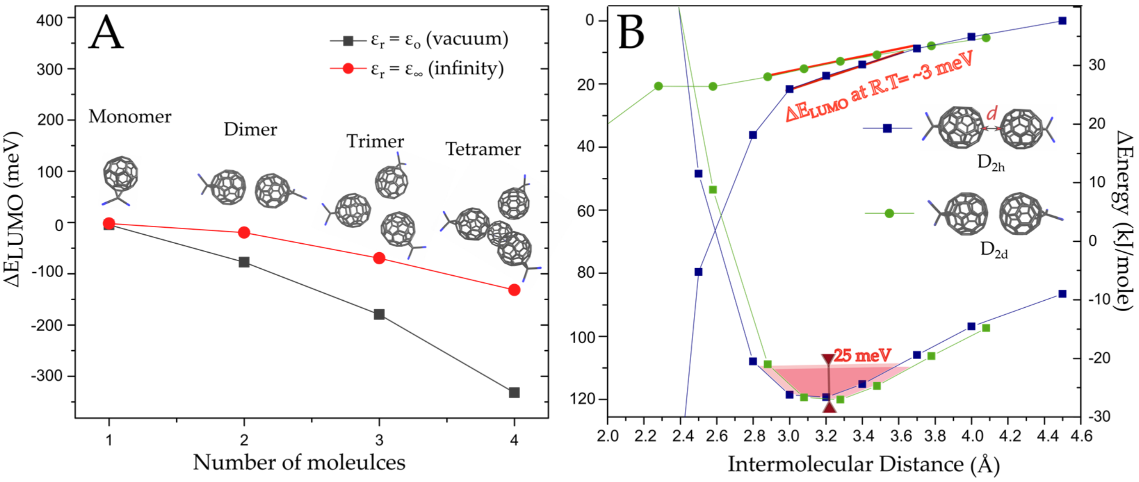

Figure 5—3: (A) Change in LUMO energies relative to monomer with increasing number of molecules calculated by means of TDDFT (SVP/BP86) for molecular clusters with increasing size being in vacuum and in a solvent with infinite relative permittivity (ε_r). (B) Influence of packing density on dimer binding energy *(right y-axis)* and LUMO energies *(left y-axis)* for $C_{61}(CN)_2$-dimers computed using TDDFT (TZV/BP86). Shaded part in red in the energy profile represents thermally accessible energy change with respect to intermolecular distance at room temperature. Zero on the right y-axis refers to non-interacting monomers (separated by 90 Å) and the 25 meV shaded area depicts thermal energy at room temperature.

5.3 Morphology *vs.* Electronic Property

In case of a simple hexagonal C_{60}-monolayer on a gold surface in vacuum each of the six neighbours of a C_{60} fullerene causes a stabilization of the fullerene's LUMO energy by $\Delta E_{LUMO} \approx 65$ meV, as determined experimentally by means of scanning tunnelling microscopy.[123] The mean number of nearest neighbours ($\bar{N}_{nn}$) also increases with growth of three-dimensional aggregates because the bulk/surface ratio increases. This gives the trend of decreasing LUMO energies for increasing aggregate sizes as detailed in the previous sections.

5.3.1 *Molecular Bulk vs. Surface State equation*

At this point, it is shown, that, mean LUMO energy can be formulated as a function of the aggregate's diameter d, height h, and the effective LUMO energy difference $\Delta N_{nn}\Delta E_{LUMO}$ between bulk and surface states (with ΔN_{nn} being the difference in nearest neighbours and ΔE_{LUMO} the difference in the LUMO energy between bulk and surface states, respectively).[16] Derivation of such a function is based on an axiom that all aggregate shapes are special cases of ellipsoids. The following parameters are considered, to describe a typical aggregate:

N_{surf}= number of molecules on the surface; N_{bulk}= number molecules at the bulk; $A_{Aggregate}$=surface area; $daggr, h$= diameter and height; $V_{Aggregate}$= volume; d_i=diameter of $MPEGC_{60}$

Calculation of the number of surface molecules:

$$N_{surf} = \frac{A_{Aggregate}(daggr - di, h - di)}{A_{perMonomer}}$$

$$= \frac{2\pi(daggr - di)\left(daggr - di + \frac{(-di + h)^2 \mathrm{ArcSinh}\left[\frac{\sqrt{(daggr - di)^2 - (-di + h)^2}}{-di + h}\right]}{\sqrt{(daggr - di)^2 - (-di + h)^2}}\right)}{di^2}$$

Calculation of the number of bulk molecules:

$$N_{bulk} = \frac{V_{Aggregate}(daggr - 2di, h - 2di)}{V_{perMonomer}} = \frac{4\pi(daggr - 2di)^2(-2di + ha)}{3di^3}$$

Here 'd_{aggr}' and 'h' are the diameter and height of the aggregate, respectively; 'di' is the diameter of the molecule. Therefore, the ratio of number of bulk to surface molecules gives:

$$\frac{N_{bulk}}{N_{surf}} = \frac{2(daggr - 2di)^2(-2di + h)}{3(daggr - di)di\left(daggr - di - \frac{(di - h)^2 \mathrm{ArcSinh}\left[\frac{\sqrt{(daggr - h)(daggr - 2di + h)}}{di - h}\right]}{\sqrt{(daggr - h)(daggr - 2di + h)}}\right)} \qquad (1)$$

The average energy of the LUMO, *i.e.* E_{LUMO}^{mean}, is calculated as follows:

---

[16] The derivation of this equation was jointly done with Dr. Julia Preiβ and Dr. Martin Presselt.

$$\mathrm{E}_{LUMO}^{mean}=\frac{N_{bulk}\mathrm{E}_{LUMO}^{bulk}+N_{surf}\left(\Delta E_{LUMO}\mathrm{N}_{nn}+\mathrm{E}_{LUMO}^{bulk}\right)}{N_{surf}+N_{bulk}}$$

Here E_{LUMO}^{bulk} is the energy of the LUMO of the bulk molecules and ΔE_{LUMO} is the energy difference per nearest neighbor. N_{nn} is the number of nearest neighbors. This can be rewritten to show the dependence of the average energy of the LUMO from the ratio of number of bulk to surface molecules (By expansion with $\frac{1}{N_{surf}}$:

$$\mathrm{E}_{LUMO}^{mean}=\frac{\frac{N_{bulk}}{N_{surf}}\mathrm{E}_{LUMO}^{bulk}+\left(\Delta E_{LUMO}\mathrm{N}_{nn}+\mathrm{E}_{LUMO}^{bulk}\right)}{1+\frac{N_{bulk}}{N_{surf}}}$$

$$\mathrm{E}_{LUMO}^{mean}=\frac{\mathrm{E}_{LUMO}^{bulk}\left(1+\frac{N_{bulk}}{N_{surf}}\right)+\Delta E_{LUMO}\mathrm{N}_{nn}}{1+\frac{N_{bulk}}{N_{surf}}}$$

$$\boldsymbol{\mathrm{E}_{LUMO}^{mean}=E_{LUMO}^{bulk}+\frac{\Delta E_{LUMO}\mathrm{N}_{nn}}{1+\frac{N_{bulk}}{N_{surf}}}} \tag{2}$$

Additionally, putting equation (1) into equation (2), one get the direct dependence of the average energy of the LUMO from the aggregate size (h and d_{aggr})

$$\mathrm{E}_{LUMO}^{mean}=E_{LUMO}^{bulk}+\frac{\Delta E_{LUMO}\mathrm{N}_{nn}}{1+\frac{2(\mathrm{daggr}-2\mathrm{di})^{2}(-2\mathrm{di}+\mathrm{h})}{3(\mathrm{daggr}-\mathrm{di})\mathrm{di}\left(\mathrm{daggr}-\mathrm{di}-\frac{(\mathrm{di}-\mathrm{h})^{2}\mathrm{ArcSinh}\left[\frac{\sqrt{(\mathrm{daggr}-\mathrm{h})(\mathrm{daggr}-2\mathrm{di}+\mathrm{h})}}{\mathrm{di}-\mathrm{h}}\right]}{\sqrt{(\mathrm{daggr}-\mathrm{a})(\mathrm{daggr}-2\mathrm{di}+\mathrm{h})}}\right)}}$$

In the next section, it is demonstrated that Equation (2) can be used to described the LUMO energy variation for all MPEGC$_{60}$ morphologies.

5.3.2 *Supramolecular LUMO energies*

Equation (2) features a hyperbolic relation between the ratio between the number of bulk and surface states ($N^{bulk}/N^{surface}$) to LUMO energies rather than the actual morphological dimensions dimensions. Defining $N^{bulk}/N^{surface}$ as ξ:

$$\mathrm{E}_{LUMO}^{mean}=E_{LUMO}^{bulk}+\frac{\Delta E_{LUMO}\mathrm{N}_{nn}}{1+\xi}$$

Figure 5—4 represents the dependence of E_{LUMO} on ξ which can be thought of as a morphological term factor and can be obtained from grain-sizes, and aggregate height deduced from AFM analysis of the individual analysis. $SC^{annealed}$samples feature aggregates with two size ranges (categorized as A for small and B for larger aggregates) which contribute to two different ξ-values. DC aggregates being the largest in size feature maximum bulk states, and its LUMO energy determined electrochemically, *cf.* Table 1 is taken as an estimate for the bulk LUMO energy E_{LUMO}^{bulk}=-4.40 eV (measured for $DC_{gr,ves\,|\,csp}$ films).

Considering ΔN_{nn}=3, *i.e.* difference in the number of nearest neighbours between bulk and surface states in a hexagonal packing pattern, and ΔE_{LUMO}=65 meV (Fernándes Torrente *et al.*[123]), the pale blue function in Figure 5—4. is obtained. Most of the morphological term factors in Figure 5—4 is in qualitative agreement with this function apart from $SC_{gr\,|\,csp}$, $SC^{165°C}_{gr\,|\,csp}$, and $SC^{220°C}_{gr\,|\,csp}$. To understand the ξ-values of these films either large effective LUMO energy difference *i.e.* $\Delta N_{nn}\Delta E_{LUMO}$ of ~1.2 eV is needed to be considered or E_{LUMO}^{bulk} energies need to vacuum shift till ~-4.30 eV, as shown in Figure 5—4, respectively. The physical interpretation is that: the SC films constitutes; a) Different $\Delta N_{nn}\Delta E_{LUMO}$ energies as compared to the interfacially grown films, and/or b) Supramolecular structure with higher bulk electron affinity.

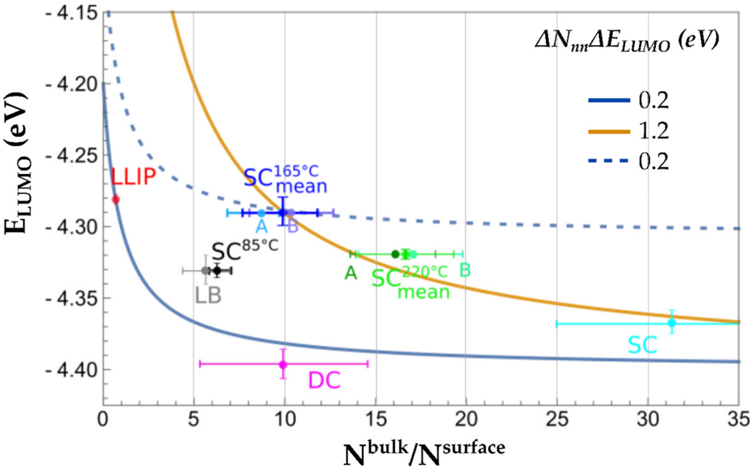

Figure 5—4: Dependence of the mean E_{LUMO} on the ratio between bulk and surface molecules $N^{bulk}/N^{surface}$ for different values of effective LUMO energy differences between bulk and surface states $\Delta N_{nn}\Delta E_{LUMO}$. Offsets, *i.e.* the bulk LUMO energy, of -4.40 eV (solid lines) and -4.30 eV (dashed lines) are assumed. Experimental data with error bars as determined electrochemically and *via* AFM are included for comparison.

a) *Different $\Delta N_{nn}\Delta E_{LUMO}$ energies as compared to the interfacially grown films*: For most supramolecular structures, based on tetra- and hexagonal molecular assemblies values of ΔN_{nn}=1-3 are reasonable, but can increase to extreme values of ΔN_{nn}=12-1=11, if the bulk can be described by hexagonal closed-shell packing of equal spheres and fullerenes at the surface are just connected *via* a single nearest neighbour to the bulk. Therefore, $\Delta N_{nn}\Delta E_{LUMO}$ of ~1.2 eV might be imagined as seen in Figure 5—4. Accordingly, the effective LUMO energy differences of all morphologies fall within these expected limits ($0.2<\Delta N_{nn}\Delta E_{LUMO}<1.2$).

b) *Supramolecular structure with higher bulk electron affinity*: Because LUMO is stabilized with rising nearest neighbour interactions and fullerene intermolecular distances,[17] it can be considered that E_{LUMO}^{bulk} variation can also be possible for the different MPEGC$_{60}$ thin-films. The basis of this argument is that, an increase in E_{LUMO}^{bulk} can impel from weakened fullerene-fullerene interactions, *i.e.* less number or larger distances between nearest neighbours. However, such an increase in E_{LUMO}^{bulk} energies upon annealing seems to be far-fetched because annealing usually produces well packed structures, evinced by their large vis-absorption *cf.* Figure 4—6.

This section particularly demonstrated that LUMO energies strongly depend on supramolecular structure of an aggregate. The differences in the mean LUMO energies is ascribed to varying aggregate sizes and packing geometries captured by the morphology term factor ξ, and effective LUMO energy change between bulk and surface sites, quantified by $\Delta N_{nn}\Delta E_{LUMO}$, while varying E_{LUMO}^{bulk} energies seemingly has a minor impact. These results of particular importance because one can at will tune the electron affinities of fullerene superstructures by adjusting morphology term factor ξ. Therefore, aggregates with larger surface states, *i.e.* extended surfaces push LUMO energies towards vacuum.

In an ideal solar cell made out of these fullerenes, their changes in LUMO energies would closely relate to the overall open-circuit voltage (V_{OC}) (see next section). Additionally, the established fullerene structures with tailored optoelectronic properties can improve photovoltaic performance. In the light of the above considerations amorphous-Si/fullerene based hybrid solar cells are fabricated.

5.4 Fullerene Morphologies in Hybrid Solar Cells

The prime goal of this section is to demonstrate that the LUMO-energy tunability of MPEGC$_{60}$ morphologies established in this dissertation, can cause linear changes in the open-circuit voltage of a solar cell where these fullerene morphologies serve as the n-type layer. This section stimulates discussion on Current (I)-Voltage (V)-characteristics of amorphous Si/fullerene hybrid solar cells, which are influenced by supramolecular

---

[17] Fullerene centre to centre intermolecular distances can be typically large ranging from 10 to 20 Å, *cf.* Figure 4-5.

order and packing. The photovoltaic design requisites to achieve these milestones are the following:

a) A bilayer active layer is preferred, so that the synthesized amphiphilic fullerene morphologies do not degrade into intercalated mixed donor:acceptor phases.

b) Because the fullerene morphologies were grown and characterized on hydrophilic quartz substrates, the surface polarity of the donor deposited anode must be similar, such that the investigated morphologies are retained.

c) The donor deposited anode must offer a rigid and flat surface for reasonable surface coverage with MPEGC$_{60}$. Therefore, hole-only reference devices *i.e.* devices without fullerenes is needed to be characterized in order to i) simulate the influence of pin-holes, a pertinent problem giving rise to short-circuits, and ii) demonstrate how far, morphologically controlled amphiphilic fullerenes improve/deteriorate, photovoltaic performance.

d) The difference in Fermi energies (E_f) of the fullerene and the donor before contact *i.e.* the barrier of the minority carrier injection determines the cell's built in potential (V_{bi}), which is connected to the open-circuit voltage (V_{OC}). Therefore, the band energies of the donor and acceptor fullerenes should be reasonably positioned to allow interfacial charge transfer, for functional photovoltaics.[179]

Keeping the above points in consideration, hydrogenated amorphous Si (a-Si:H) was chosen as the ideal p-doped donor candidate, for a-Si:H/MPEGC$_{60}$ photovoltaics.[24] To simulate the influence of pin-holes[18] and compare how far fullerenes influence HSC performance, *cf.* point d, the fullerene layer was replaced by highly n-doped a-Si:H (10 nm) for two reference solar cells. The HSC design, with the corresponding band energies before contact, is provided in Figure 5—5.

5.4.1 Current – Voltage Characteristics

Figure 5—6 shows the current voltage (IV) curves in and Table 2, the deduced photovoltaic parameters, namely maximum and mean V_{OC}, (from 12 solar cells), fill factors (FF), short circuit current density (J_{SC}) and power conversion efficiencies (η) under illumination.

---

[18] Pin-hole is a commonly used term in photovoltaics meaning presence of tiny cracks/holes in mainly in the absorber layer.

Standard p-i-n a-Si:H solar cells are fabricated in vacuum, but fullerene layer deposition necessitates exposure to ambient conditions/water for interfacial MPEGC$_{60}$ deposition. This leads to the formation of higher interface defect densities and a weak S-shape in the IV-curve as seen from Figure 5—6.

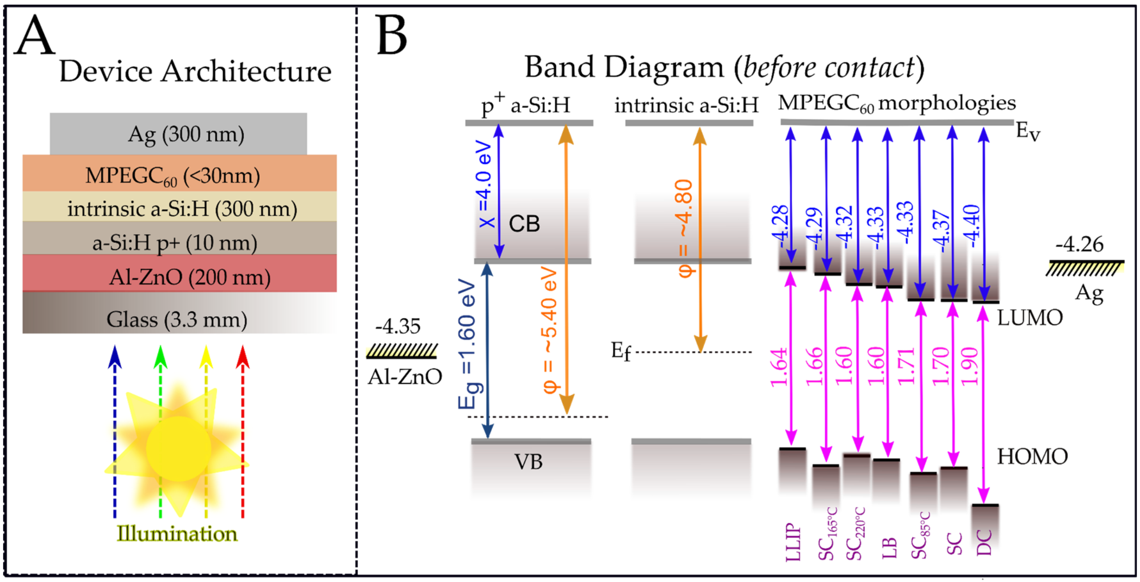

Figure 5—5: (A) Device architecture of the fabricated a-Si:H/MPEGC$_{60}$ HSCs, and (B) band diagram, before contact, shows energy levels of all components in the device. The HOMO, LUMO energies of MPEGC$_{60}$ morphologies are added from electrochemical data. (E_g: fundamental band gap, E_F: Fermi energy, E_v: vacuum energy, φ: work function, X: electron affinity, CB: conduction band, VB: valence band). The VB and CB energies of intrinsic a-Si:H are taken to be 5.6 eV and 4.0 eV and upon p-doping E_F shifts by ~600 meV towards the VB. All band energies are scaled to vacuum.

The typical S-shaped IV-profile of the standard p-i a-Si:H solar cell (donor only device) without n+-Si layer (grey IV-curve in Figure 5—6) is representative of the influence of pin-holes. Here pin-holes indicate cracks/breaks in the thin fullerene layer which exposes the a-Si:H to AZO cathode. Omission of the n+-doped silicon layer leads to a quasi-Fermi-energy mismatch ($\varepsilon_{F,c}$) in the a-Si:H intrinsic layer and the φ of Ag demonstrating a strong counter diode like behaviour with sufficiently low V_{OC} of 500 mV, and S-shaped IV-curve. The V_{OC} of these hole-only devices significantly increase by nearly 200 mV (LLIP cells gives V_{OC}≈700 mV), and the S-shape is reduced for the fullerene solar cells. Particularly, this effect is aggravated upon annealing which is a signature of reduced interface defect densities in the space charge region.[183]

Table 2: Photovoltaic characteristics of AZO/a-Si:H p^+/a-Si:H i/n^+-layer/Ag HSCs. J_{SC}: short-circuit current density, *FF*: fill factor, η: power conversion efficiency, V_{OC}: open circuit voltage; Ordering is according decreasing LUMO energies.

n^+-doped layer	V_{OC}^{max} (mV)	$\overline{V_{OC}}$ (mV)	*FF* (%)	J_{SC} (mA/cm²)	η(%)
$LLIP_{sh,wi\,\mid\,dist}$	696	683	45.7	9.3	2.86
$SC^{165°C}_{gr\,\mid\,csp}$	694	673	37.8	7.0	1.84
$SC^{220°C}_{gr\,\mid\,csp}$	680	667	37.3	6.8	1.72
$LB_{sh\,\mid\,csp}$	650	634	31.3	7.2	1.47
$SC^{85°C}_{gr\,\mid\,csp}$	643	627	44.9	6.2	1.80
$SC_{gr\,\mid\,csp}$	624	615	44.5	5.2	1.83
a-Si:H reference solar cells					
None	500	480	44.6	6.3	1.40
a-Si:H n^+	914	875	53.5	9.9	4.82
air exposure, a-Si:H n^+	865	860	50.6	7.7	3.36
None	500	480	44.6	6.3	1.40

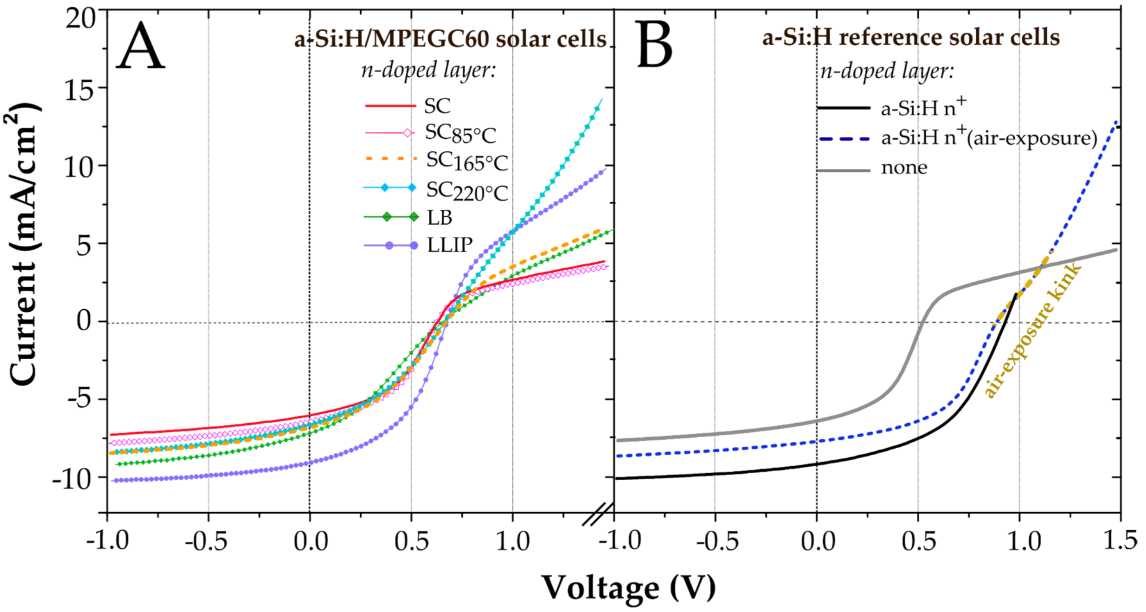

Figure 5—6: Current (*I*)-voltage (*V*) curves of the fabricated solar cells. (A) a-Si:H/MPEGC$_{60}$ HSCs; (B) reference inorganic a-Si:H solar cells.

5.4.2 *Morphology vs. Photovoltaic parameters*

The main focus of this section, is to correlate the morphology quantified by ξ, established in section 4.3.2, to the photovoltaic parameters of the fabricated a-Si:H/MPEGC$_{60}$-hybrid solar cells. The primary focus will be on V_{OC} changes which is linearly dependent on the LUMO energies of fullerenes, in turn dictated by morphological term factor (ξ). Next, the influence, of morphology, particularly supramolecular order, and packing on J_{SC} is discussed.

5.4.2.1 Influence on Open Circuit Voltage (V_{OC})

One needs to appreciate that V_{OC}, is simply $\Delta\varepsilon_F^{contact}$, *i.e.* Fermi energy difference between p$^+$ and n$^+$, when carrier generation is in equilibrium to recombination in contact, which is in turn proportional to the built-in potential of the cell V_{bi}, or $\Delta\varepsilon_F^{non-contact}$.[135] Therefore, $eV_{OC} = \varepsilon_F(n) - \varepsilon_F(p)$

or, $eV_{OC} \propto E_{LUMO}^{MPEGC_{60}} - \varepsilon_F(p)(a\text{-}Si{:}H)$ (because, all fullerene morphologies comes from the same MPEGC$_{60}$-batch and ε_F(n) depends on the doping level, and is material-specific).Since, ε_F(p)(a-Si:H) is constant for all hybrid solar cell:

$$eV_{OC} \propto E_{LUMO}^{MPEGC_{60}} \qquad (1)$$

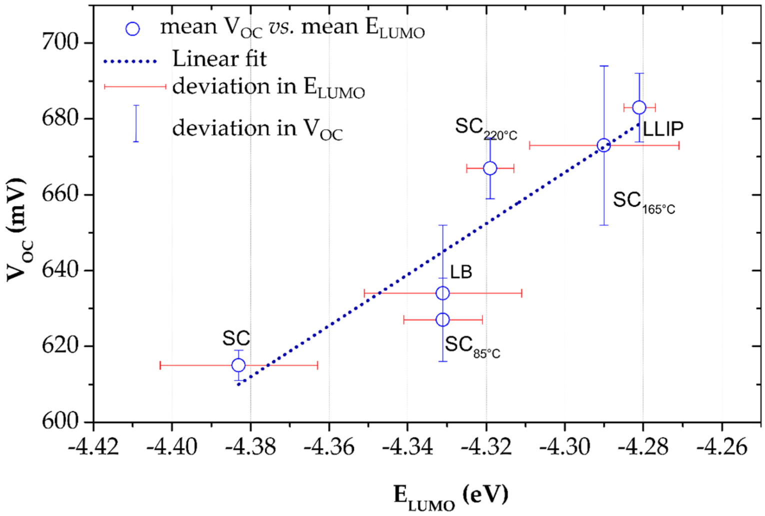

Figure 5—7: V_{OC} of the a-Si:H/MPEGC$_{60}$ HSCs *vs.* the LUMO energies obtained from electrochemical measurements.

In accordance to the above equation and the LUMO-energy values, *cf.* Figure 5—5, the following V_{OC}-trend for MPEGC$_{60}$ HSCs: $V_{OC}^{LLIP} > V_{OC}^{SC^{165^\circ C}} > V_{OC}^{SC^{220^\circ C}} > V_{OC}^{LB} > V_{OC}^{SC^{85^\circ C}} > V_{OC}^{SC}$ is expected. Figure 5—7 demonstrates that this order is roughly fits with an approximately linear relation (slope = 0.7 if V_{OC} is multiplied with the elemental charge *e*) between V_{OC}

and E_{LUMO} in comparison to the theoretically expected slope of unity for $e \cdot \Delta V_{OC}(V)/\Delta E_{LUMO}(eV)$.[179] Deviations from the perfect correlation can be an effect of reduction of trap states[184] at the a-Si:H-MPEGC$_{60}$ interface upon annealing. This might increase the parallel resistance and thus V_{OC}. Thermal treatment also reduces the S-shape (at I=0) of the IV curves, which indicates a reduction of interface defect densities in the space charge region.[183] The observed trend in mean V_{OC} demonstrates a net change of ~72 mV corresponding to the observed 120 mV change of supramolecular E_{LUMO}.

5.4.2.2 Influence on Short Circuit Current (J$_{SC}$)

J_{SC} is particularly influenced by: a) photon absorption in the absorber layer, and b) recombination *via* supramolecular disorder-caused tail states[185-187]. It is noted that photon absorption does not vary between the different cells made from the same a-Si:H batch, because the absorption coefficient of a-Si is comparable to fullerenes (~10^4-10^5 cm^{-1}), but the thickness of the MPEGC$_{60}$ films is ~20-30 times less in comparison to that of a-Si:H. Thus, varying optical characteristics of MPEGC$_{60}$ morphologies, *cf.* Chapter 4, section 3.2.1, does not influence either J_{SC} or efficiency.

Higher J_{SC}-values is realized for the interface-assembled supramolecular structures in $LB_{sh\,|\,csp}$ and $LLIP_{sh,wi\,|\,dist}$. The varying J_{SC} can arise due to high supramolecular order, in these morphologies. The highest supramolecular ordering in $LLIP$-films, mainly in their 2D nanosheets *cf.* Chapter 4, Figure 4—5 contributes to the highest J_{SC} value of 9.3 mA/cm^2 among the series. LB-sheets in the same way *cf.* Chapter 4, Figure 4—5, demonstrates high local ordering, but less global ordering comes second with J_{SC} value of 7.2 mA/cm^2. Presumably, because packing, *i.e.* inter-fullerene contacts and therefore electron-hopping, annealing improves J_{SC}-values of $SC_{gr\,|\,csp}$-HSCs, as summarized in Table 2. Thus, annealing $SC_{gr\,|\,csp}$ films at 85°C rises J_{SC} from 5.2 mA/cm^2 to 6.2 mA/cm^2, which is ascribed mainly because of improved surface coverage and the release of trapped spin-casting solvent. At 165°C, even higher J_{SC} values is witnessed (7 mA/cm^2) due to greater inter-fullerene contacts, but diminishes upon annealing at 220°C does not lead to a further increased J_{SC} probably due to receding acceptor layer and isolated cluster formation, *cf.* Chapter 4, Figure 4—2 exposing intrinsic a-Si:H layer to the Ag-contact.

5.5 Summary- Electronic Properties and Hybrid Solar Cells

In this chapter supramolecular fullerene assemblies discussed in Chapter 4 were fabricated on electrode surfaces, to study their electronic properties and subsequently as n-layer in amorphous Si solar cells. These supramolecular structures feature varying LUMO and HOMO energies, as revealed by square wave voltammetry measurements. While large inter-fullerene separation with large surface state availability were found to push LUMO energies towards vacuum, increasing aggregate size for the non-annealed films were found to stabilize HOMO-energies by hundreds of meVs. Overall, fabrication of the different supramolecular structures and morphologies enabled a total variation in the thin-film's LUMO energies of 120 meV. The LUMO energy variation could be explained by taking into consideration different fullerene/fullerene intermolecular distances between them and the number of nearest neighbors in accordance to their packing geometries.

Considering neighbor interactions based on fullerene in a molecular aggregate, morphological parameter ξ was defined to be ratio between bulk and surface molecules of that aggregate $N^{bulk}/N^{surface}$. Subsequently, an analytical expression was derived in this work considering, nearest neighbor interaction (ΔN_{nn}), ξ and E_{LUMO}^{bulk}energy. Simplifying the derived equation, the mean LUMO energy was found to be a function of ξ, thus implicitly controlled by actual aggregate morphology. Utilizing this equation it is predicted that $\Delta N_{nn} \Delta E_{LUMO}$ can vary by 0.20 eV upon fullerene supramolecular variation.

These tailored fullerene morphologies were finally incorporated as electron acceptor layers in solid state HSCs, to demonstrate the merit of supramolecular structure tuning. Particularly supramolecular order and observed LUMO energy variation of MPEGC$_{60}$ was shown to influence the J_{SC} and V_{OC} values of the hybrid cells, respectively. The V_{OC} data of the a-Si reference devices without acceptor layer, could be boosted up to ~200 mV, by incorporating fullerenes, highest for the LLIP-MPEGC$_{60}$ morphology. Secondly, up to 72 mV linear variation in V_{OC} was achieved, basically reflecting that varying, $E_{LUMO}^{MPEGC_{60}}$ tailors the potential energy barrier across the space charge region. Thirdly, the J_{SC} value of the a-Si:H/ fullerene devices were attributed not to the differently absorbing fullerene films, but to different degrees of supramolecular order. Therefore, LLIP films with largest global order features the highest J_{SC} value of 9.3 mA/cm^2, LB fingerprint layers (7.2 mA/cm^2) coming second followed by the annealed films. Finally, champion devices with power conversion efficiencies of 2.94% are obtained setting records in for a-Si:fullerene solar cell technology.

6 Summary and Outlook

Though fullerenes have been revolutionizing photovoltaic technology over the last decades,[20, 188-190] they are being replaced by non-fullerene acceptors.[28, 191] Albeit many upsides of fullerenes ranging from multiple charge acceptance to isotropic charge mobility are commendable; downsides like low visible light absorption and poor tunability of electronic energy levels and high cost are limiting their usability. Some earlier research was targeted towards the synthesis of structurally elegant and functional fullerene assemblies bound by multiple noncovalent interactions.[48, 192] However, just a few research on van der Waals (vdW) dimers and photo-polymerized fullerenes unveiled presence of charge traps[149] and high electron affinities[67] which are detrimental for photovoltaic performance. This early research has initiated the development of a holistic framework to understand how supramolecular structure determines optoelectronic properties. This has been the prime scientific challenge in fullerene electronics in the recent years.[192]

This thesis not only addresses the above mentioned challenge and bridges the gap between single molecule and device level, but strives to reach the grand target of alleviating the fundamental limitations of fullerenes (also see Figure 1—1 and Figure 1—2). This is done by tailoring the optoelectronic properties of the amphiphilic fullerene derivative MPEGC$_{60}$, by supramolecular structural control on thin solid films. The major outcomes of the thesis has been schematically demonstrated in Figure 6—1and is discussed briefly below.

First, the *optical properties* of these fullerene morphologies were studied in detail by absorption spectroscopy and quantum chemical calculations (see panel B, Figure 6—1). Differences in fullerene orientation (*parallel* or *random*) within these thin-films heavily influenced the film's absorption spectra. Systematic dilution experiments in a stearic acid matrix, revealed a well-resolved UV-peak for fullerene dimers with maximum buckyball interactions (λ_{dimer} = 234 nm). This feature can be used as a fingerprint to identify fullerene dimers in a heterogeneous solution mixture. Further differences in optical spectra was witnessed for fullerene clusters with characteristic structure properties: intermolecular distance, geometry, symmetry and size. TD-DFT simulations enumerates these differences and molecular orbital analysis was used to reveal their origins in the light of electronic structure theory.[19]

---

[19] Further conclusions on optical properties can be found as summary at the end of Chapter 3.

Next, the *morphological properties* of fullerene thin-films was studied in details (see panel C, Figure 6—1). These films were produced using self-assembly at liquid/liquid interfaces (LLIP technique), air-water interfaces (LB technique), and on solid supports (Spin Coating (SC) and Drop Coating (DC) techniques) with or without thermal treatment. Fullerene's multiple vdW and π-π interactions, lead to the formation of unique non-covalent morphologies achieved by these preparation methods. In-depth grain analysis, revealed that the prepared fullerene assemblies scaled from a few nanometers (<10 nm) up to a few micrometers (see panel C, Figure 6—1). DC and SC amorphous films featured vesicular and ellipsoidal aggregates. Thermal annealing produced crystalline grains which grew in size to spheroid aggregates at higher temperatures. LB films exhibited densely packed fingerprint like assemblies with locally ordered fullerenes in the nm scale, but less global ordering in the μm-scale. 2D extended nanosheets and nanowires were synthesized by LLIP technique upon extended sonication. In contrast to LB films, they demonstrated more global order and significantly larger lattice constants. UV-vis measurements on thin-films consisting each morphology shed light on their supramolecular structures, revealing that inter-fullerene distances and supramolecular order largely depends on annealing temperature and deposition interfaces.[3]

The *electronic properties* of these fullerene morphologies were studied next; through electrochemical measurements on modified electrode surfaces and quantum chemical calculations (see panel B, Figure 6—1). The actual supramolecular structure of these morphologies control their LUMO energies which could be tailored by tens up to 120 meV. Comparing grain analysis data to LUMO energies and DFT calculation on large fullerene clusters (from mono- to tetramers), an important analytical expression was deduced (see panel C, Figure 6—1). This expression suggests that the LUMO energy of *any* fullerene aggregate can be deduced if ξ (the molecular number ratio between bulk and surface states of that aggregate), bulk LUMO energy of the fullerene derivative and the supramolecular dimensions of that aggregate is known.[20]

---

[20] Further conclusions on morphological and electronic properties can be found as Chapter summary 3 and 4, respectively.

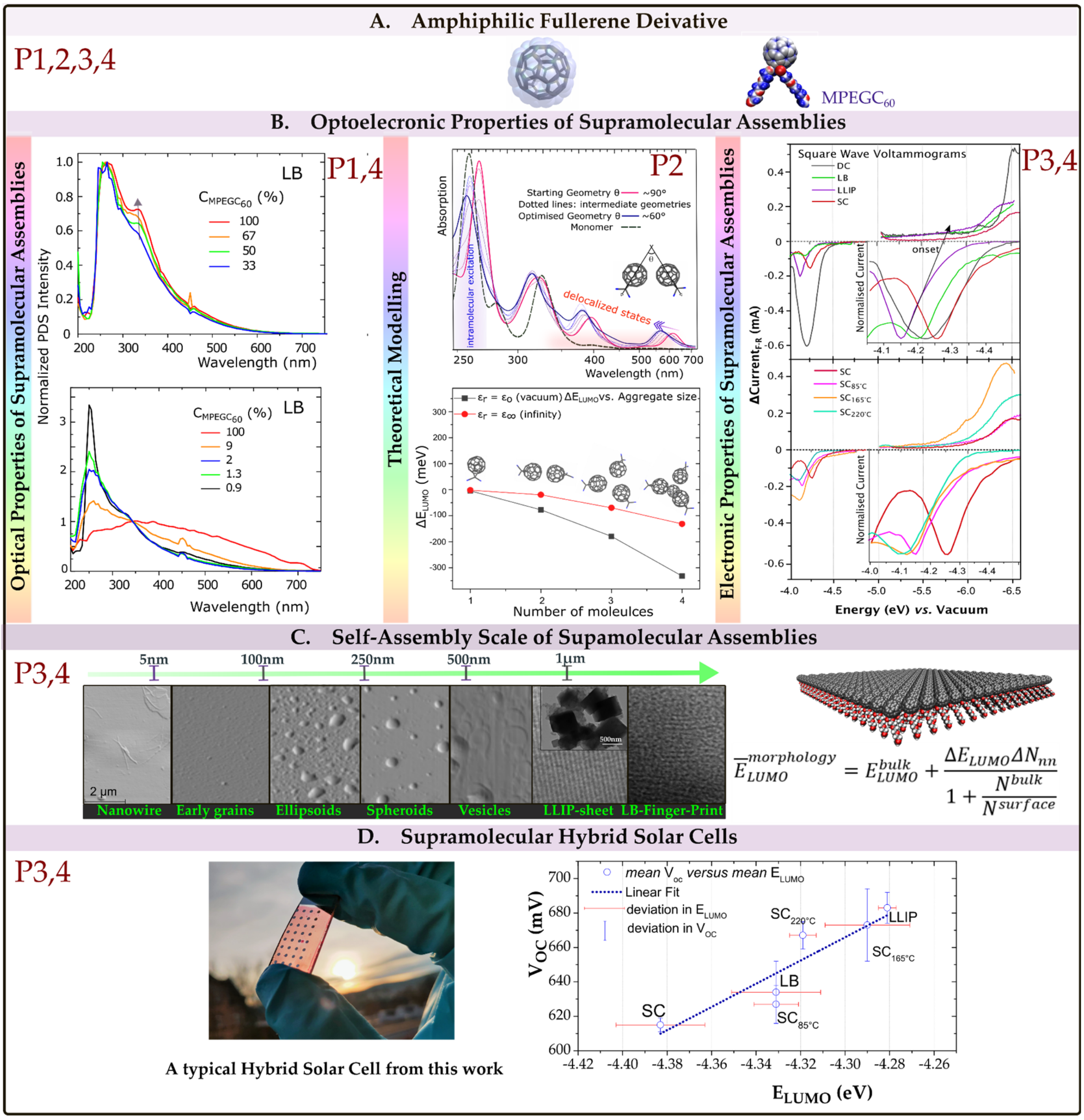

$$E_{LUMO}^{morphology} = E_{LUMO}^{bulk} + \frac{\Delta E_{LUMO} \Delta N_{nn}}{1 + \frac{N^{bulk}}{N^{surface}}}$$

Figure 6—1: Schematic representation of the essential results of this thesis as solution to the scientific questions: *cf*. Figure 1—1, with corresponding publications (P1, P2, P3 and P4). Panel A shows MPEGC$_{60}$ who's optical (P1, P2) and electronic properties (P2) was tailored, supported by theoretical modelling (P1, P2, P3) in Panel B. Panel C shows the self-assembly scale of MPEGC$_{60}$ assemblies extending from nm to µm length scales. The correlation between supramolecular structure and LUMO energy is displayed on the right. Panel D shows the architecture of a-Si:H/MPEGC$_{60}$ HSC whose V_{OC} is a linear function of MPEGC$_{60}$'s supramolecular LUMO energies.

Finally, the practical application of the above lessons on optoelectronic properties were ensured by fabricating solid state a-Si:H/MPEGC$_{60}$ solar cells (see panel D, Figure 6—1). Each morphology were utilized as organic acceptor layer while a-Si:H served as the inorganic donor layer in the hybrid solar cell. These bilayer devices showed a 200 mV increment in V_{OC}. Since the spacing between VB of a-Si:H and LUMO of MPEGC$_{60}$ was systematically enlarged due to supramolecular LUMO-energy variation a total ~72 mV linear increment in V_{OC} was observed. The LLIP solar cell featured the highest efficiency of 2.94%, setting a record in a-Si/fullerene photovoltaics.

Now, the scientific questions set for this thesis in the introductory chapter (section 1.2 and Figure 1—1) are evaluated in retrospect:

a) *Can the same fullerene derivative be assembled into different supramolecular structures? How far can self-assembly scale spatially, if prepared from the same derivative?*

The same amphiphilic MPEGC$_{60}$ was shown to organize into vesicular, grainy, ellipsoidal, spheroids, globally/locally ordered two-dimensional sheets, nanowire and flaky structures. These structures have different packing, supramolecular order and ranges from nanoscopic grainy structures to mesoscopic annealed aggregates and finally, spatially extended μm long sheets. The self-assembly ranges from a few nm to μm scales.

b) *How does optical and electronic properties change with morphology i.e. at different size scales of the assembly, and other structural parameters, like intermolecular distances and supramolecular order*?

The *optical properties* of fullerene morphologies are heavily dependent on size, only when the symmetry of the overall morphology is random. This is why highly concentrated SC films with stochastic and macroscopic aggregates, revealed pronounced and broad vis-absorption with poor UV absorption, while LB films constituting aggregates with fixed symmetry influenced the absorption spectra only negligibly. Reducing intermolecular distances, on the other hand, increases intermolecular π-π interactions, and boosts vis-absorption, only if the aggregate is non-centrosymmetric. *Centrosymmetric fullerene aggregates are always poorly vis-absorbing*- a corollary to Laporte's selection rule[162] was verified in this thesis.

The *electronic properties* of the produced fullerene morphologies, particularly LUMO-energies are found to be strongly dependent on supramolecular structure. Depending on their morphological parameter ξ and bulk LUMO energy, the effective LUMO energy of a fullerene assembly can be tuned, as per requirement. In effect, a total variation of 120 meV was observed for the same fullerene species.

c) *Can the morphology dependent optoelectronic properties be witnessed in a pure self-assembly based solar cell, in the form of certain photovoltaic parameter variation*?

Solar cells were fabricated with a-Si:H electron donor layer, and fullerenes with well-defined morphologies serving as electron acceptors. The merit of LUMO energy tuning is witnessed by linear variation of V_{OC}, while supramolecular order contributes to particularly high J_{SC}. Particularly, morphologies with LUMO energies closer to a-Si:H CB features high V_{OC}, for *e.g.* LLIP morphology has the highest LUMO energy (-4.28 eV), thereby featuring the highest V_{OC} (696 mV) of the series.

Finally, how far addressing the above open questions (a-c) can alleviate the drawbacks of fullerenes as outlined in section 1.2, more specifically, low vis-absorption with poor tunability of optical transitions, high electron-affinities with poor tunability of electronic states and high-cost for large scale use?

The traditional method of tailoring optoelectronic properties of fullerene is through molecular variation, *i.e.* linking electron acceptor/donating groups. Such a method can yield molecules with improved absorption or tuned LUMO energies, but physicochemical properties like solubility, stability or synthetic costs are limiting this approach. The interfacial self-assembly approach developed in this thesis stands as an alternative to achieve desired optoelectronic properties of fullerenes without influencing its physicochemical properties.

- It is demonstrated, that supramolecular structure can heavily influence fullerene's UV-vis light absorption in thin-films and can lead to high vis-absorption and tailored optical transitions alleviating the first drawback (low vis-absorption).
- Electron affinity (LUMO energy) of the same amphiphilic fullerene was tuned up to 120 meV in thin-films alleviating the second drawback (poor tunability of electronic energy levels).
- Lastly, the hybrid solar devices fabricated in this thesis are comprised of thin fullerene layers (10-20 nm). For the fabrication of these devices, stock solutions with 100x less fullerene concentration ($C_{MPEGC60}$ = 0.1-0.5 mg/ml), than traditional fullerene photovoltaics ($C_{fullerenes}$ = 20-30 mg/ml) was used. In spite of such low material usage reasonable J_{SC} value of 9.3 mA/cm^2, V_{OC} value of 696 mV and a handsome ~2.94% P.C.E for the champion devices was reported. Thus, the final drawback of fullerenes (costing) was alleviated, for pocket-friendly, large scale industrial processing.

Outlook

Research in self-assembled fullerene photovoltaics outside the scope of this thesis is currently being explored within two broad directions[21]: a) to test the prospects of the developed fullerene nanostructures developed in this work in perovskite solar cells[193-194] and b) to test functional photovoltaics fabricated with MPEGC_{60} with increasing hydrophilicity.[195] Here, the highlights of research direction a) is highlighted briefly.

Perovskites traditionally belong to an inorganic crystal class with ABX_3 structure, and are usually employed as organic/inorganic hybrid materials for high efficiency solar cells[196]. Usually these photoactive perovskite layers are sandwiched between hole and electron transport layers (HTL and ETL) to extract charges into external circuit.[22, 197] Self-assembled fullerenes as perovskite ETL layers have been successfully used as a thin interlayer (~10 nm) between TiO_2 and perovskite active layer to improve charge extraction, and reduce hysteresis.[197] Fullerenes have been shown to passivate defects in perovskite active layers and improve the overall cell V_{OC}.[22]

Among all synthesized fullerene supramolecular assemblies in this thesis, LLIP fullerenes stood out due to their high supramolecular order and tailored LUMO energies. $PC_{71}BM$ LLIP structures were synthesized and doped within mesoporous TiO_2 for planar $MAPbI_3$/fullerene perovskite devices. This doping of $PC_{71}BM$ LLIP structure into mesoporous TiO_2 to form a single heterojunction ($PC_{71}BM$ LLIP-TiO_2) has two advantages over their bilayer architecture ($PC_{71}BM$ LLIP | TiO_2): a) more $PC_{71}BM/TiO_2$ interfaces in heterojunction architecture leads to greater electron percolation pathways to the FTO anode, b) easier and time-effective fabrication process. The resulting fabricated device architecture can be represented as:

FTO *(anode)* | $PC_{71}BM$ LLIP-TiO_2 *(ETL)* | $MAPbI_3$ *(active-layer)* | spiroMeOTAD *(HTL)* | Au *(cathode)*

In this representation, the function of each component of the device is provided within parentheses and each interface is represented by the | symbol. Detailed description of the constituting materials and overall device fabrication process is reported by Saliba *et al.*[198] Without going into intricate details this Outlook section and Figure 6—2 share initial results to demonstrate how doping $PC_{71}BM$ LLIP structures in TiO_2 boost $MAPbI_3$ device performance.

---

[21] This first part (a) was done as a part of visiting research project at Adolphe Merkle Institute of the University of Fribourg, Switzerland in the research laboratory of Professor Ulrich Steiner and Dr. Michael Saliba. The second part (b) of the work is currently ongoing in FSU Jena.

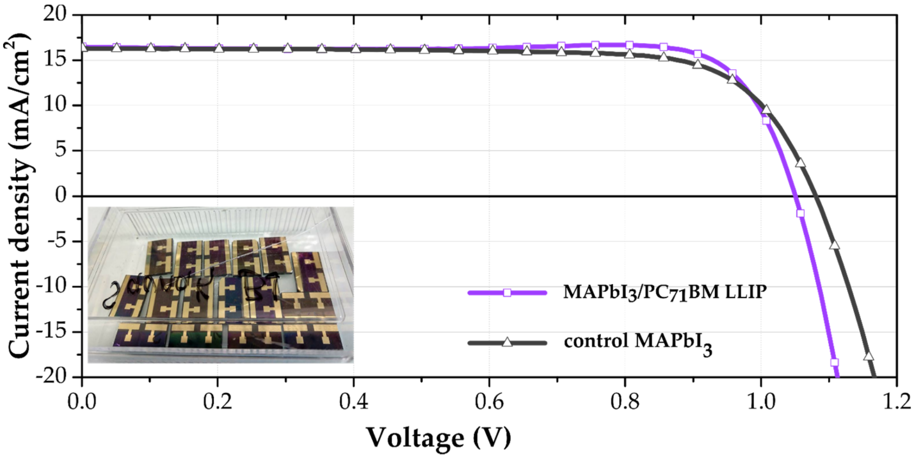

Figure 6—2: Exemplary I-V profiles of control $MAPbI_3$ and hybrid $MAPbI_3/PC_{71}BM$ LLIP solar cells.

These fabricated devices comprised of an average V_{OC} of 1034 mV, a P.C.E. of 16.3%, FF 70% and J_{SC} of 14.7 mA/cm^2, relatively better than the control devices. Though this research is in its infancy, these initial results demonstrate that self-assembled fullerene structures can be promising in the field of perovskite solar cells.

7 Zusammenfassung und Ausblick

Obwohl Fullerene die Photovoltaik-Technologie in den letzten Jahrzehnten revolutioniert haben,[20, 188-190] werden sie durch Nicht-Fulleren-Akzeptoren ersetzt.[28, 191] Trotz ihrer vielen Vorteile, die von der Mehrfachladung bis zur isotropen Ladungsmobilität reichen, wird deren Verwendbarkeit durch eine geringe Absorption von sichtbarem Licht, eine schlechte Abstimmbarkeit der elektronischen Energieniveaus und hohen Kosten eingeschränkt. Einige frühere Forschungen zielten auf die Synthese von strukturell eleganten und funktionellen Fullerenanordnungen ab, welche durch mehrere nicht-kovalente Wechselwirkungen erreicht werden.[48, 192] Allerdings enthüllten einige Studien zu van der Waals (vdW) Dimeren und photopolymerisierten Fullerenen das Vorhandensein von Ladungsfallen[149] und einer hohen Elektronenaffinität,[67] die wiederum einer hohen photovoltaische Leistung abträglich sind. Jene frühe Forschung hat die Entwicklung eines ganzheitlichen Ansatzes angestoßen, mit dem verstanden werden kann wie die supramolekulare Struktur optoelektronische Eigenschaften bestimmt. Dies bildete in den letzten Jahren die primäre wissenschaftliche Herausforderung in der Fullerenelektronik.[192]

Die hier vorgestellte Arbeit befasst sich nicht nur mit der oben genannten Herausforderung, sondern schließt die Lücke zwischen Einzelmolekül und Geräteebene und strebt darüber hinaus das große Ziel an, die grundlegenden Grenzen der Fullerene zu verringern (siehe auch Abbildung 1-1 und Abbildung 1-2). Dies geschieht durch die Anpassung der optoelektronischen Eigenschaften des amphiphilen Fullerenderivates MPEGC$_{60}$ durch supramolekulare Strukturkontrolle auf dünnen Festschichten. Die wichtigsten Ergebnisse der Arbeit wurden schematisch in Abbildung 6-1 dargestellt und werden im Folgenden kurz erläutert.

Zunächst wurden die optischen Eigenschaften dieser Fullerenmorphologien durch Absorptionsspektroskopie und quantenchemische Berechnungen detailliert untersucht (siehe Panel B, Abbildung 6-1). Unterschiede in der Fullerenorientierung (*parallel* oder *ungeordnet*) innerhalb dieser dünnen Schichten beeinflussten die Absorptionsspektren der Schicht stark. Systematische Verdünnungsexperimente in einer Stearinsäurematrix ergaben einen gut aufgelösten UV-Peak für Fullerendimere mit maximaler Interaktion zwischen den beiden Fulleren (λ_{dimer} = 234 nm). Dieses Merkmal kann als spektraler Fingerabdruck verwendet werden um Fullerendimere in einem heterogenen Lösungsgemisch zu identifizieren. Weitere Unterschiede in den optischen Spektren wurden für Fullerencluster mit charakteristischen strukturellen Eigenschaften, wie intermolekularer Abstand, Geometrie, Symmetrie und Größe beobachtet. Die TD-DFT-Simulationen zeigen diese Unterschiede in Betrachtung der elektronischen Strukturtheorie [22]

Anschließend wurden die morphologischen Eigenschaften von Fullerendünnschichten im Detail untersucht (siehe Panel C, Abbildung 6-1). Diese Schichten wurden durch Selbstassemblierung an Flüssig-Flüssig-Grenzflächen (LLIP-Technik), Luft-Wasser-Grenzflächen (LB-Technik) und auf festen Trägern (SC- und DC-Technik) mit oder ohne Wärmebehandlung hergestellt. Eine Fülle an Möglichen vdW und π-π Interaktionen zwischen Fullerenen führen zur Bildung einzigartiger nicht-kovalenter Morphologien, welche durch diese Präparationsmethoden erreicht werden können. Eine eingehende Körnungsanalyse ergab, dass die präparierten Fullerenanordnungen von wenigen Nanometern (<10 nm) bis hin zu einigen Mikrometern skalieren (siehe Panel C, Abbildung 6-1). DC- und SC-amorphe Schichten zeigten vesikuläre und ellipsoide Aggregate. Beim Tempern entstanden kristalline Körner, die bei höheren Temperaturen sphäroidische Aggregate formten. Die LB-Filme zeigten dicht gepackte, fingerabdruckartige Anordnungen mit lokal geordneten Fullerenen im Nanometerbereich, aber auch eine geringere globale Ordnung im Mikrometerbereich. Zweidimensional ausgedehnte Nanoblätter und Nanodrähte wurden mittels LLIP-Technik durch längere Ultraschallbehandlung synthetisiert. Im Gegensatz zu LB-Filmen zeigten diese eine höhere globale Ordnung und deutlich größere Gitterkonstanten. UV-vis-Messungen an dünnen Schichten, welche jeweils aus einer Morphologie bestehen, klären deren supramolekulare Strukturen auf und zeigen, dass die Inter-Fulleren-Abstände hauptsächlich von der Tempertemperatur und der Abscheidungsgrenzfläche abhängig sind.[23]

Als nächstes wurden die elektronischen Eigenschaften dieser Fullerenmorphologien durch elektrochemische Messungen an modifizierten Elektrodenoberflächen und durch quantenchemische Berechnungen untersucht (siehe Panel B, Abbildung 6-1). Die supramolekulare Struktur der jeweiligen Morphologie bestimmt ihre LUMO-Energie, die wiederum um Dutzende bis zu 120 meV angepasst werden konnte. Aus dem Vergleich der Körnungsanalysedaten mit LUMO-Energien und DFT Berechnungen an

---

[22] Weitere Schlussfolgerungen zu den optischen Eigenschaften befinden sich als Zusammenfassung am Ende von Kapitel 3.

[23] : Weitere Schlussfolgerungen zu morphologischen und elektronischen Eigenschaften befinden sich in den Kapiteln 3 und 4.

großen Fullerenclustern (von Mono- bis Tetrameren) wurde ein wichtiger analytischer Ausdruck abgeleitet (siehe Panel C, Abbildung 6-1). Dieser Ausdruck deutet darauf hin, dass die LUMO-Energie eines beliebigen Fullerenaggregats abgeleitet werden kann, wenn ξ (das Molekularzahlenverhältnis zwischen Bulk- und Oberflächenzuständen dieses Aggregats), die LUMO-Energie des Bulks und die supramolekularen Dimensionen dieses Aggregats bekannt sind.[24]

Schließlich wurde die praktische Anwendbarkeit der oben genannten Erkenntnisse über optoelektronische Eigenschaften von Fullerenen durch die Herstellung einer a-Si:H/MPEGC_{60} Festkörpersolarzellen sichergestellt (siehe Panel D, Abbildung 6-1). Dabei wurden die verschiedenen Morphologien als organische Akzeptorschicht getestet, während a-Si:H als anorganische Donorschicht diente. Diese Hybrid-Solarzellen zeigten einen Anstieg der V_{OC} um 200 mV. Zusätzlich wurde ein lineares Inkrement von ~72 mV in V_{OC} beobachtet, da der energetische Abstand zwischen dem VB von a-Si:H und dem LUMO von MPEGC_{60} durch die supramolekulare LUMO-Energievariation systematisch vergrößert wurde. Die LLIP-Solarzelle wies mit 2,94 % den höchsten Wirkungsgrad auf und stellte damit einen Rekord in der a-Si/Fulleren-Photovoltaik auf.

Abschließend werden die wissenschaftlichen Fragen, die für diese Arbeit im einleitenden Kapitel (Abschnitt 1.2 und Abbildung 1-1) gestellt wurden, im Rückblick betrachtet:

a) Kann das gleiche Fullerenderivat in verschiedenen supramolekularen Strukturen angeordnet werden? Wie groß skalieren die selbstassemblierten Fullerenstrukturen räumlich, wenn dieses aus dem gleichen Derivat hergestellt wird?

Es wurde gezeigt, dass sich das amphiphiles MPEGC_{60} Molekül in vesikuläre, körnige, ellipsoide, sphäroidische, globale/lokal geordnete zweidimensionale Schichten, Nanodrähte und schuppige Strukturen organisiert. Diese Strukturen haben eine unterschiedliche Packung, supramolekulare Ordnung und reichen von nanoskopischen, körnigen Strukturen über mesoskopische Aggregate bis hin zu räumlich ausgedehnten Mikrometer langen Schichten. Die selbstassemblierten Fullerenstrukturen erstreckt sich im Bereich von wenigen Nanometern bis hin zu Mikrometer.

---

[24] Weitere Schlussfolgerungen zu morphologischen und elektronischen Eigenschaften befinden sich in den Kapiteln 3 und 4.

b) Wie ändern sich optische und elektronische Eigenschaften mit der Morphologie, d.h. bei unterschiedlichen Größenskalen der selbstassemblierten Fullerenstrukturen und anderen struktureller Parametern, wie intermolekulare Abstände und supramolekulare Ordnung?

Die *optischen Eigenschaften* von Fullerenmorphologien hängen stark von der Größe ab, falls die Symmetrie der Gesamtmorphologie ungeordnet ist. Aus diesem Grund zeigten hochkonzentrierte SC-Schichten mit ungeordneten und makroskopischen Aggregaten eine ausgeprägte und breite Vis-Absorption mit schlechter UV-Absorption, während LB-Schichten, die Aggregate mit fester Symmetrie bilden, die Absorptionsspektren nur geringfügig beeinflussten. Die Verringerung der intermolekularen Abstände hingegen erhöht die intermolekularen π-π Interaktionen und steigert die Vis-Absorption, falls das Aggregat nicht zentralsymmetrisch ist. *Zentralsymmetrische Fullerenaggregate absorbieren immer schlecht im sichtbaren*. Dies ist eine Konsequenz aus Laporte's Auswahlregel,[162] die in dieser Arbeit verifiziert wurde.

Die *elektronischen Eigenschaften* der erzeugten Fullerenmorphologien, insbesondere der LUMO-Energien, sind stark von der supramolekularen Struktur abhängig. Abhängig von ihrem morphologischen Parameter ξ und der LUMO-Energie des Bulks kann die effektive LUMO-Energie einer Fullerenanordnung je nach Bedarf eingestellt werden. In der Tat wurde eine Gesamtvariation von 120 meV für die gleiche Fullerenart beobachtet.

c) Bewirken die morphologieabhängigen optoelektronischen Eigenschaften in einer auf Selbstassemblierung basierenden Solarzelle eine bestimmte photovoltaische Parametervariation?

Solarzellen wurden mit einer a-Si:H Elektronendonorschicht hergestellt, wobei Fullerene mit klar definierten Morphologien als Elektronenakzeptoren dienten. Der Vorteil der LUMO-Energieabstimmung zeigte sich in der linearen Variation des V_{OC}, während die supramolekulare Ordnung zu einem besonders hohen J_{SC} beiträgt. Insbesondere Morphologien mit LUMO-Energien die näher an dem CB von a-Si:H liegen, weisen einen hohen V_{OC}-Wert auf. Zum Beispiel hat die LLIP-Morphologie die höchste LUMO-Energie (-4,28 eV) und damit auch den höchsten V_{OC}-Wert (696 mV) der Serie.

Schließlich, inwieweit kann die Beantwortung der oben genannten Fragen (a-c) die in Abschnitt 1.2 beschrieben Nachteile von Fullerenen mildern? Diese Nachteile sind insbesondere die geringe Vis-Absorption mit der schlechten Abstimmbarkeit von optischen Übergängen, die hohen Elektronenaffinitäten mit der schlechten Abstimmbarkeit von elektronischen Zuständen, und die hohen Kosten, die bei einem großtechnischen Einsatz entstehen würden.

Die traditionelle Methode zur Anpassung der optoelektronischen Eigenschaften von Fulleren erfolgt durch molekulare Variation, d.h. durch die Verknüpfung von Elektronenakzeptor- und Elektronendonorgruppen. Ein solches Vorgehen kann Moleküle mit verbesserter Absorptionseigenschaften und abgestimmten LUMO-Energien hervorbringen. Allerdings begrenzen physikalisch-chemische Eigenschaften wie Löslichkeit, Stabilität oder Synthesekosten diesen Ansatz. Die in dieser Arbeit weiterentwickelte Technik der Selbstassemblierung an Grenzflächen stellt eine Alternative dar, um die gewünschten optoelektronischen Eigenschaften von Fullerenen zu erzielen, ohne jedoch ihre physikalisch-chemischen Eigenschaften zu beeinflussen.

- Es wurde gezeigt, dass die supramolekulare Struktur die UV-vis-Lichtabsorption des Fullerens in dünnen Schichten stark beeinflussen kann und zu hoher Vis-Absorption und maßgeschneiderten optischen Übergängen führen kann. Dies kann den ersten Nachteil der geringen Vis-Absorption lindern.
- Die Elektronenaffinität (LUMO-Energie) desselben amphiphilen Fullerens wurde bis zu 120 meV in dünnen Schichten abgestimmt, was den zweiten Nachteil, die schlechte Abstimmbarkeit der elektronischen Energieniveaus, lindert.
- Schließlich wurden in dieser Arbeit hybride Solarzellen hergestellt, die aus dünnen Fullerenschichten (10-20 nm) bestehen. Für deren Herstellung waren 100-fach geringere Konzentration an Fulleren ($c_{CMPEGC60}$ = 0,1 - 0,5 mg/ml) als bei der Herstellung herkömmliche Fulleren-Photovoltaik ($c_{Fullere}$ = 20-30 mg/ml) notwendig. Trotz des geringen Materialverbrauchs wurde ein vernünftiger J_{SC}-Wert von 9,3 mA/cm^2, ein V_{OC}-Wert von 696 mV und eine hervorragende ~2,94 %ige P.C.E. für die Vorzeigegeräte erreicht. So wurde der endgültige Nachteil von Fullerenen (Kosten) für eine portemonnaieschonende, großindustrielle Verarbeitung gemildert.

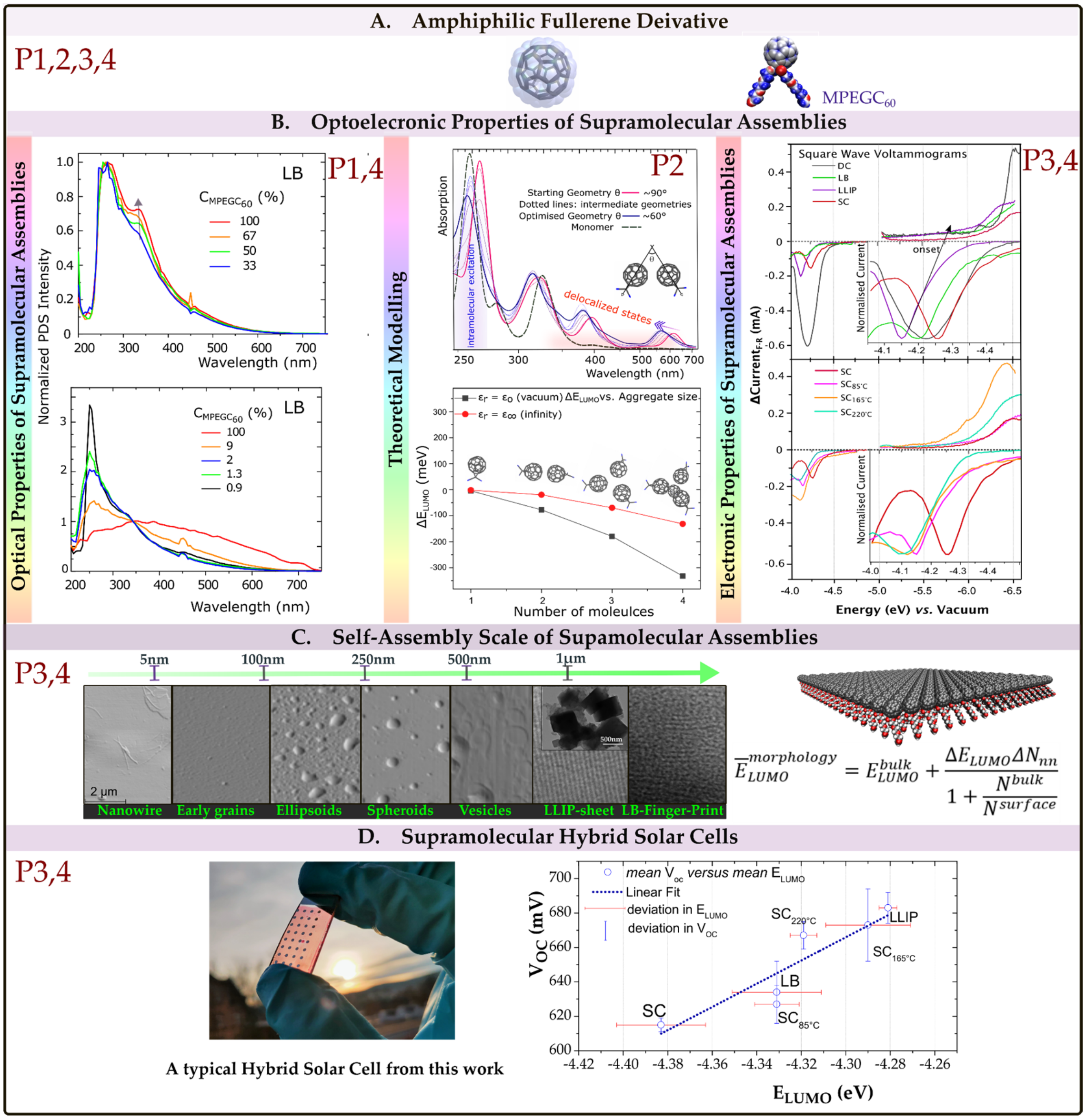

Abbildung 7—1: Schematische Darstellung der wesentlichen Ergebnisse dieser Arbeit als Antwort auf die wissenschaftlichen Fragen: vgl. Abbildung 1-1 mit entsprechenden eingebundenen Publikationen (P1, P2, P3 und P4). Panel A zeigt MPEGC$_{60}$, dessen optischen (P1, P2) und elektronischen Eigenschaften (P2) maßgeschneidert wurden, unterstützt durch theoretische Modellierung (P1, P2, P3) in Panel B. Panel C zeigt die selbstassemblierten Strukturen von MPEGC$_{60}$-Baugruppen, die sich von Nanometer bis Mikrometer Länge erstrecken. Der Zusammenhang zwischen supramolekularer Struktur und LUMO-Energie ist hierbei rechts dargestellt. Panel D zeigt die Architektur von a-Si:H/MPEGC$_{60}$ Hybrid-Solarzelle, dessen V_{OC} eine lineare Funktion der supramolekularen LUMO-Energien von MPEGC$_{60}$ ist.

Ausblick

Die Forschung zu der selbstassemblierten Fullerenphotovoltaik wird derzeit über diese Arbeit hinaus in zwei großen Richtungen untersucht:[25] a) die Perspektiven der in dieser Arbeit entwickelten Fullerennanostrukturen werden in Perowskitsolarzellen[193-194] getestet und b) die mit $MPEGC_{60}$ hergestellten funktionalen Solarzelle werden mit einer zunehmender Anzahl von PEG-Ketten, d.h. einer erhöhter Hydrophilie, getesten.[195] Hier werden die Highlights der Forschungsrichtung a) kurz hervorgehoben.

Perowskite gehören traditionell zu einer anorganischen Kristallklasse mit ABX3-Struktur und werden üblicherweise als organisch-anorganische Hybridmaterialien für hocheffiziente Solarzellen1 eingesetzt.[196] Normalerweise werden diese photoaktiven Perowskitschichten zwischen einer Loch- und Elektronentransportschichten (HTL und ETL) eingeschlossen um Ladungen in den externen Stromkreis zu extrahieren.[22, 197] Selbstassemblierte Fullerenstrukturen als Perowskit-ETL-Schichten wurden erfolgreich als dünne Zwischenschicht (~10 nm) zwischen TiO_2 und Perowskit-Aktivschicht eingesetzt, um die Ladungsextraktion zu verbessern und die Hysterese zu reduzieren.[197] Fullerene haben sich als passivierend für Defekte in Perowskit-Aktivschichten erwiesen und verbessern die gesamte V_{OC}.[22]

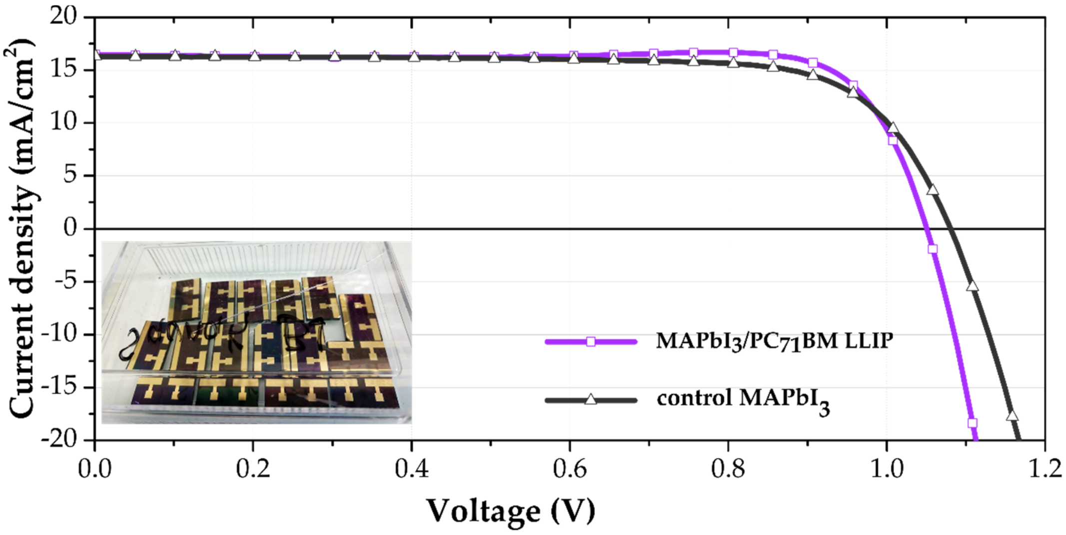

Abbildung 7—2: Exemplarische I-V-Profile von $MAPbI_3$ Referenz und hergestellten hybriden $MAPbI_3$/PC71BM LLIP-Solarzellen.

---

[25] Der erste Teil (a) wurde im Rahmen eines Gastforschungsprojektes am Adolphe Merkle Institut der Universität Fribourg, Schweiz, im Forschungslabor von Professor Ulrich Steiner und Dr. Michael Saliba durchgeführt. Der zweite Teil (b) der Arbeit wird derzeit in der FSU Jena weitergeführt.

Wie diese Arbeit zeigt, ist die Herstellung ultradünner Fullerenschichten mit hoher morphologischer Kontrolle für eine schnelle und effiziente Verarbeitung im Labormaßstab nicht einfach.

Dies führte zu der Idee, LLIP Fullerenstrukturen innerhalb von TiO_2 zu interkalieren, um ein einziges ETL anstelle einer separaten Zwischenschicht herzustellen. Unter allen synthetisierten supramolekularen Fullerenstrukturen, die in dieser Arbeit untersucht wurden, zeichneten sich LLIP Fullerene durch ihre hohe supramolekulare Ordnung und maßgeschneiderte LUMO-Energien aus. $PC_{71}BM$ LLIP-Strukturen wurden synthetisiert und in mesoporöses TiO_2 dotiert um $MAPbI_3$/Fulleren-Perowskit-Solarzellen zu erhalten. Ohne auf komplizierte Details über deren Herstellung und die physikalischen Grundlagen eingehen zu wollen, werden in diesem Abschnitt sowie in der Abbildung 6-2 erste Ergebnisse vorgestellt. Diese zeigen, wie die Dotierung von TiO_2 mit PC71BM LLIP Strukturen die Leistung von $MAPbI_3$ Zellen erhöht.

Unter den in dieser Arbeit synthetisierten, selbstassemblierten Fullerenstrukturen zeichneten sich die LLIP Fullerenstrukturen durch eine hohe supramolekulare Ordnung und eine maßgeschneiderte LUMO-Energien aus. Um planare $MAPbI_3$/Fulleren-Perowskit-Solarzellen herzustellen, wurden $PC_{71}BM$ LLIP Strukturen synthetisiert und in eine mesoporöses TiO_2 dotiert. Diese Dotierung erzeugt einen einzigen Heteroübergang ($PC_{71}BM$ LLIP-TiO2) und hat zwei Vorteile gegenüber einer traditionellen Doppelschichtarchitektur ($PC_{71}BM$ LLIP|TiO2): erstens, führt die größere Grenzfläche zwischen $PC_{71}BM$ und TiO_2 in der Heteroübergangsarchitektur zu einer größeren Zahl von Elektronenperkolationswegen zur FTO Anode, zweitens, ist die Herstellung eines einzelnen Heteroübergang einfacherer und zeitsparender als die Herstellung einer Doppelschichtarchitektur. Die resultierende Architektur der Solarzelle kann wie folgt dargestellt werden:

FTO *(anode)*|$PC_{71}BM$ LLIP-TiO_2 *(ETL)*| $MAPbI_3$ *(active-layer)*| spiroMeOTAD *(HTL)*|Au *(cathode)*

In dieser Darstellung ist die Funktion der jeweiligen Zellkomponente in Klammern angegeben und jede Schnittstelle wird durch das Symbol | repräsentiert. Eine detaillierte Beschreibung der konstituierenden Materialien und der Herstellungsprozess der Zellen wird von Saliba et al.[198] berichtet.

Die hergestellten Zellen erreichten durchschnittlich eine V_{OC} von 1034 mV, einer P.C.E. von 16,3 %, einen FF von 70 % und einen J_{SC} von 14,7 mA/cm^2, was besser als die Referenzsolarzellen ist. Obwohl diese Forschung noch in den Anfängen steckt, zeigen diese ersten Ergebnisse, dass selbstassemblierten Fullerenstrukturen im Bereich der Perowskitsolarzellen vielversprechend sein können.

Curriculum Vitae

Curriculum Vitae

November,2018

Saunak Kumar Das

PhD Researcher, MSc (Topper, General Chemistry), BSc (Honors in Chemistry)

(DOB: 10/03/1990, Calcutta, India; Higher academic & Research Experience: 9 years)

Institute of Physical Chemistry, Friedrich-Schiller Universität (FSU) &
Leibniz Institute of Photonic Technology (IPHT)
D-07743, Jena,
Germany

Guide: Professor Dr. Benjamin Dietzek, Dr. Martin Presselt

Research Interests

- *Imaging and Optoelectronic properties of Nanometer scaled objects*
- *Absorption Spectroscopy/Photophysics*
- *Surfaces and Interfaces, Self-Assembled Monolayers*
- *Heterojunction, Bulk Heterojunction/Pervoskite/Hybrid/Quantum Dot Solar Cells*
- *Theoretical Modelling (Q. Chem)*
- *Electrochemistry*

Educational Experiences/Coursework

Master of Science (MSc Chemistry) 2012-2014: VIT University, India (CGPA: 9.36/10)

Quantum Chemistry & Group Theory, Statistical Thermodynamics, Advanced Electro-analytical Chemistry, Chemical Kinetics, Advanced NMR, Organic Synthetic Methodology, Material Science, Advanced Spectroscopy among many others. Lab works: Analytical, Physical, Organic Synthesis, Advanced Inorganic Chemistry, Stereo-chemistry.

Bachelors of Science (BSc with Honors Chemistry) (2008-2011) 3 years: St. Xavier's College India)

Physical Chemistry, Inorganic Chemistry, Organic Chemistry, Analytical Chemistry, Polymer Chemistry

Research Projects (Masters)

I. Facile Synthesis and Characterizations of Semiconductor Selenites and perselanates

(School of Advanced Sciences, VIT University)

Supervisor: Dr Vijayaraghavan R

In this study we devised a novel one-pot synthesis route for cadmium selenite and cadmium per-selanate. We characterized these using XRD. Cadmium Selenite is an interesting material and its novelty enables metal selenites to be applied as anisotropic, semi-conductive coatings, photo-voltage sources, or photoelectric devices. We successfully synthesized and characterized this interesting nano-material (with application in Quantum dots) by reducing the prepared cadmium selenite.

II. Thermodynamic and Kinetic aspects of divalent Transition Metal Hydroxides

(School of Advanced Sciences, VIT University)

Hydroxides of divalent metal cations (Zn, Cd, Cu, Ni) find application in various fields. Cadmium Hydroxide is generated in storage battery anodes, in nickel-cadmium and silver-cadmium storage batteries its discharge. Similarly, Zinc Hydroxide is used to coat metals for protection. We have observed the rapid conversion of zinc hydroxide to its oxide at room temperature and other standard conditions when zinc chloride is treated with sodium hydroxide. Thereby, we proposed to study the thermodynamics and kinetic studies of this probable dehydration using quite a few methods. The hydroxides and the dehydrated oxides were characterized next using XRD, FTIR, DTA, SEM methods.

III. Synthesis and characterization of hydrophobic carbon nanoparticles: Application towards fluorescence quenching with novel iridium and rhodium complexes

-Indian Institute of Science Education and Research (IISER, Kolkata)

Program: Summer Student Research Project Kolkata (May 2013-July 2013)

Supervisor: Dr Pradipta Purkayastha, (https://sites.google.com/site/pradiptp/home)

Carbon nanoparticles (CNPs) are of significant importance in the luminescence chemistry serving as fluorescent marker and applications in biophotonics, opto-electronics, sensing have been explored. The synthesis methodology for hydrophilic and hydrophobic CNPs is economic, and easily achievable. Here synthesis and applications toward fluorescence quenching of hydrophobic CNPs have been reported. Novel Polynuclear complexes of Rhodium and Iridium, specifically Rh^Rh, Ir^Ir as dimers and Rh^Ir have been synthesized to act as the counterparts for CNPs. They are characterized assuming a possible directional electron transfer property and hence assumed to alter appreciably the spectral patterns of fluorescence of various light absorbing species. CNPs find sequential quenching in response to these polynuclear systems. Alongside fluorescence studies we characterized the CNPs by dynamic light scattering.

Summer Research Fellow

IV. Fabrication of selective electrochemical sensor using multiwalled carbon nanotubes for tetrahydrocannabinol: the illicit psychoactive in marijuana

-VIT University

Supervisor: Dr Annamalai Senthil Kumar (vit.academia.edu/annamalaisenthilkumarvit)

A simple and selective electrochemical sensor for Tetra Hydro Cannabinol (THC, in marijuana) by casting multiwalled carbon-nanotube (MWCNT) on glassy carbon working-electrode. The modified electrode showed a diffusion controlled redox peak at an $E1/2 = 130 \pm 30$ mV vs Ag/AgCl. The identical structural-attributes of THC and MWCNT support surface-locking THC to the planar sheet of MWCNT and facilitate the oxidation of phenolic-type OH group of THC! For the first time such mechanistic oxidation pathway for MWCNT@THC redox-couple is reported. The pH, scan rate and loading studies showing linear dependence were performed and discussed.

2nd Prize Science, Engineering Technology Conference 2013, VIT

Master Thesis: Electronically Nonadiabatic Excited State Decomposition of High Nitrogen Energetic Material TAGzt: A Combined CASSCF and RASSCF Study

-Indian Institute of Science (IISc) Bangalore

Ultrafast spectroscopy of many energetic molecules are hard to study experimentally because of the obvious reason of explosion, for which high-performing ab-initio calculations comes out handyUsing CASSCF and RASSCF, calculation, excited state dynamics and dissociation pathways of ionic energetic clusters were studied in the paradigm of theoretical gas-phase spectroscopy.

Supervisor: Dr. Atanu Bhattacharya (http://ipc.iisc.ac.in/atanub.php)

Marks: 10/10

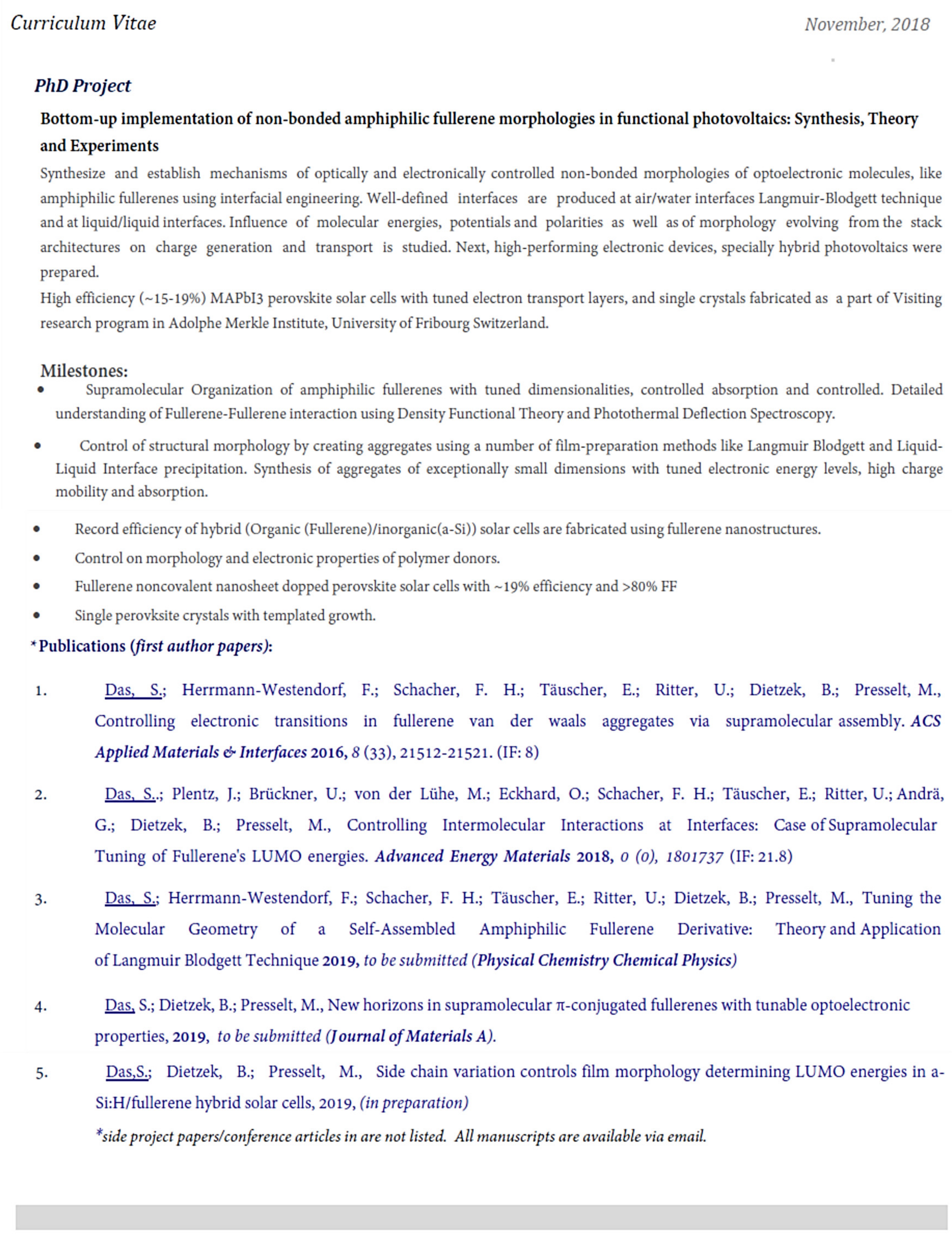

Curriculum Vitae *November, 2018*

PhD Project

Bottom-up implementation of non-bonded amphiphilic fullerene morphologies in functional photovoltaics: Synthesis, Theory and Experiments

Synthesize and establish mechanisms of optically and electronically controlled non-bonded morphologies of optoelectronic molecules, like amphiphilic fullerenes using interfacial engineering. Well-defined interfaces are produced at air/water interfaces Langmuir-Blodgett technique and at liquid/liquid interfaces. Influence of molecular energies, potentials and polarities as well as of morphology evolving from the stack architectures on charge generation and transport is studied. Next, high-performing electronic devices, specially hybrid photovoltaics were prepared.

High efficiency (~15-19%) MAPbI3 perovskite solar cells with tuned electron transport layers, and single crystals fabricated as a part of Visiting research program in Adolphe Merkle Institute, University of Fribourg Switzerland.

Milestones:

- Supramolecular Organization of amphiphilic fullerenes with tuned dimensionalities, controlled absorption and controlled. Detailed understanding of Fullerene-Fullerene interaction using Density Functional Theory and Photothermal Deflection Spectroscopy.
- Control of structural morphology by creating aggregates using a number of film-preparation methods like Langmuir Blodgett and Liquid-Liquid Interface precipitation. Synthesis of aggregates of exceptionally small dimensions with tuned electronic energy levels, high charge mobility and absorption.
- Record efficiency of hybrid (Organic (Fullerene)/inorganic(a-Si)) solar cells are fabricated using fullerene nanostructures.
- Control on morphology and electronic properties of polymer donors.
- Fullerene noncovalent nanosheet dopped perovskite solar cells with ~19% efficiency and >80% FF
- Single perovksite crystals with templated growth.

***Publications (*first author papers*):**

1. Das, S.; Herrmann-Westendorf, F.; Schacher, F. H.; Täuscher, E.; Ritter, U.; Dietzek, B.; Presselt, M., Controlling electronic transitions in fullerene van der waals aggregates via supramolecular assembly. ***ACS Applied Materials & Interfaces*** **2016,** *8* (33), 21512-21521. (IF: 8)
2. Das, S.; Plentz, J.; Brückner, U.; von der Lühe, M.; Eckhard, O.; Schacher, F. H.; Täuscher, E.; Ritter, U.; Andrä, G.; Dietzek, B.; Presselt, M., Controlling Intermolecular Interactions at Interfaces: Case of Supramolecular Tuning of Fullerene's LUMO energies. ***Advanced Energy Materials*** **2018,** *0 (0), 1801737* (IF: 21.8)
3. Das, S.; Herrmann-Westendorf, F.; Schacher, F. H.; Täuscher, E.; Ritter, U.; Dietzek, B.; Presselt, M., Tuning the Molecular Geometry of a Self-Assembled Amphiphilic Fullerene Derivative: Theory and Application of Langmuir Blodgett Technique **2019,** *to be submitted (**Physical Chemistry Chemical Physics**)*
4. Das, S.; Dietzek, B.; Presselt, M., New horizons in supramolecular π-conjugated fullerenes with tunable optoelectronic properties, **2019**, *to be submitted (**Journal of Materials A**).*
5. Das,S.; Dietzek, B.; Presselt, M., Side chain variation controls film morphology determining LUMO energies in a-Si:H/fullerene hybrid solar cells, 2019, *(in preparation)*

**side project papers/conference articles in are not listed. All manuscripts are available via email.*

Conference, Invited Talks, Posters

- Three Talks at Science Engineering Technology Conferences (2012,2013): VIT University India
- Poster: International Conference on Emerging Trends in Chemical Science (IETC, 2013) VIT University India
- Poster: DPG Conference 2015, Berlin
- Poster: Bunsentagung 2015, Ruhr University Bochum, Germany
- Talk: Dornburg Seminar Jena, 2017
- Talk: EsMolNa, Summer School of Nanoscience, Paris, 2015
- Talk: Dornburg Seminar, FSU Jena, 2017
- Poster: MRS Spring Meeting, Phoenix, Arizona, USA, 2016
- Conference Article: MRS Spring Meeting, Phoenix, Arizona, USA 2017
- Poster: Photochemistry conference, University of Jena, 2016
- Invited Talk: Nano-Science Centre, University of Copenhagen, 2017
- *Invited Talk Freiburg University, Germany* (2019)*

Teaching Activity

- General Chemistry and Physics (Hartley's High School (Kolkata India) 2011-12
- Teaching Assistant, Basic Mathematics, Masters Level (VIT University), 2013
- Master Thesis Student: 1; Research assistant of 10 MSc (Chemistry) students for Surface Chemistry/Solar cell internship (2016-17-18), FSU Germany
- Taught Scientific Instrumentation for students- VIT University, 2013

Achievements/Honors

- Visiting Research Scholarship (Adolphe Merkle Institute, University of Fribourg, Switzerland, 2018)
- Topper, MSc (General Chemistry) from VIT University, 2014
- PhD Fellowship: BMBF, Friedrich-Schiller University, Jena Germany
- PhD invitation Amsterdam University, Netherlands (*denied*)
- PhD invitation Ruhr-Universität Bochum, Germany (*denied*)
- Leibniz Association Funding 2018
- Science, Engineering, Technology (SET) conference 2013/14, Best Poster Awards
- Summer Research Fellowship, 2013

Membership/Reviewing Activity

- German Physical Society (DPG)
- Reviewer Activities: *Chemical Physics Letters (2018-present)*

Complete List of Publications

Peer-reviewed Publications

1. **Das, S.**; Herrmann-Westendorf, F.; Schacher, F. H.; Taüscher, E.; Ritter, U.; Dietzek, B.; Presselt, M., Controlling Electronic Transitions in Fullerene van der Waals Aggregates via Supramolecular Assembly. *ACS applied materials & interfaces* **2016,** *8* (33), 21512-21521. *(IF-8.097)*

2. **Das, S**.; Fiedler, J.; Buhmann, S. Y.; Walter, M.; Dietzek, B.; Presselt, M., Macroscopic Quantum Electrodynamic and (Time-Dependent) Density Functional Theory Approaches to Electronic Ground and Excited State Dispersion Interactions between Fullerenes. (*to be submitted)* **2019**.

3. **Das, S**.; Preiß, J.; Plentz, J.; Brückner, U.; von der Lühe, M.; Eckardt, O.; Dathe, A.; Schacher, F. H.; Täuscher, E.; Ritter, U.; Csáki, A.; Andrä, G.; Dietzek, B.; Presselt, M., Controlling Intermolecular Interactions at Interfaces: Case of Supramolecular Tuning of Fullerene's Electronic Structure. *Advanced Energy Materials* **2018,** *0* (0), 1801737. (*IF-21.875)*

4. **Das, S**.; Presselt, M., New horizons in supramolecular non-bonded fullerene aggregates with tunable optoelectronic properties. *(Submitted) Journal of Materials Chemistry A* 2019.

5. **Das, S**.; Täuscher, E.; Biehl, P.; Ritter, U.; Schaefer, H. F.; Dietzek, B.; Presselt, M., Synthetic, Interfacial and Optoelectronic chemistry of PEG-functionalized Fullerenes. *(in preparation)* 2019.

6. **Das, S;** Saliba, M, The versatile application range of perovskite optoelectronics, invited review paper *(in preparation),* **2019.**

7. Jahn, M; Plentz, J; Hupfer, M.; Karthik M.; **Das, S.**; Herrmann-Westendorf, F.; Kaufmann, M.; Mahammed, A.; Schulz, M.; Schulz; Dietzek B.; Gudrun A.; Weber, K.; Gross, Z.; Presselt, M., Towards Miniaturized Budget Sensors for Photometric Nitric Oxide Sensing Using Immobilized Iron(III)Corroles as Sensitizer *(to be submitted),* **2019**

8. Agung Wahyuono, Ruri; Konkin, Gulnara; Das, S.; Schulz, M. Plentz, J.; Jia, G.; Andrä, G.; Dietzek, B., Formulation of Optimum Gel Electrolytes for Quasi-Solid State Flexible Solar Cells *(in preparation),* **2019.**

Conference and other contributions

1. *Poster:* **Das, S**.; Herrmann-Westendorf, F.; Dietzek, B.; Presselt Optical characterization of highly ordered donor-acceptor films made by Langmuir Blodgett technique, 2015 *DPG Spring Meeting, (Berlin, Germany)*

2. *Poster:* **Das, S**.; Herrmann-Westendorf, F.; Dietzek, B.; Presselt, M. Impact of Aggregation on Photonic Properties of Amphiphilic Fullerenes, 2015 *Bunsentagung, (Bochum, Germany)*

3. *Talk:* **Das, S**.; Dietzek, B.; Presselt, M. Morphological and Optical properties Amphiphilic Fullerene Nanostructures, 2015 *European School on Molecular Nanoscience (ESMolNa), (Paris, France)*

4. *Poster:* **Das, S.** Herrmann-Westendorf, F.; Dietzek, B.; Presselt. M., Controlling Electronic Transitions in Fullerene Aggregates, 2016 *MRS Fall Meeting Abstract (Pheonix, Arizona, USA)*.

5. *Invited Talk:* **Das, S**.; Dietzek, B.; Presselt. M., Exploration of optoelectronic properties of fullerene nanostructures, 2017 *Department of Chemistry, University of Copenhagen, (Denmark)*

6. *Meeting Abstract:* **Das, S**.; Herrmann-Westendorf, F.; Hupfer, M.; Sivakov, V.; Dietzek, B.; Presselt, M. In Interface Doping in BHJ Solar Cells and Development of Well-Defined Model-Interfaces for Fundamental Studies and Understanding of Interface Processes and Involving Doping,. 2017 *MRS Fall Meeting Abstract* (Boston, USA).

7. Presselt, M.; Herrmann-Westendorf, F.; Kaufmann, M.; **Das, S**.; Hupfer, M.; Dietzek, B. Colored soaps for photonics, 2017; *American Chemical Society Meeting Abstracts*).

Acknowledgement

Any dissertation is a piece of creation of the highest intellectual quality and a lot of sweat and blood of several people, their tireless inspiration and hard work goes into its making!

I shall start by extending my immense respect, admiration and gratitude towards my supervisor, Dr. Benjamin Dietzek without whom this thesis would not have seen the light of day. His relentless efforts in keeping the group motivated and inspired, coupled with unparalleled hard-work and supervision has been instrumental in shaping my scientific wisdom. Though being extremely busy, by a scale many of us cannot conceive, Benjamin had his doors always open in the spirit of scientific and career discussions for me. Also thanks for tolerating my medieval English throughout the course of my PhD research. You will remain an inspiration for life, and I wish to work with you in the future.

I would also like to extend my immense gratitude and respect to my daily supervisor Dr. Martin Presselt, working with whom was a necessary exercise in patience and perseverance. In retrospect, his constant supervision has motivated me to strive for perfection, like nothing else could. I would like to thank all current and past members of both our subgroup and Dietzek group at different walks of my scientific experience. I would like to specially acknowledge Jasmin for not only learning from me, but also for making the research process fun for me.

I would also pass my gratitude to Prof. Dr. Felix Schacher for letting me work with different members of his team at different times and for our very fruitful collaboration. Specially, I would like to thank Moritz who helped me in multiple TEM measurements. I would like to thank Jonathan Plentz, Uwe Bruckner and their team for letting my use their solar cell lab facilities. I thank Dr. Andrea Csáki for letting me use her AFM facilities. I want to deeply acknowledge Prof. Uwe Ritter and his team for synthesis of our PEG-fullerenes, and sending multiple batches throughout these years. I am extremely keen on acknowledging my theory collaborators, especially Johannes Fiedler, Dr. Stefan Buhmann and Michael Walter for their cooperation with my process of learning and understanding of the many facets and complexities of fullerenes.

I would like to acknowledge Dr. Michael Saliba during my wonderful visiting research experience in Switzerland which was both scientifically and emotionally constructive,

and served to further consolidate my desire to continue with research in the domain of solar cells. I would like to thank Ruri for his collaboration throughout the FEST project.

I am indebted to many people in the course of this thesis. First and foremost I thank Julian for translating, and proof reading the German summary and many parts of this thesis! He had been a close friend who, in the course of my stay in Jena, has become my family away from home. Our trips and adventures especially with Alejandro helped us survive the hardships of PhD life. I especially thank Matze for making excellent proof reading of my thesis! I also thank Jasmin and Max for re-reading the German summary. I have come across and worked with exceptional team members, Max, Julia, Torsten, Felix and Karin who were very cooperative and helpful throughout my years in Jena.

I'd take this chance to acknowledge my friends and family. I cannot thank my father enough for his continuous career guidance and discussions in several parts of my thesis with great care; and Ma and Mamuni for never letting me miss home, in the course of the most trying period of my career. Dada, Kaku, Maroo, Bapi kaku, kakima and my cousins have all been my greatest support.

Jena and Germany has been a life changing experience, where I made lovely friends. I thank Lika, Julian, Olga, Florian, Fabian, Andy, Jürgen, Anindya, Shrea, Max, Nele for making the necessary respite from the research grind, so much fun and filled with life. Sreeja you are wonderful, and without you being here, and helping me in so many overt and covert ways, I would not have survived the many tribulations of the PhD experience. I would like to acknowledge my dear mates Sounak, Trishari, Reejula, Amit, Solanki, Arnab, Gogol, Wrishin and my dearest brothers Diptarka and Tito. Abhisekh, you are still my best man, thank you for all those crispy science-philo-art-conversations and tolerating my lunacy.

Declaration of Authorship

I hereby certify that this dissertation is, to the best of my knowledge and belief, original and the result of my own investigations, except as acknowledged, and has not been submitted, either in part or whole, for a degree at this or any other university.

Selbstständigkeitserklärung

Hiermit erkläre ich, dass ich die vorliegende Arbeit selbständig und nur unter Verwendung der angegebenen Hilfsmittel, persönlichen Mitteilungen und Quellen angefertigt habe und dass ich nicht die gleiche oder eine in wesentlichen Teilen ähnliche Abhandlung bei dieser oder einer anderen Hochschule als Abschlussarbeit/Dissertation eingereicht habe.

Saunak Das   Jena, den …………… …......………………………

Bibliography

1. Hameroff, S., Consciousness, Neurobiology and Quantum Mechanics: The Case for a Connection. In *The Emerging Physics of Consciousness*, Tuszynski, J. A., Ed. Springer Berlin Heidelberg: Berlin, Heidelberg, 2006; pp 193-253.

2. Maier, J. P.; Campbell, E. K., Fullerenes in Space. *Angewandte Chemie International Edition* **2017,** *56* (18), 4920-4929.

3. Jung, C. G., *Die Archetypen und das kollektive Unbewusste*. Walter: 1980.

4. Avouris, P.; Chen, Z.; Perebeinos, V., Carbon-based electronics. *Nature Nanotechnology* **2007,** *2*, 605.

5. Avouris, P., Graphene: Electronic and Photonic Properties and Devices. *Nano Lett.* **2010,** *10*, 4285.

6. Park, S.; Vosguerichian, M.; Bao, Z., A review of fabrication and applications of carbon nanotube film-based flexible electronics. *Nanoscale* **2013,** *5* (5), 1727-1752.

7. Matsuo, Y., Fullerene Derivatives for Organic Solar Cells. In *Chemical Science of π-Electron Systems*, Akasaka, T.; Osuka, A.; Fukuzumi, S.; Kandori, H.; Aso, Y., Eds. Springer Japan: Tokyo, 2015; pp 559-573.

8. Chiang, C.-H.; Wu, C.-G., Bulk heterojunction perovskite–PCBM solar cells with high fill factor. *Nature Photonics* **2016,** *10*, 196.

9. Jeon, I.; Yoon, J.; Ahn, N.; Atwa, M.; Delacou, C.; Anisimov, A.; Kauppinen, E. I.; Choi, M.; Maruyama, S.; Matsuo, Y., Carbon Nanotubes versus Graphene as Flexible Transparent Electrodes in Inverted Perovskite Solar Cells. *The Journal of Physical Chemistry Letters* **2017,** *8* (21), 5395-5401.

10. Halik, M.; Hirsch, A., The Potential of Molecular Self-Assembled Monolayers in Organic Electronic Devices. *Advanced Materials* **2011,** *23* (22-23), 2689-2695.

11. Zhang, X.; Zhang, Y.; Wang, Y.; Kalytchuk, S.; Kershaw, S. V.; Wang, Y.; Wang, P.; Zhang, T.; Zhao, Y.; Zhang, H.; Cui, T.; Wang, Y.; Zhao, J.; Yu, W. W.; Rogach, A. L., Color-Switchable Electroluminescence of Carbon Dot Light-Emitting Diodes. *ACS Nano* **2013,** *7* (12), 11234-11241.

12. Derycke, V.; Auvray, S.; Borghetti, J.; Chung, C. L.; Lefevre, R.; Lopez-Bezanilla, A.; Nguyen, K.; Robert, G.; Schmidt, G.; Anghel, C.; Chimot, N.; Lyonnais, S.; Streiff, S.; Campidelli, S.; Chenevier, P.; Filoramo, A.; Goffman, M. F.; Goux-Capes, L.; Latil, S.; Blase, X.; Triozon, F.; Roche, S.; Bourgoin, J. P., Carbon nanotube chemistry and assembly for electronic devices. *Comptes Rendus Physique* **2009,** *10* (4), 330-347.

13. Bolotin, K. I.; Sikes, K. J.; Jiang, Z.; Klima, M.; Fudenberg, G.; Hone, J.; Kim, P.; Stormer, H. L., Ultrahigh electron mobility in suspended graphene. *Solid State Communications* **2008,** *146* (9), 351-355.

14. Lee, W. H.; Park, Y. D., Tuning Electrical Properties of 2D Materials by Self-Assembled Monolayers. *Advanced Materials Interfaces* **2018,** *5* (1), 1700316.

15. Kroto, H. W.; Heath, J. R.; O'Brien, S. C.; Curl, R. F.; Smalley, R. E., C60: Buckminsterfullerene. *Nature* **1985,** *318*, 162.

16. Kratschmer, W.; Lamb, L. D.; Fostiropoulos, K.; Huffman, D. R., Solid C60: a new form of carbon. *Nature* **1990,** *347* (6291), 354-358.

17. Chen, X.; Fuchs, H., *Soft Matter Nanotechnology: From Structure to Function*. Wiley: 2015.

18. MacKenzie, R. C. I.; Frost, J. M.; Nelson, J., A numerical study of mobility in thin films of fullerene derivatives. *The Journal of Chemical Physics* **2010,** *132* (6), 064904.

19. Yang, Y.; Arias, F.; Echegoyen, L.; Chibante, L. P. F.; Flanagan, S.; Robertson, A.; Wilson, L. J., Reversible Fullerene Electrochemistry: Correlation with the HOMO-LUMO Energy Difference for C60, C70, C76, C78, and C84. *Journal of the American Chemical Society* **1995,** *117* (29), 7801-7804.

20. Guldi, D. M.; Illescas, B. M.; Atienza, C. M.; Wielopolski, M.; Martin, N., Fullerene for organic electronics. *Chemical Society Reviews* **2009,** *38* (6), 1587-1597.

21. Mazzio, K. A.; Luscombe, C. K., The future of organic photovoltaics. *Chemical Society Reviews* **2015,** *44* (1), 78-90.

22. Fang, Y.; Bi, C.; Wang, D.; Huang, J., The Functions of Fullerenes in Hybrid Perovskite Solar Cells. *ACS Energy Letters* **2017,** *2* (4), 782-794.

23. Li, Y.; Zhao, Y.; Chen, Q.; Yang, Y.; Liu, Y.; Hong, Z.; Liu, Z.; Hsieh, Y.-T.; Meng, L.; Li, Y.; Yang, Y., Multifunctional Fullerene Derivative for Interface Engineering in Perovskite Solar Cells. *Journal of the American Chemical Society* **2015,** *137* (49), 15540-15547.

24. Yun, M. H.; Jang, J. H.; Kim, K. M.; Song, H.-e.; Lee, J. C.; Kim, J. Y., A hybrid solar cell fabricated using amorphous silicon and a fullerene derivative. *Physical Chemistry Chemical Physics* **2013,** *15* (45), 19913-19918.

25. Zhang, Y.; Murtaza, I.; Meng, H., Development of fullerenes and their derivatives as semiconductors in field-effect transistors: exploring the molecular design. *Journal of Materials Chemistry C* **2018,** *6* (14), 3514-3537.

26. Langa, F.; De La Puente, F. L.; Nierengarten, J. F.; Chemistry, R. S. o., *Fullerenes: Principles and Applications*. Royal Society of Chemistry: 2007.

27. Orlandi, G.; Negri, F., Electronic states and transitions in C-60 and C-70 fullerenes. *Photochemical & Photobiological Sciences* **2002,** *1* (5), 289-308.

28. Yan, C.; Barlow, S.; Wang, Z.; Yan, H.; Jen, A. K. Y.; Marder, S. R.; Zhan, X., Non-fullerene acceptors for organic solar cells. *Nature Reviews Materials* **2018,** *3*, 18003.

29. Cid, A.; Moldes, Ó. A.; Diniz, M. S.; Rodríguez-González, B.; Mejuto, J. C., Redispersion and Self-Assembly of C60 Fullerene in Water and Toluene. *ACS Omega* **2017,** *2* (5), 2368-2373.

30. Shayeganfar, F.; Rochefort, A., Electronic Properties of Self-Assembled Trimesic Acid Monolayer on Graphene. *Langmuir* **2014,** *30* (32), 9707-9716.

31. Nirmalraj, P.; Thompson, D.; Molina-Ontoria, A.; Sousa, M.; Martín, N.; Gotsmann, B.; Riel, H., Nanoelectrical analysis of single molecules and atomic-scale materials at the solid/liquid interface. *Nat Mater* **2014,** *13* (10), 947-953.

32. Tanaka, I.; Kamiya, I.; Sakaki, H.; Qureshi, N.; Allen, S. J.; Petroff, P. M., Imaging and probing electronic properties of self-assembled InAs quantum dots by atomic force microscopy with conductive tip. *Applied Physics Letters* **1999,** *74* (6), 844-846.

33. Slim, S.; Rosei, F., Asymmetry in supramolecular assembly. *Science* **2016,** *353* (6304), 1098-1099.

34. Hupfer, M. L.; Kaufmann, M.; Herrmann-Westendorf, F.; Sachse, T.; Roussille, L.; Feller, K. H.; Weiss, D.; Deckert, V.; Beckert, R.; Dietzek, B.; Presselt, M., On the Control of Chromophore Orientation, Supramolecular Structure, and Thermodynamic Stability of an Amphiphilic Pyridyl-Thiazol upon Lateral Compression and Spacer Length Variation. *ACS Appl Mater Interfaces* **2017,** *9* (50), 44181-44191.

35. Álvaro Galué, H.; Oomens, J.; Buma, W. J.; Redlich, B., Electron-flux infrared response to varying π-bond topology in charged aromatic monomers. *Nature Communications* **2016,** *7*, 12633.

36. Storhoff, J. J.; Lazarides, A. A.; Mucic, R. C.; Mirkin, C. A.; Letsinger, R. L.; Schatz, G. C., What Controls the Optical Properties of DNA-Linked Gold Nanoparticle Assemblies? *Journal of the American Chemical Society* **2000,** *122* (19), 4640-4650.

37. Würthner, F.; Kaiser, T. E.; Saha-Möller, C. R., J-Aggregates: From Serendipitous Discovery to Supramolecular Engineering of Functional Dye Materials. *Angewandte Chemie International Edition* **2011,** *50* (15), 3376-3410.

38. Chen, C.-T.; Chuang, C.; Cao, J.; Ball, V.; Ruch, D.; Buehler, M. J., Excitonic effects from geometric order and disorder explain broadband optical absorption in eumelanin. *Nature Communications* **2014,** *5*, 3859.

39. Salzmann, I.; Duhm, S.; Heimel, G.; Oehzelt, M.; Kniprath, R.; Johnson, R. L.; Rabe, J. P.; Koch, N., Tuning the Ionization Energy of Organic Semiconductor Films: The Role of Intramolecular Polar Bonds. *Journal of the American Chemical Society* **2008,** *130* (39), 12870-12871.

40. Whitesides, G. M.; Grzybowski, B., Self-Assembly at All Scales. *Science* **2002,** *295* (5564), 2418-2421.

41. Palmer, L. C.; Stupp, S. I., Molecular Self-Assembly into One-Dimensional Nanostructures. *Accounts of Chemical Research* **2008,** *41* (12), 1674-1684.

42. Chang, S. S.; Tsoi, W. C.; Higgins, A. M.; Kim, J.-S.; Winfield, J. M.; James, D. T., Self-Assembled, Molecularly Aligned Conjugated Polymer Nanowires via Dewetting. *Advanced Functional Materials* **2010,** *20* (18), 3045-3054.

43. Ryu, J.-H.; Oh, N.-K.; Zin, W.-C.; Lee, M., Self-Assembly of Rod−Coil Molecules into Molecular Length-Dependent Organization. *Journal of the American Chemical Society* **2004,** *126* (11), 3551-3558.

44. Tsai, W.-W.; Tevis, I. D.; Tayi, A. S.; Cui, H.; Stupp, S. I., Semiconducting Nanowires from Hairpin-Shaped Self-Assembling Sexithiophenes. *The Journal of Physical Chemistry B* **2010,** *114* (45), 14778-14786.

45. Huang, Y. Y.; Knowles, T. P. J.; Terentjev, E. M., Strength of Nanotubes, Filaments, and Nanowires From Sonication-Induced Scission. *Advanced Materials* **2009,** *21* (38-39), 3945-3948.

46. Zou, J.; Kim, F., Self-Assembly of Two-Dimensional Nanosheets Induced by Interfacial Polyionic Complexation. *ACS Nano* **2012,** *6* (12), 10606-10613.

47. Arpin, K. A.; Losego, M. D.; Cloud, A. N.; Ning, H.; Mallek, J.; Sergeant, N. P.; Zhu, L.; Yu, Z.; Kalanyan, B.; Parsons, G. N.; Girolami, G. S.; Abelson, J. R.; Fan, S.; Braun, P. V., Three-dimensional self-assembled photonic crystals with high temperature stability for thermal emission modification. *Nature Communications* **2013,** *4*, 2630.

48. Babu, S. S.; Mohwald, H.; Nakanishi, T., Recent progress in morphology control of supramolecular fullerene assemblies and its applications. *Chemical Society Reviews* **2010,** *39* (11), 4021-4035.

49. Kirner, S.; Sekita, M.; Guldi, D. M., 25th Anniversary Article: 25 Years of Fullerene Research in Electron Transfer Chemistry. *Advanced Materials* **2014,** *26* (10), 1482-1493.

50. Guldi, D. M.; Zerbetto, F.; Georgakilas, V.; Prato, M., Ordering Fullerene Materials at Nanometer Dimensions. *Accounts of Chemical Research* **2005,** *38* (1), 38-43.

51. Itoh, Y.; Kim, B.; Gearba, R. I.; Tremblay, N. J.; Pindak, R.; Matsuo, Y.; Nakamura, E.; Nuckolls, C., Simple Formation of C60 and C60-Ferrocene Conjugated Monolayers Anchored onto Silicon Oxide with Five Carboxylic Acids and Their Transistor Applications. *Chemistry of Materials* **2011,** *23* (4), 970-975.

52. Homma, T.; Harano, K.; Isobe, H.; Nakamura, E., Preparation and Properties of Vesicles Made of Nonpolar/Polar/Nonpolar Fullerene Amphiphiles. *Journal of the American Chemical Society* **2011,** *133* (16), 6364-6370.

53. Fernandez, G.; Sanchez, L.; Veldman, D.; Wienk, M. M.; Atienza, C.; Guldi, D. M.; Janssen, R. A. J.; Martin, N., Tetrafullerene conjugates for all-organic photovoltaics. *Journal Of Organic Chemistry* **2008,** *73* (8), 3189-3196.

54. Insuasty, A.; Atienza, C.; Lopez, J. L.; Martin, N., Supramolecular pentapeptide-based fullerene nanofibers: effect of molecular chirality. *Chemical Communications* **2015,** *51* (52), 10506-10509.

55. Nierengarten, J.-F., Chemical modification of C60 for materials science applications. *New Journal of Chemistry* **2004,** *28* (10), 1177-1191.

56. Nierengarten, J.-F.; Armaroli, N.; Accorsi, G.; Rio, Y.; Eckert, J.-F., [60]Fullerene: A Versatile Photoactive Core for Dendrimer Chemistry. *Chemistry – A European Journal* **2003,** *9* (1), 36-41.

57. Sariciftci, N. S.; Braun, D.; Zhang, C.; Srdanov, V. I.; Heeger, A. J.; Stucky, G.; Wudl, F., Semiconducting Polymer-Buckminsterfullerene Heterojunctions - Diodes, Photodiodes, And Photovoltaic Cells. *Applied Physics Letters* **1993,** *62* (6), 585-587.

58. Andreas, H., The Chemistry of the Fullerenes: An Overview. *Angewandte Chemie International Edition in English* **1993,** *32* (8), 1138-1141.

59. Hirsch, A.; Brettreich, M.; Wudl, F., *Fullerenes: Chemistry and Reactions*. Wiley: 2006.

60. Troshin, P. A.; Hoppe, H.; Renz, J.; Egginger, M.; Mayorova, J. Y.; Goryochev, A. E.; Peregudov, A. S.; Lyubovskaya, R. N.; Gobsch, G.; Sariciftci, N. S.; Razumov, V. F., Material Solubility-Photovoltaic Performance Relationship in the Design of Novel Fullerene Derivatives for Bulk Heterojunction Solar Cells. *Advanced Functional Materials* **2009,** *19* (5), 779-788.

61. Troshin, P. A.; Lyubovskaya, R. N., Organic chemistry of fullerenes: the major reactions, types of fullerene derivatives and prospects for practical use. *Russian Chemical Reviews* **2008,** *77* (4), 323.

62. Bonifazi, D.; Enger, O.; Diederich, F., Supramolecular [60]fullerene chemistry on surfaces. *Chemical Society Reviews* **2007,** *36* (2), 390-414.

63. Vorobiev, A. K.; Gazizov, R. R.; Borschevskii, A. Y.; Markov, V. Y.; Ioutsi, V. A.; Brotsman, V. A.; Sidorov, L. N., Fullerene as Photocatalyst: Visible-Light Induced Reaction of Perfluorinated α,ω-Diiodoalkanes with C60. *The Journal of Physical Chemistry A* **2017,** *121* (1), 113-121.

64. Rudolf, M.; Kirner, S. V.; Guldi, D. M., A multicomponent molecular approach to artificial photosynthesis - the role of fullerenes and endohedral metallofullerenes. *Chemical Society Reviews* **2016,** *45* (3), 612-630.

65. Jain, R.; Rather, J. A.; Dwivedi, A.; Vikas, Highly Sensitive and Selective Voltammetric Sensor Fullerene Modified Glassy Carbon Electrode for Determination of Cefitizoxime in Solubilized System. *Electroanalysis* **2010,** *22* (21), 2600-2606.

66. Shrestha, R. G.; Shrestha, L. K.; Khan, A. H.; Kumar, G. S.; Acharya, S.; Ariga, K., Demonstration of Ultrarapid Interfacial Formation of 1D Fullerene Nanorods with Photovoltaic Properties. *ACS Applied Materials & Interfaces* **2014,** *6* (17), 15597-15603.

67. Maeyoshi, Y.; Saeki, A.; Suwa, S.; Omichi, M.; Marui, H.; Asano, A.; Tsukuda, S.; Sugimoto, M.; Kishimura, A.; Kataoka, K.; Seki, S., Fullerene nanowires as a versatile platform for organic electronics. *Scientific Reports* **2012,** *2*, 600.

68. Kim, J.; Park, C.; Song, I.; Lee, M.; Kim, H.; Choi, H. C., Unique Crystallization of Fullerenes: Fullerene Flowers. *Scientific Reports* **2016,** *6*, 32205.

69. Bairi, P.; Minami, K.; Hill, J. P.; Nakanishi, W.; Shrestha, L. K.; Liu, C.; Harano, K.; Nakamura, E.; Ariga, K., Supramolecular Differentiation for Construction of Anisotropic Fullerene Nanostructures by Time-Programmed Control of Interfacial Growth. *ACS Nano* **2016,** *10* (9), 8796-8802.

70. Georgakilas, V.; Pellarini, F.; Prato, M.; Guldi, D. M.; Melle-Franco, M.; Zerbetto, F., Supramolecular self-assembled fullerene nanostructures. *Proceedings of the National Academy of Sciences* **2002,** *99* (8), 5075-5080.

71. Ball, J. M.; Bouwer, R. K. M.; Kooistra, F. B.; Frost, J. M.; Qi, Y.; Domingo, E. B.; Smith, J.; Leeuw, D. M. d.; Hummelen, J. C.; Nelson, J.; Kahn, A.; Stingelin, N.; Bradley, D. D. C.; Anthopoulos, T. D., Soluble fullerene derivatives: The effect of electronic structure on transistor performance and air stability. *Journal of Applied Physics* **2011,** *110* (1), 014506.

72. Das, S.; Herrmann-Westendorf, F.; Schacher, F. H.; Tauscher, E.; Ritter, U.; Dietzek, B.; Presselt, M., Controlling Electronic Transitions in Fullerene van der Waals Aggregates via Supramolecular Assembly. *ACS Applied Materials & Interfaces* **2016,** *8* (33), 21512-21521.

73. Rispens, M. T.; Meetsma, A.; Rittberger, R.; Brabec, C. J.; Sariciftci, N. S.; Hummelen, J. C., Influence of the solvent on the crystal structure of PCBM and the efficiency of MDMO-PPV:PCBM 'plastic' solar cells. *Chemical Communications* **2003,** (17), 2116-2118.

74. Kennedy, R. D.; Ayzner, A. L.; Wanger, D. D.; Day, C. T.; Halim, M.; Khan, S. I.; Tolbert, S. H.; Schwartz, B. J.; Rubin, Y., Self-Assembling Fullerenes for Improved Bulk-Heterojunction Photovoltaic Devices. *Journal of the American Chemical Society* **2008,** *130* (51), 17290-17292.

75. W., L. B.; G., R. O.; C., C. D.; M., A. S.; A., P. A.; V., B. O.; H., S. S.; Nikos, K.; Garry, R., Inter-Fullerene Electronic Coupling Controls the Efficiency of Photoinduced Charge Generation in Organic Bulk Heterojunctions. *Advanced Energy Materials* **2016,** *6* (24), 1601427.

76. Bauernschmitt, R.; Ahlrichs, R.; Hennrich, F. H.; Kappes, M. M., Experiment versus Time Dependent Density Functional Theory Prediction of Fullerene Electronic Absorption. *Journal of the American Chemical Society* **1998,** *120* (20), 5052-5059.

77. Jammer, M., *The Philosophy of Quantum Mechanics the Interpretations of Quantum Mechanics in Historical Perspective*. 1974.

78. Simons, J., *An Introduction to Theoretical Chemistry*. Cambridge University Press: 2003.

79. Born, M.; Oppenheimer, R., Zur Quantentheorie der Molekeln. *Annalen der Physik* **1927,** *389* (20), 457-484.

80. Schrödinger, E., An Undulatory Theory of the Mechanics of Atoms and Molecules. *Physical Review* **1926,** *28* (6), 1049-1070.

81. Lewars, E., *Computational Chemistry: Introduction to the Theory and Applications of Molecular and Quantum Mechanics*. Kluwer Academic: 2003.

82. Murrell, J. N.; Kettle, S. F.; Tedder, J. M., *The Chemical Bond*. Wiley: 1987.

83. Froese Fischer, C., General Hartree-Fock program. *Computer Physics Communications* **1987,** *43* (3), 355-365.

84. Wahl, A. C.; Das, G., The Multiconfiguration Self-Consistent Field Method. In *Methods of Electronic Structure Theory*, Schaefer, H. F., Ed. Springer US: Boston, MA, 1977; pp 51-78.

85. Szalay, P. G.; Müller, T.; Gidofalvi, G.; Lischka, H.; Shepard, R., Multiconfiguration Self-Consistent Field and Multireference Configuration Interaction Methods and Applications. *Chemical Reviews* **2012,** *112* (1), 108-181.

86. Tobocman, W., Many-Body Perturbation Theory. *Physical Review* **1957,** *107* (1), 203-208.

87. Bartlett, R. J.; Musiał, M., Coupled-cluster theory in quantum chemistry. *Reviews of Modern Physics* **2007,** *79* (1), 291-352.

88. Vollhardt, D.; Byczuk, K.; Kollar, M., Dynamical Mean-Field Theory. In *Strongly Correlated Systems: Theoretical Methods*, Avella, A.; Mancini, F., Eds. Springer Berlin Heidelberg: Berlin, Heidelberg, 2012; pp 203-236.

89. Wang, Y., Quantum Monte Carlo simulation. *Ann. Appl. Stat.* **2011,** *5* (2A), 669-683.

90. Parr, R. G.; Yang, W., *Density-Functional Theory of Atoms and Molecules*. 1989.

91. Riess, J.; Münch, W., The theorem of hohenberg and kohn for subdomains of a quantum system. *Theoretica chimica acta* **1981,** *58* (4), 295-300.

92. Kohn, W.; Sham, L. J., Self-Consistent Equations Including Exchange and Correlation Effects. *Physical Review* **1965,** *140*, A1133.

93. Baerends, E. J.; Gritsenko, O. V., A Quantum Chemical View of Density Functional Theory. *The Journal of Physical Chemistry A* **1997,** *101* (30), 5383-5403.

94. Runge, E.; Gross, E. K. U., Density-Functional Theory for Time-Dependent Systems. *Phys. Rev. Lett.* **1984,** *52*, 997.

95. Runge, E.; Gross, E. K. U., Density-Functional Theory For Time-Dependent Systems. *Physical Review Letters* **1984,** *52* (12), 997-1000.

96. Furche, F.; Ahlrichs, R.; Hattig, C.; Klopper, W.; Sierka, M.; Weigend, F., Turbomole. *Wiley Interdisciplinary Reviews-Computational Molecular Science* **2014,** *4* (2), 91-100.

97. Schmidt, M. W.; Baldridge, K. K.; Boatz, J. A.; Elbert, S. T.; Gordon, M. S.; Jensen, J. H.; Koseki, S.; Matsunaga, N.; Nguyen, K. A.; Su, S. J.; Windus, T. L.; Dupuis, M.; Montgomery, J. A., GENERAL ATOMIC AND MOLECULAR ELECTRONIC-STRUCTURE SYSTEM. *Journal of Computational Chemistry* **1993,** *14* (11), 1347-1363.

98. Zerner, M. C.; Lipkowitz, K. B.; Boyd, D. B., *Reviews of Computational Chemistry*. 1991; p 313.

99. Das, S.; Preiß, J.; Plentz, J.; Brückner, U.; von der Lühe, M.; Eckardt, O.; Dathe, A.; Schacher, F. H.; Täuscher, E.; Ritter, U.; Csáki, A.; Andrä, G.; Dietzek, B.; Presselt, M., Controlling Intermolecular Interactions at Interfaces: Case of Supramolecular Tuning of Fullerene's Electronic Structure. *Advanced Energy Materials* **2018,** *8* (32), 1801737.

100. Becke, A. D.; Johnson, E. R., A Density-Functional Model of the Dispersion Interaction. *J. Chem. Phys.* **2005,** *123*, 154101.

101. Klamt, A.; Schüürmann, G., COSMO - a new Approach to Dielectric Screening in Solvents with Explicit Expressions for the Screening Energy and its Gradient. *Journal of the Chemical Society-Perkin Transactions 2* **1993,** (5), 799-805.

102. Ariga, K.; Yamauchi, Y.; Mori, T.; Hill, J. P., 25th Anniversary Article: What Can Be Done with the Langmuir-Blodgett Method? Recent Developments and its Critical Role in Materials Science. *Advanced Materials* **2013,** *25* (45), 6477-6512.

103. Petty, M. C., *Langmuir–Blodgett Films: An Introduction*. 1996; Vol. null, p null.

104. Ulman, A., PART TWO - LANGMUIR–BLODGETT FILMS. In *An Introduction to Ultrathin Organic Films*, Academic Press: San Diego, 1991; pp 101-236.

105. Butt, H. J.; Graf, K.; Kappl, M., *Physics and Chemistry of Interfaces*. Wiley: 2006.

106. Shaw, D. J., *Introduction to Colloid & Surface Chemistry*. 4. ed.; 1992.

107. Kaganer, V. M.; Mohwald, H.; Dutta, P., Structure and phase transitions in Langmuir monolayers. *Reviews of Modern Physics* **1999,** *71* (3), 779-819.

108. Petty, M. C., Possible Applications for Langmuir-Blodgett-Films. *Thin Solid Films* **1992,** *210* (1-2), 417-426.

109. Sathish, M.; Miyazawa, K. i.; Hill, J. P.; Ariga, K., Solvent Engineering for Shape-Shifter Pure Fullerene (C60). *Journal of the American Chemical Society* **2009,** *131* (18), 6372-6373.

110. Gracia-Espino, E.; Barzegar, H. R.; Sharifi, T.; Yan, A.; Zettl, A.; Wågberg, T., Fabrication of One-Dimensional Zigzag [6,6]-Phenyl-C61-Butyric Acid Methyl Ester Nanoribbons from Two-Dimensional Nanosheets. *ACS Nano* **2015,** *9* (10), 10516-10522.

111. Jackson, W. B.; Amer, N. M.; Boccara, A. C.; Fournier, D., Photothermal deflection spectroscopy and detection. *Applied Optics* **1981,** *20* (8), 1333-1344.

112. Boccara, A. C.; Fournier, D.; Jackson, W.; Amer, N. M., Sensitive photothermal deflection technique for measuring absorption in optically thin media. *Optics Letters* **1980,** *5* (9), 377-379.

113. Presselt, M.; Herrmann, F.; Shokhovets, S.; Hoppe, H.; Runge, E.; Gobsch, G., Sub-bandgap absorption in polymer-fullerene solar cells studied by temperature-dependent external quantum efficiency and absorption spectroscopy. *Chemical Physics Letters* **2012,** *542*, 70-73.

114. Ahmed, M. S., Photothermal Deflection Spectroscopy of Amorphous, Nanostructured and Nanocomposite Thin Films. *Electronic Thesis and Dissertation* **2013,** *Repository. 1678*.

115. Goldburg, W. I., Dynamic light scattering. *American Journal of Physics* **1999,** *67* (12), 1152-1160.

116. Stefanaki, E.-C., Electron microscopy: the basics. *Physics of advanced materials winter school* **2008**, 1-11.

117. Jalili, N.; Laxminarayana, K., A review of atomic force microscopy imaging systems: application to molecular metrology and biological sciences. *Mechatronics* **2004,** *14* (8), 907-945.

118. Morita, S.; Giessibl, F. J.; Meyer, E.; Wiesendanger, R., *Noncontact atomic force microscopy*. Springer: 2015; Vol. 3.

119. Zhang, X.; Li, X.-D.; Ma, L.-X.; Zhang, B., Electronic and electrochemical properties as well as flowerlike supramolecular assemblies of fulleropyrrolidines bearing ester substituents with different alkyl chain lengths. *RSC Advances* **2014,** *4* (104), 60342-60348.

120. Kutner, W.; Pieta, P.; Nowakowski, R.; Sobczak, J. W.; Kaszkur, Z.; McCarty, A. L.; D'Souza, F., Composition, Structure, Surface Topography, and Electrochemical Properties of Electrophoretically Deposited Nanostructured Fullerene Films. *Chemistry of Materials* **2005,** *17* (23), 5635-5645.

121. Xie, Q.; Perez-Cordero, E.; Echegoyen, L., Electrochemical detection of C606- and C706-: Enhanced stability of fullerides in solution. *Journal of the American Chemical Society* **1992,** *114* (10), 3978-3980.

122. Larson, B. W.; Whitaker, J. B.; Wang, X.-B.; Popov, A. A.; Rumbles, G.; Kopidakis, N.; Strauss, S. H.; Boltalina, O. V., Electron Affinity of Phenyl–C61–Butyric Acid Methyl Ester (PCBM). *The Journal of Physical Chemistry C* **2013,** *117* (29), 14958-14964.

123. Isabel Fernández, T.; Katharina, J. F.; Jose Ignacio, P., Spectroscopy of C 60 single molecules: the role of screening on energy level alignment. *Journal of Physics: Condensed Matter* **2008,** *20* (18), 184001.

124. Andreas, O., Energy level alignment at planar organic heterojunctions: influence of contact doping and molecular orientation. *Journal of Physics: Condensed Matter* **2017,** *29* (13), 133001.

125. Dutton, G.; Zhu, X. Y., Unoccupied States in C60 Thin Films Probed by Two-Photon Photoemission. *The Journal of Physical Chemistry B* **2002,** *106* (23), 5975-5981.

126. Matsumoto, F.; Iwai, T.; Moriwaki, K.; Takao, Y.; Ito, T.; Mizuno, T.; Ohno, T., Design of Fullerene Derivatives for Stabilizing LUMO Energy using Donor Groups Placed in Spatial Proximity to the C60 Cage. *The Journal of Organic Chemistry* **2012,** *77* (20), 9038-9043.

127. Bard, A. J.; Faulkner, L. R.; Leddy, J.; Zoski, C. G., *Electrochemical methods: fundamentals and applications*. wiley New York: 1980; Vol. 2.

128. Bockris, J. O. M.; Conway, B. E.; White, R. E., *Modern aspects of electrochemistry*. Springer Science & Business Media: 2012; Vol. 22.

129. Cardona, C. M.; Li, W.; Kaifer, A. E.; Stockdale, D.; Bazan, G. C., Electrochemical Considerations for Determining Absolute Frontier Orbital Energy Levels of Conjugated Polymers for Solar Cell Applications. *Advanced Materials* **2011,** *23* (20), 2367-2371.

130. Gmucova, K.; Mullerova, J., Amorphous photovoltaics: Organics versus inorganics. 2013.

131. Larsen, C. Fabricating designed fullerene nanostructures for functional electronic devices. Doctoral thesis, comprehensive summary, Umeå universitet, Umeå, 2014.

132. Braun, S.; Salaneck, W. R.; Fahlman, M., Energy-Level Alignment at Organic/Metal and Organic/Organic Interfaces. *Advanced Materials* **2009,** *21* (14-15), 1450-1472.

133. Ishii, H.; Sugiyama, K.; Ito, E.; Seki, K., Energy Level Alignment and Interfacial Electronic Structures at Organic/Metal and Organic/Organic Interfaces. *Advanced Materials* **1999,** *11* (8), 605-625.

134. Böer, K. W., *Introduction to space charge effects in semiconductors*. Springer: 2010; Vol. 37.

135. Würfel, P.; Würfel, U., *Physics of Solar Cells: From Basic Principles to Advanced Concepts*. Wiley: 2009.

136. Hagfeldt, A.; Grätzel, M., Molecular photovoltaics. *Accounts Of Chemical Research* **2000,** *33* (5), 269-277.

137. Hoppe, H.; Sariciftci, N. S., Organic solar cells: An overview. *Journal of Materials Research* **2004,** *19* (7), 1924-1945.

138. Scholes, G. D.; Rumbles, G., Excitons in nanoscale systems. *Nature Materials* **2006,** *5*, 683.

139. Brabec, C. J.; Durrant, J. R., Solution-Processed Organic Solar Cells. *MRS Bulletin* **2008,** *33* (07), 670-675.

140. Brabec, C. J.; Sariciftci, N. S.; Hummelen, J. C., Plastic Solar Cells. *Advanced Functional Materials* **2001,** *11*, 15-26.

141. Yan Ying, O.; Bang Tao, C.; Francis, E. H. T.; Ciprian, I., Process Analysis and Optimization on PECVD Amorphous Silicon on Glass Substrate. *Journal of Physics: Conference Series* **2006,** *34* (1), 812.

142. KIM, J.-E.; RYU, S.-H.; CHOI, S.-Y., THE EFFECT OF a-SiN:H AND a-Si:H SURFACE ROUGHNESS OF TFT BY PE/RACVD. *International Journal of Modern Physics B* **2010,** *24* (15n16), 3107-3111.

143. Drevillon, B.; Vaillant, F., Oxidation of plasma-deposited hydrogenated amorphous silicon. *Thin Solid Films* **1985,** *124* (3), 217-222.

144. Armarego, W. L. F., *Purification of Laboratory Chemicals*. Elsevier Science: 2017.

145. Diederich, F.; Whetten, R. L., Beyond C60: the higher fullerenes. *Accounts of Chemical Research* **1992,** *25* (3), 119-126.

146. Liu, T.; Troisi, A., What makes fullerene acceptors special as electron acceptors in organic solar cells and how to replace them. *Advanced materials (Deerfield Beach, Fla.)* **2013,** *25* (7), 1038-41.

147. Dresselhaus, M. S.; Dresselhaus, G.; Eklund, P. C., Chapter 3 - Structure of Fullerenes. In *Science of Fullerenes and Carbon Nanotubes*, Dresselhaus, M. S.; Dresselhaus, G.; Eklund, P. C., Eds. Academic Press: San Diego, 1996; pp 60-79.

148. Nath, S.; Pal, H.; Palit, D. K.; Sapre, A. V.; Mittal, J. P., Aggregation of Fullerene, C60, in Benzonitrile. *The Journal of Physical Chemistry B* **1998,** *102* (50), 10158-10164.

149. Shubina, T. E.; Sharapa, D. I.; Schubert, C.; Zahn, D.; Halik, M.; Keller, P. A.; Pyne, S. G.; Jennepalli, S.; Guldi, D. M.; Clark, T., Fullerene Van der Waals Oligomers as Electron Traps. *Journal of the American Chemical Society* **2014,** *136* (31), 10890-10893.

150. Gao, Y.; Tang, Z.; Watkins, E.; Majewski, J.; Wang, H.-L., Synthesis and Characterization of Amphiphilic Fullerenes and Their Langmuir−Blodgett Films. *Langmuir* **2005,** *21* (4), 1416-1423.

151. Kaufmann, M.; Hupfer, M. L.; Sachse, T.; Herrmann-Westendorf, F.; Weiß, D.; Dietzek, B.; Beckert, R.; Presselt, M., Introducing double polar heads to highly fluorescent Thiazoles: Influence on supramolecular structures and photonic properties. *Journal of Colloid and Interface Science* **2018,** *526*, 410-418.

152. Cheng, J. L.; Stacko, P.; Rudolf, P.; Gengler, R. Y. N.; Feringa, B. L., Bidirectional Photomodulation of Surface Tension in Langmuir Films. *Angewandte Chemie-International Edition* **2017,** *56* (1), 291-296.

153. Zhavnerko, G.; Marletta, G., Developing Langmuir-Blodgett strategies towards practical devices. *Materials Science and Engineering B-Advanced Functional Solid-State Materials* **2010,** *169* (1-3), 43-48.

154. Na, J. Y.; Kang, B.; Sin, D. H.; Cho, K.; Park, Y. D., Understanding Solidification of Polythiophene Thin Films during Spin-Coating: Effects of Spin-Coating Time and Processing Additives. *Scientific Reports* **2015,** *5*, 13288.

155. Wang, H.; He, Y.; Li, Y.; Su, H., Photophysical and Electronic Properties of Five PCBM-like C60 Derivatives: Spectral and Quantum Chemical View. *The Journal of Physical Chemistry A* **2012,** *116* (1), 255-262.

156. Negri, F.; Orlandi, G.; Zerbetto, F., Interpretation of the vibrational structure of the emission and absorption spectra of C60. *The Journal of Chemical Physics* **1992,** *97* (9), 6496-6503.

157. Hare, J. P.; Kroto, H. W.; Taylor, R., Preparation and UV / visible spectra of fullerenes C60 and C70. *Chemical Physics Letters* **1991,** *177* (4), 394-398.

158. Sauvé, G.; Fernando, R., Beyond Fullerenes: Designing Alternative Molecular Electron Acceptors for Solution-Processable Bulk Heterojunction Organic Photovoltaics. *The Journal of Physical Chemistry Letters* **2015,** *6* (18), 3770-3780.

159. Orlandi, G.; Siebrand, W., Theory of vibronic intensity borrowing. Comparison of Herzberg-Teller and Born-Oppenheimer coupling. *The Journal of Chemical Physics* **1973,** *58* (10), 4513-4523.

160. Sassara, A.; Zerza, G.; Chergui, M.; Negri, F.; Orlandi, G., The visible emission and absorption spectrum of C-60. *Journal of Chemical Physics* **1997,** *107* (21), 8731-8741.

161. Orlandi, G., The evaluation of vibronic coupling matrix elements. *Chemical Physics Letters* **1976,** *44* (2), 277-280.

162. Laporte, O.; Meggers, W. F., Some Rules of Spectral Structure*. *J. Opt. Soc. Am.* **1925,** *11* (5), 459-463.

163. Linse, P., Stacked or T-shaped benzene dimer in aqueous solution? A molecular dynamic study. *Journal of the American Chemical Society* **1992,** *114* (11), 4366-4373.

164. Stupp, S. I.; Palmer, L. C., Supramolecular Chemistry and Self-Assembly in Organic Materials Design. *Chemistry of Materials* **2014,** *26* (1), 507-518.

165. Wahyuono, R. A.; Hermann-Westendorf, F.; Dellith, A.; Schmidt, C.; Dellith, J.; Plentz, J.; Schulz, M.; Presselt, M.; Seyring, M.; Rettenmeyer, M.; Dietzek, B., Effect of annealing on the sub-bandgap, defects and trapping states of ZnO nanostructures. *Chemical Physics* **2017,** *483*, 112-121.

166. Ulman, A., *An Introduction to Ultrathin Organic Films: From Langmuir--Blodgett to Self--Assembly*. Elsevier Science: 2013.

167. Tanese, M. C.; Pignataro, B.; Farinola, G. M.; Colangiuli, D.; Valli, L.; Giotta, L.; Conoci, S.; Marinelli, F.; Leva, E.; Babudri, F.; Naso, F.; Sabbatini, L.; Zambonin, P. G.; Torsi, L., Nanostructural depth-profile and field-effect properties of poly(alkoxyphenylene-thienylene) Langmuir-Scafer thin-films. *Thin Solid Films* **2008,** *516* (10), 3263-3269.

168. Nagarajan, R., Molecular Packing Parameter and Surfactant Self-Assembly: The Neglected Role of the Surfactant Tail. *Langmuir* **2002,** *18* (1), 31-38.

169. Akselrod, L.; Byme, H. J.; Sutto, T. E.; Roth, S., Structure and properties of thermally annealed fullerene films. *Chemical Physics Letters* **1995,** *233* (4), 436-443.

170. Ryu, M. S.; Cha, H. J.; Jang, J., Effects of thermal annealing of polymer:fullerene photovoltaic solar cells for high efficiency. *Current Applied Physics* **2010,** *10* (2, Supplement), S206-S209.

171. Orgiu, E.; Squillaci, M. A.; Rekab, W.; Borjesson, K.; Liscio, F.; Zhang, L.; Samori, P., The dramatic effect of the annealing temperature and dielectric

functionalization on the electron mobility of indene-C60 bis-adduct thin films. *Chemical Communications* **2015,** *51* (25), 5414-5417.

172. Sachse, T.; Martinez, T. J.; Dietzek, B.; Presselt, M., A program for automatically predicting supramolecular aggregates and its application to urea and porphin. *Journal of Computational Chemistry* **2018,** *39* (13), 763-772.

173. Herzberg, G.; Teller, E., *Zeitschrift fiir Physikalische Chemie (Frankfurt am Main)* **1933,** *B 21*, 410.

174. Yoo, S. H.; Kum, J. M.; Cho, S. O., Tuning the electronic band structure of PCBM by electron irradiation. *Nanoscale Research Letters* **2011,** *6* (1), 545.

175. Reinspach, J. A.; Diao, Y.; Giri, G.; Sachse, T.; England, K.; Zhou, Y.; Tassone, C.; Worfolk, B. J.; Presselt, M.; Toney, M. F.; Mannsfeld, S.; Bao, Z., Tuning the Morphology of Solution-Sheared P3HT:PCBM Films. *ACS Applied Materials & Interfaces* **2016,** *8* (3), 1742–1751.

176. Han, G. D.; Maurano, A.; Weis, J. G.; Bulović, V.; Swager, T. M., VOC enhancement in polymer solar cells with isobenzofulvene–C60 adducts. *Organic Electronics* **2016,** *31*, 48-55.

177. Singh, T. B.; Sariciftci, N. S.; Yang, H.; Yang, L.; Plochberger, B.; Sitter, H., Correlation of crystalline and structural properties of C60 thin films grown at various temperature with charge carrier mobility. *Applied Physics Letters* **2007,** *90* (21), 213512.

178. Mutolo, K. L.; Mayo, E. I.; Rand, B. P.; Forrest, S. R.; Thompson, M. E., Enhanced Open-Circuit Voltage in Subphthalocyanine/C60 Organic Photovoltaic Cells. *Journal of the American Chemical Society* **2006,** *128* (25), 8108-8109.

179. Elumalai, N. K.; Uddin, A., Open circuit voltage of organic solar cells: an in-depth review. *Energy & Environmental Science* **2016,** *9* (2), 391-410.

180. Heumueller, T.; Mateker, W. R.; Distler, A.; Fritze, U. F.; Cheacharoen, R.; Nguyen, W. H.; Biele, M.; Salvador, M.; von Delius, M.; Egelhaaf, H.-J.; McGehee, M. D.; Brabec, C. J., Morphological and electrical control of fullerene dimerization determines organic photovoltaic stability. *Energy & Environmental Science* **2016,** *9* (1), 247-256.

181. Hu, T.; Jiang, P.; Chen, L.; Yuan, K.; Yang, H.; Chen, Y., Amphiphilic fullerene derivative as effective interfacial layer for inverted polymer solar cells. *Organic Electronics* **2016,** *37*, 35-41.

182. Koopmann, R.; Gerischer, H., Untersuchung der elektrochemischen Reduktion von Nitrobenzol durch Kombination von ESR-Messungen mit elektroanalytischen Methoden. *Berichte der Bunsengesellschaft für physikalische Chemie* **1966,** *70* (2), 127-138.

183. Froitzheim, A.; Brendel, K.; Elstner, L.; Fuhs, W.; Kliefoth, K.; Schmidt, M., Interface recombination in heterojunctions of amorphous and crystalline silicon. *J Non-Cryst Solids* **2002,** *299–302, Part 1*, 663-667.

184. Bonoldi, L.; Carati, C.; Montanari, L.; Po', R., Effects of Aging and Annealing on the Density of Trap States in Organic Photovoltaic Materials. *The Journal of Physical Chemistry C* **2014,** *118* (15), 7751-7758.

185. Presselt, M.; Bärenklau, M.; Rösch, R.; Beenken, W. J. D.; Runge, E.; Shokhovets, S.; Hoppe, H.; Gobsch, G., Sub-Bandgap Absorption in Polymer-Fullerene Solar Cells. *Applied Physics Letters* **2010,** *97* (25), 253302-01 - 02.

186. Beenken, W. J. D.; Herrmann, F.; Presselt, M.; Hoppe, H.; Shokhovets, S.; Gobsch, G.; Runge, E., Sub-bandgap absorption in organic solar cells: experiment and theory. *Physical Chemistry Chemical Physics* **2013,** *15* (39), 16494-16502.

187. Kirchartz, T.; Pieters, B. E.; Kirkpatrick, J.; Rau, U.; Nelson, J., Recombination via tail states in polythiophene:fullerene solar cells. *Physical Review B* **2011,** *83* (11), 115209.

188. Collavini, S.; Delgado, J. L., Fullerenes: the stars of photovoltaics. *Sustainable Energy & Fuels* **2018,** *2* (11), 2480-2493.

189. Li, C.-Z.; Yip, H.-L.; Jen, A. K. Y., Functional fullerenes for organic photovoltaics. *Journal of Materials Chemistry* **2012,** *22* (10), 4161-4177.

190. Mi, D.; Kim, J. H.; Kim, H. U.; Xu, F.; Hwang, D. H., Fullerene derivatives as electron acceptors for organic photovoltaic cells. *J Nanosci Nanotechnol* **2014,** *14* (2), 1064-84.

191. Lin, Y.; Zhan, X., Non-fullerene acceptors for organic photovoltaics: an emerging horizon. *Materials Horizons* **2014,** *1* (5), 470-488.

192. Nakanishi, T., Supramolecular soft and hard materials based on self-assembly algorithms of alkyl-conjugated fullerenes. *Chemical Communications* **2010,** *46* (20), 3425-3436.

193. Saliba, M.; Matsui, T.; Seo, J.-Y.; Domanski, K.; Correa-Baena, J.-P.; Nazeeruddin, M. K.; Zakeeruddin, S. M.; Tress, W.; Abate, A.; Hagfeldt, A.; Grätzel, M., Cesium-containing triple cation perovskite solar cells: improved stability, reproducibility and high efficiency. *Energy & Environmental Science* **2016,** *9* (6), 1989-1997.

194. Gholipour, S.; Ali, A. M.; Correa-Baena, J.-P.; Turren-Cruz, S.-H.; Tajabadi, F.; Tress, W.; Taghavinia, N.; Grätzel, M.; Abate, A.; De Angelis, F.; Gaggioli, C. A.; Mosconi, E.; Hagfeldt, A.; Saliba, M., Globularity-Selected Large Molecules for a New Generation of Multication Perovskites. *Advanced Materials* **2017,** *29* (38), 1702005-n/a.

195. Das, S.; Täuscher, E.; Biehl, P.; Ritter, U.; Schaefer, H. F.; Dietzek, B.; Presselt, M., Synthetic, Interfacial and Optoelectronic chemistry of PEG-functionalized Fullerenes. *Soft Mater/JMC C/ PCCP* **2019**.

196. Correa-Baena, J.-P.; Abate, A.; Saliba, M.; Tress, W.; Jesper Jacobsson, T.; Grätzel, M.; Hagfeldt, A., The rapid evolution of highly efficient perovskite solar cells. *Energy & Environmental Science* **2017,** *10* (3), 710-727.

197. Gatti, T.; Menna, E.; Meneghetti, M.; Maggini, M.; Petrozza, A.; Lamberti, F., The Renaissance of fullerenes with perovskite solar cells. *Nano Energy* **2017,** *41*, 84-100.

198. Saliba, M.; Correa-Baena, J.-P.; Wolff, C. M.; Stolterfoht, M.; Phung, N.; Albrecht, S.; Neher, D.; Abate, A., How to Make over 20% Efficient Perovskite Solar Cells in Regular (n–i–p) and Inverted (p–i–n) Architectures. *Chemistry of Materials* **2018,** *30* (13), 4193-4201.